LBNL-43356

ERNEST ORLANDO LAWRENCE
BERKELEY NATIONAL LABORATORY

Ion Implantation of $In_{0.53}Ga_{0.47}As$

Marlene I. Almonte

Materials Sciences Division
Center for Advanced Materials

May 1999

Ph.D. Thesis

DISCLAIMER

LBNL-43356

Ion Implantation of $In_{0.53}Ga_{0.47}As$

Marlene Isabel Almonte

Materials Science and Mineral Engineering
University of California, Berkeley

and

Center for Advanced Materials
Materials Sciences Division
Ernest Orlando Lawrence Berkeley National Laboratory
1 Cyclotron Road
Berkeley, California 94720

Ph.D. Thesis

May 1999

This work was supported by the Director, Office of Science, Office of Basic Energy Sciences, Materials Sciences Division, of the U.S. Department of Energy under Contract No. DE-AC03-76SF00098.

Ion Implantation of $In_{0.53}Ga_{0.47}As$

by

Marlene Isabel Almonte

B.S. (Rensselaer Polytechnic Institute) 1992

M.S. (University of California, Berkeley) 1996

A dissertation submitted in partial satisfaction of the

requirements for the degree of

Doctor of Philosophy

in

Engineering-Materials Science

and Mineral Engineering

in the

GRADUATE DIVISION

of the

UNIVERSITY OF CALIFORNIA, BERKELEY

Committee in charge:

Professor Eugene E. Haller, Chair

Professor Timothy D. Sands

Professor Peter Yu

Spring 1999

Ion Implantation of $In_{0.53}Ga_{0.47}As$

by

Marlene Isabel Almonte

Abstract

Ion Implantation of $In_{0.53}Ga_{0.47}As$

by

Marlene Isabel Almonte

Doctor of Philosophy in Engineering-
Materials Science and Mineral Engineering

University of California, Berkeley

Professor Eugene E. Haller, Chair

The ternary compound $In_{0.53}Ga_{0.47}As$, lattice-matched to InP, is a semiconductor alloy of technological importance for numerous electronic and optoelectronic device applications. One of these applications includes photodiodes to be developed for the 1.3-1.55 μm wavelength range where silica fibers have their lowest optical loss. With a rapid increase in its use there is an essential need to understand the effects of ion implantation of this alloy semiconductor for implant isolation purposes in which highly resistive layers are required. Due to the small band gap (0.75 eV at 300K) of $In_{0.53}Ga_{0.47}As$, the estimated maximum resistivity is of the order of 1000 Ω-cm.

Implant isolation can be achieved by the implantation of either inert noble gas ions or electrically active ions. Ion bombardment with inert species introduces defects which trap charge carriers. In the case of implant isolation by electrically active ions, the implanted impurities form an electronic level located close to the middle of the bandgap.

Studies of the effects of implantation in $In_{0.53}Ga_{0.47}As$ due to damage by implantation of Ne^+ ions and to compensation by implantation of Fe^+ ions are reported in

this thesis. The former only involves lattice damage related effects while the latter leads to damage and dopant induced compensation. From the Ne^+ implantation results it appears that the damage related energy levels in $In_{0.53}Ga_{0.47}As$ produced by ion bombardment of chemically inactive species, are not sufficiently deep to lead to effective isolation. A higher resistivity of the order of 770 Ω-cm is achieved with Fe^+ implantation, indicating that Fe introduces an energy level deep in the bandgap.

The changes in the electrical properties of the layers are correlated to the lattice damage (damage induced effects) and/or the diffusion of the compensating dopants (dopant induced compensation). Structural characterization of the layers is performed with channeling Rutherford Backscattering Spectrometry (RBS). The distribution of the compensating dopants in the as-implanted and annealed layers is examined by Secondary Ion Mass Spectrometry (SIMS). SIMS analysis shows Fe out-diffusion which results in the loss of the semi-insulating electrical characteristics. To further our understanding of Fe diffusion in $In_{0.53}Ga_{0.47}As$, the diffusion coefficient of Fe is measured for the first time. The diffusivity of Fe was measured to be $4x10^{-13}$ cm^2 s^{-1} at 550°C. The thermal stability of these damage and compensation induced effects producing implant isolation is discussed in detail.

Table of Contents

Acknowledgements

I would like to thank Professor Eugene Haller for his continual guidance, encouragement, and support. I would like to extend my gratitude to Professor Peter Yu and Professor Timothy Sands for reviewing this dissertation. Dr. Kin Man Yu provided continued assistance with Rutherford Backscattering Spectrometry. I am also grateful to Dr. Kin Man Yu and Dr. Wladek Walukiewicz for the many valuable discussions on implant isolation. This research was made possible by Dr. Hong Hou, Dr. John Reno, and Dr. Joanna Mirecki-Millunchick from Sandia National Laboratories who kindly provided samples for this work. I am indebted to Andreas Stonas (Lawrence Berkeley National Labs) and Mark Ridgway (Australian National University) for performing the ion implantation for this research. Dr. Harmut Bracht provided invaluable expertise and insight on impurity diffusion.

My sincere thanks to all of my fellow graduate students and "*amigos*" in the Haller research group who were extremely supportive. I will never forget the fun times we shared playing cards at lunchtime. I would like to extend a special thanks to David Hom for his assistance. Hughes Silvestri who kindly submitted my dissertation to Graduate Division, since I was on the east coast.

I am grateful to the University of California (Graduated Opportunity Award) and the American Association of University Women (Selected Professions Fellowship) for their financial support. This work was supported by the Director, Office of Science, Office of Basic Energy Sciences, Materials Science Division of the U.S. Department of Energy under Contract No. DE-AC03-76SF00098.

One experiences many hurdles and difficult times in graduate school. I was able to overcome them thanks to the overwhelming support and encouragement from my family and friends. My mother instilled in her daughters the value of an education and a career. She has been a fountain of inspiration and strength. As my graduate studies come to completion, I only wish she could be present on my graduation day to see the fruits of her hard work and sacrifices. But, being the phenomenal mother that she "is", I know she will be there spiritually as she has been throughout this journey.

I am eternally grateful to my dad (Bolivar) and "sisters" (Ana, Michelle and Silvia) for their unconditional love and support. Members of my family traveled to the west coast several times and sent me many care packages to keep my spirits up. They cheered me on, every step of the way.

I am indebted to the Olivo and Martinez families for their endless support and encouragement. Our families, along with the Viciedos, have shared many common goals and experiences. Our parents came from humble beginnings and immigrated to the United States in pursuit of a better life for their children. We were the first generation of college graduates in our families and many of us continued onto graduate school. It astonishes me how much we have accomplished. Thanks to the dedication and support of our parents, we will be able to provide our children with an infinite number of opportunities.

To my husband and best friend, Victor Olivo, "gracias" for your endless love and encouragement. You have always been extremely understanding and supportive on my academic pursuits. Now that I have accomplished something that has meant so much to me, I rejoice knowing that I can celebrate it with you.

1. Introduction

1.1 Fundamentals of semiconductor physics and electronic devices

1.1.1 General

The worldwide prevalence of portable computers, fax machines, video cassette recorders, cellular phones, "intelligent" automobiles, and countless other technical tools & gadgets can be attributed to the existence of semiconductor devices, especially integrated circuits contained on small single crystal chips of, for example, silicon. Each integrated circuit consists of up to millions of diodes, transistors, resistors, and capacitors. The functionality of these circuits is based on the physical, specifically, electronic properties of the devices making up the circuit. In turn these properties are intimately related to the material properties of semiconductors. A major goal of electronic materials research is the development of a deep understanding of the fundamental principles of all the materials and their interactions used in making electronic devices, so that higher performance integrated circuits may be developed.

1.1.2 Intrinsic semiconductors

As suggested by their name, semiconductors are neither good electrical conductors (e.g. metals) nor good electrical insulators. Their ability to conduct electricity is intermediate and strongly depends on doping, i.e., the addition of specific impurity atoms. Electrical resistivity values at room temperature for semiconductors range from 10^{-4} to 10^{9} Ω-cm. In contrast to metals the electrical resistivity of undoped semiconductors strongly depends on temperature.

The electrical conductivity of an intrinsic semiconductor is independent of impurities. Conduction results from the thermal promotion of electrons from a filled

valence band in which they are immobile to an empty conduction band in which they can move. The removal of electrons, the negative charge carriers, from the valence band produces holes which act like mobile positive charge carriers. Since each excitation leaves behind a hole in the valence band, the concentration of electrons in the conduction band equals the concentration of holes ($n_e=n_h$). This intrinsic conduction at room temperature is possible because of the relatively small energy band gap between the valence and conduction band in semiconductors. Semiconductors have band gaps of the order of 0.5 to 3 eV.

Si and Ge are elemental semiconductors, whereas GaAs and InP belong to a very large family of compound semiconductors. The class of ternary and quaternary compounds consists of alloy semiconductors which include AlGaAs, InGaAs, and InGaAsP. The energy gap, lattice constant, and several physical properties of several III-V compounds and their alloys are shown in Fig. A.1 and listed in Table A.2.

Si is unquestionably the most important and widely used semiconductor for integrated circuits. One of the reasons for its widespread use is its ability to form a stable oxide film which exhibits excellent insulating properties and a very small interface state density. These thermal oxides are essential for masking selectively during dopant implantation and diffusion, metallization, device isolation and other device processes.

The technological importance of GaAs and InP stems from their potential to be used for both electronic and photonic applications. For photonic applications, these semiconductors have a distinct advantage over Si, which has an indirect band gap and is a highly inefficient photonic material. Furthermore, III-V materials have larger electron mobilities at low electric fields than Si, which make them attractive candidates for high-

speed devices. Some of the applications of GaAs include microwave devices, high-speed digital integrated circuits, and as substrates for epitaxial growth. InP is mostly used as substrate material for growing lattice-matched epitaxial layers of alloys, such as InGaAs and InGaAsP. These ternary and quaternary alloys play an important role in the development of light sources and detectors for fiber optic communication.

1.1.3 Extrinsic semiconductors

The electrical conductivity of extrinsic semiconductors is dominated by impurities and/or defects. Typically impurities have been intentionally added. These impurities are called "dopants", and the process of adding these components is known as "doping". The effect of these impurities arises from the fact that they introduce energy levels in the band gap of the semiconductor. The nature of these levels determines many of the electrical and optical properties of the semiconductor. Each ionized dopant atom can contribute one or more free charge carriers. The intrinsic carrier concentration $\mathbf{n_i}$ at room temperature of Si and GaAs are $1.4 \times 10^{10} cm^{-3}$ and $1.8 \times 10^{6} cm^{-3}$, respectively. As a result, the addition of a very small concentration of dopants ($>\mathbf{n_i}$) will change the conductivity significantly and the extrinsic carriers become the dominant source of conduction.

A dopant in a semiconductor acts either as a donor or an acceptor when it occupies a substitutional lattice site, depending on whether it has an extra or missing valence electron, respectively. For instance, for GaAs if a column VI element (e.g., Se or Te) substitutes an As site, it is a donor. On the other hand, if a column II element (e.g., Zn) sits on a Ga site, the dopant is an acceptor. Si in GaAs is an amphoteric dopant. Si can act as a donor on a Ga site (Si_{Ga}) or as an acceptor on an As site (Si_{As}). In theory, any group IV element in GaAs is amphoteric. Among the group IV elements Si, Ge, Sn

behave amphoterically while C is predominantly an acceptor or forms neutral complexes (Moll et al. 1993).

1.1.3.1 Shallow and deep levels

A shallow level defect introduces a weak but long-range potential disturbance in the lattice which can extend over tens or more unit cells in real space. In turn, it is highly localized in k-space. The energy levels associated with shallow donors and acceptors are discrete and represent the binding energy of an electron or hole to the impurity in the host, respectively. For shallow donors, the binding energy of the free carrier can be described by the effective mass approximation (Kohn and Luttinger 1955). In this approximation, the Bohr theory of the hydrogen atom is modified to include the dielectric constant of the semiconductor (ε) and the effective mass of the electrons ($\mathbf{m_e}$) in the crystal. The donor ionization energy (eV) is:

$$E_d = \frac{13.6}{\varepsilon^2}\frac{m_e}{m} \tag{1.1}$$

where **m** is the free electron mass. The ionization energies for donor and acceptor ground states range from a few to a few tens of meV. The Bohr radius (Å) corresponding to the ground states has to be modified accordingly from that of the hydrogen atom:

$$a_d = \frac{0.53\varepsilon}{m_e/m} \tag{1.2}$$

The effective mass approximation can also be applied to acceptors, although the situation is more complicated than for donors due to the degeneracy of light and heavy hole bands at the top of the valence band. In addition, the valence bands are not perfectly parabolic but are warped and can not be described by simple effective masses. Baldereschi and

Lipari (Baldereschi et al. 1973, Baldereschi et al. 1974) have calculated the energy levels of shallow acceptor states in various semiconductors (Table A.1).

In addition to the impurities which form shallow levels chemical impurities and charged point defects exist which form deep level centers in semiconductors. The wavefunctions associated with these deep level impurities are localized in real space and extend over only one or a few unit cells. The energy levels of these centers are called "deep" because they are usually located far away from the band edges in the band gap of the semiconductor.

Typical deep level impurities include for example gold and iron in Si, and transition metal elements and the As_{Ga} anti-site in GaAs. A deep level of particular interest is the DX center observed in GaAs and AlGaAs. Si_{Ga} exhibits a shallow donor level in GaAs and $Al_xGa_{1-x}As$ ($x<0.22$). This shallow donor level transforms into a deep donor DX center in $Al_xGa_{1-x}As$ for $x>0.22$ (Lang et al. 1977, Lang 1986, Chand et al. 1984) and in pure GaAs under hydrostatic pressures greater than 20 kbar (Mizuta et al. 1985, Wolk et al. 1991).

In many cases deep levels are detrimental in semiconductors, specifically in device applications which require long minority carrier lifetimes. These impurities can act as traps or recombination centers for charge carriers. Consequently, their presence can reduce minority carrier lifetimes. One of the cases where deep levels are necessary to produce a desirable property is semi-insulating GaAs. The deep levels of the As_{Ga} anti-sites in As rich GaAs pin the Fermi level close to the middle of the band gap.

1.1.3.2 General properties of transition metal impurities

Transition metal elements form a very important class of impurities in III-V semiconductors because of their ability to compensate shallow impurities and pin the Fermi level near midgap. With the proper relative concentrations these can lead to semi-insulating layers in compound semiconductors.

Transition metal impurities occupy substitutional cation sites in III-V compound semiconductors (Weber 1993). Typical solubility limits are of the order of 10^{17}–10^{18} cm^{-3}. The electronic configurations of the valence shells of transition metal impurities are $3d^n4s^2$. In its neutral state, the electron configuration of Fe (the transition metal of interest for this work) is $3d^64s^2$. A transition metal impurity on a group III lattice site has an electron configuration of M^{+3}, since three of its valence electrons are used for bonding.

Transition metal impurity levels have been used to determine band edge discontinuities between semiconductor heterojunctions (Langer et al. 1985, Nolte et al. 1987). Within a class of isovalent semiconductors, (e.g., III-V compounds and their alloys), transition metal impurity levels have been observed to remain at a fixed energy relative to the vacuum level, i.e., they align (with respect to each other) across a sequence of layers with different composition. For this reason, band edge discontinuities can be precisely determined once the positions of the energy levels of the transition metals in the various semiconductors have been determined.

1.1.4 Doping techniques

The various methods of introducing impurities into a semiconductor include dopant incorporation during crystal growth, neutron transmutation doping (NTD),

diffusion, and ion implantation. Ion implantation, the technique used for this work, will be discussed in extensive detail in section 2.1.

Doping during crystal growth can be achieved by adding a piece of heavily doped semiconductor to the melt. The maximum concentration of impurities which can be incorporated into the semiconductor is given by the solid solubility of the dopant. The concentration of impurities in the growing crystal c_s is characterized by a segregation (or distribution) coefficient:

$$k = c_s / c_l \tag{1.3}$$

where c_l is the concentration of impurities in the melt. Values for segregation coefficients for some impurities in Si range from $2x10^{-6}$ for Ti to 1.25 for O (Trumbore 1960, Hopkins et al. 1986). Segregation coefficients as large as 3 have been observed in Be doped GaAs crystals (Milnes 1973). An effective segregation coefficient is sometimes defined which incorporates factors such as growth rate, stirring conditions, crystallographic orientation of the growing interface, and stoichiometry (Swaminathan et al. 1991).

If the segregation coefficient differs from unity (no segregation), impurity striations are typically generated and observed in crystals grown from the melt. Striations are periodic fluctuations of the dopant concentration in the crystal. Rotation of the seed and crucible results in symmetric or rotational striations. Whereas, temperature fluctuations can lead to nonrotational striations. Temperature gradients at the melt-crystal interface modify the crystal growth rate and the effective segregation coefficient. As a result, impurity striations are observed (Swaminathan et al. 1991).

Neutron transmutation doping provides extremely uniform doping in semiconductors. In NTD, the semiconductor is irradiated with thermal neutrons. Newly formed isotopes decay into dopants upon neutron capture. A uniform doping concentration can be achieved as a result of the random distribution of isotopes and small absorption cross section for thermal neutrons. Amongst the various semiconductors which have been doped by this method, Ge is the only one which exhibits both n-type and p-type doping. Several hundred tons per year of ultrapure Si are doped n-type by forming P with NTD for high power, high voltage applications.

High temperature impurity diffusion has been one of the most important processing steps used in the fabrication of integrated circuits. In Si technology, diffusion of impurities allows the formation of p-n junctions, conduction channels, and source and drain regions. Since the performance of devices depends critically on dopant concentration profiles, the diffusion of various impurities has been studied rather extensively. The diffusion process often begins with the deposition of a high concentration of impurities on the semiconductor surface. Alternatively, the semiconductor wafer can be placed in a quartz-tube diffusion furnace where a gas containing the desired dopant impurities flows over the wafer. Temperatures of the order of 1000°C are required for appreciable diffusion of impurities in Si over distances of hundreds of nm.

The fundamental laws of diffusion are encompassed in Fick's first and second laws and can be written for the one dimensional case as:

$$F = -D\frac{\partial C}{\partial x} \tag{1.4}$$

$$\frac{\partial C}{\partial t} = D\frac{\partial^2 C}{\partial x^2} \tag{1.5}$$

respectively for $\mathbf{D} \neq f(\mathbf{C})$. **F** is the flux of diffusing species, $\partial \mathbf{C}/\partial \mathbf{x}$ is the concentration gradient, and **D** is the diffusion coefficient (diffusivity). Fisk's second law has an infinite number of possible solutions. A unique solution can be obtained through the application of boundary conditions. For the diffusion conditions most common in semiconductor processing, two boundary conditions are widely used. Diffusion of a fixed surface dopant concentration (constant source diffusion) leads to the following solution for eq. 1.5:

$$N(x,t) = N_o erfc\left(\frac{x}{2\sqrt{Dt}}\right) \tag{1.6}$$

for a surface concentration of $\mathbf{N_o}$. A Gaussian distribution results for diffusion of a constant supply of impurities **Q** (atoms cm^{-2}) (limited source diffusion):

$$N(x,t) = \frac{Q}{\sqrt{\pi Dt}} \exp -\left(\frac{x}{2\sqrt{Dt}}\right)^2 \tag{1.7}$$

The complementary and Gaussian diffusion profiles are shown graphically in Fig. 1.1(a) and Fig. 1.1(b), respectively.

Diffusion coefficients follow the Arrhenius behavior:

$$D = D_o \exp\left(\frac{-E_a}{kT}\right) \tag{1.8}$$

where $\mathbf{D_o}$ is the pre-exponential constant. Table 1.1 summarizes the activation energies and pre-exponential constants for common impurities in Si and GaAs.

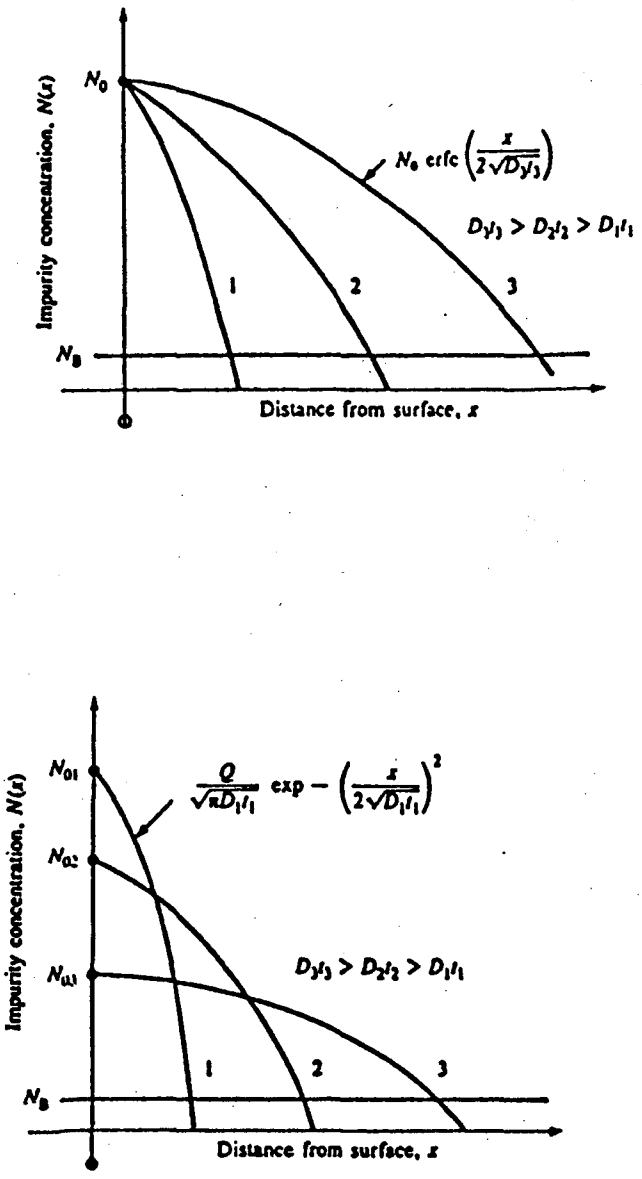

Fig. 1.1 Diffusion profiles for boundary conditions of (a) constant surface concentration and (b) limited source. (Jaeger 1988)

Table 1.1 Intrinsic diffusivities and activation energies of substitutional and self-diffusers in Si. Diffusivities and activation energies are in units of $cm^2\ s^{-1}$ and eV, respectively. The diffusivities given by D_i^0, D_i^+, D_i^-, D_i^{2-} are associated with the $A\text{-}V^0$, $A\text{-}V^+$, $A\text{-}V^-$, and $A\text{-}V^{2-}$ impurity-vacancy pair interactions, respectively. (Huff et al. 1978)

		P	As	Sb	B	Al	Ga	Si
D_i^0	D_0	3.85	0.066	0.214	0.037	1.385	0.374	0.015
	E_0	3.66	3.44	3.65	3.46	3.41	3.39	3.89
D_i^+	D_0	—	—	—	0.76	2480	28.5	1180
	E_0	—	—	—	3.46	4.20	3.92	5.09
D_i^-	D_0	4.44	22.9	13	—	—	—	16
	E_0	4.0	4.1	4.0	—	—	—	4.54
D_i^{2-}	D_0	44.2	—	—	—	—	—	10
	E_0	4.37	—	—	—	—	—	5.1

[a] D_0 in $cm^2\ s^{-1}$; E_0 in eV.

Table 1.2 Diffusion prefactor D_0 and activation energy E_d for diffusion for impurities in GaAs. Diffusion constants and activation energies are in units of $cm^2\ s^{-1}$ and eV, respectively. (Shaw 1973)

Impurity	D_0 ($cm^2\ s^{-1}$)	E_d (eV)
Au	2.9×10^{1}	2.64
Be	7.3×10^{-6}	1.2
Cd		2.43
Cr	4.3×10^{3}	3.4
Cu	3×10^{-2}	0.53
Li	5.3×10^{-1}	1.0
Mg	2.6×10^{-2}	2.7
Mn	6.5×10^{-1}	2.49–2.75
O	2×10^{-3}	1.1
S	1.85×10^{-2}	2.6
Se	3.0×10^{3}	4.16
Sn	3.8×10^{-2}	2.7
Zn		2.49
Hg	$D = 5 \times 10^{-14}$ @1000°C	
Te	$D = 10^{-13}$ @1000°C	
	$D = 2 \times 10^{-12}$ @1100°C	

Four basic diffusion mechanisms have been observed: 1) interstitial, 2) substitutional or vacancy, 3) interstitial-substitutional and 4) interstitialcy (Ghandi 1994, Mayer 1990). In the case of the interstitial mechanism, an interstitial impurity atom jumps from one interstitial site to another e.g. Li donors in Si and Ge diffuse in this manner. Substitutional or vacancy assisted diffusion involves the impurity jumping from a substitutional site into a neighboring vacancy. The concentration of vacancies and their mobility controls this diffusion mechanism. In the case of interstitial-substitutional diffusion, also called dissociative diffusion, impurities occupy substitutional as well as interstitial sites. The interstitial impurity component diffuses rapidly. It dominates in most cases the overall diffusion even though it may be a small fraction of the total impurity concentration. The triple acceptor Cu in Ge is a typical case for this mechanism. The interstitialcy mode of diffusion results from a substitutional impurity atom being displaced by a host lattice interstitial atom to an interstitial site. The interstitial impurity diffuses rapidly some distance before returning to a substitutional site creating a new host lattice interstitial. This is the dominant mechanism for most impurities diffusing in Si.

In some cases, a combination of the above four mechanisms may also occur within in a crystal. The diffusion processes of various impurities and self-diffusion have been investigated in Si for quite some time (Tan and Gösele 1985, Wolf and Tauber 1986). More recently, self-diffusion has been investigated in isotopically controlled Ge, Si and AlGaAs/GaAs multilayer structures (Fuchs et al. 1995, Bracht et al. 1998a, Wang et al. 1996, Bracht et al. 1998b). Diffusion mechanisms of Zn and Si in GaAs have been studied in great detail (Gösele 1981, Reynolds 1988). A comprehensive study of the

atomic diffusion processes of Zn and Be at heterointerfaces in lattice-matched InGaAs/InP heterostructures has been reported (Bracht et al. 1998c).

1.1.5 Diodes and transistors

The basic building block for semiconductor devices is the p-n junction. As is suggested by its name this device consists of adjacent p- and n-type regions in one crystal. The p-n junction diode is a two terminal device.

When n- and p-type materials are brought in contact, electrons will flow from the n-type region to the p-type region and holes will diffuse from the p-type region to the n-type region due to the large respective concentration gradients. As a result of this diffusion an electric field is generated resulting in the bending of the bands (Fig. 1.2(a)). A potential barrier is formed across the junction inhibiting the net flow of electrons and holes between the p-type and the n-type regions.

If a forward bias voltage $\mathbf{V_a}$ is applied to the p-n junction the barrier $\mathbf{\Delta E}$ is reduced (Fig. 1.2(b)). Under this forward bias condition the net current that flows across the p-n junction increases exponentially with voltage:

$$I = I_o\left(\exp\frac{qV_a}{kT} - 1\right) \tag{1.9}$$

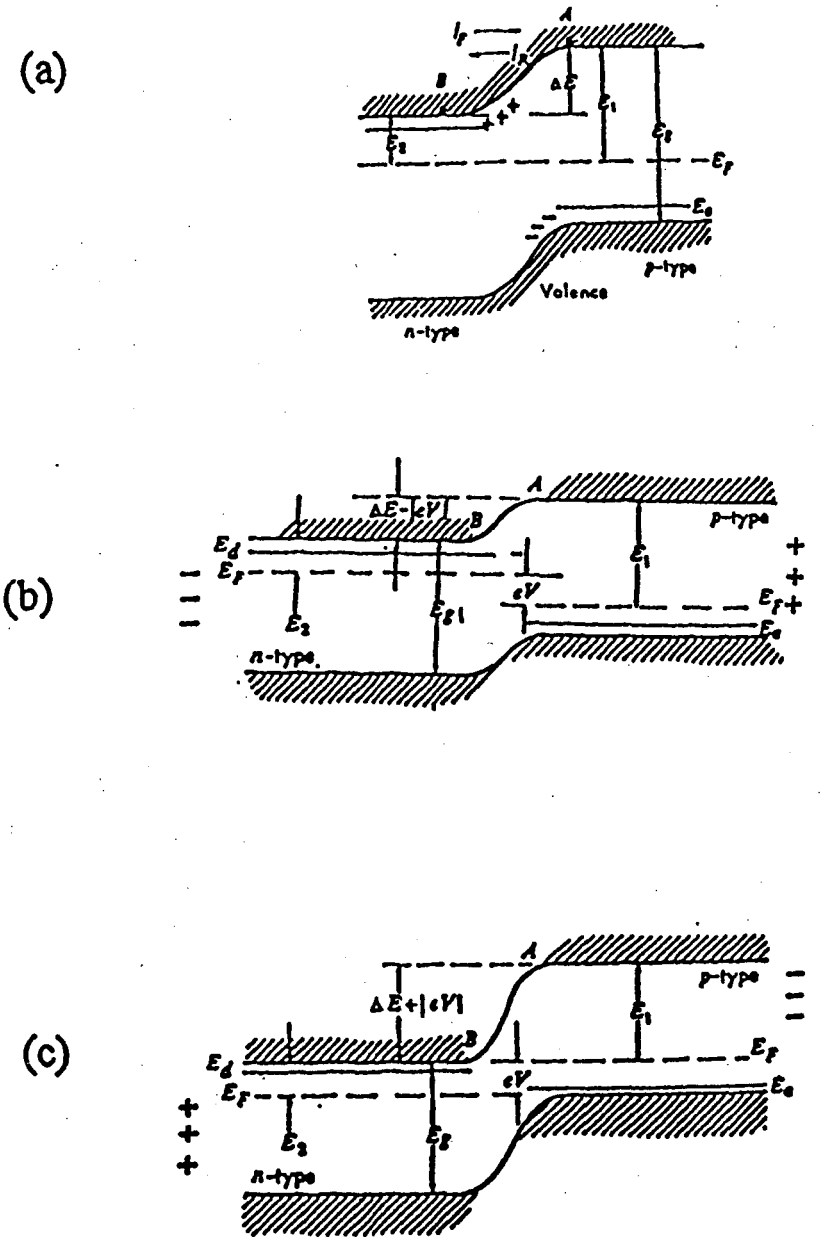

Fig. 1.2 Band structure of a p-n junction (a) at equilibrium, (b) under forward applied bias, and (c) under reverse applied bias. (Barrett et al. 1973)

If a reverse bias is applied to the p-n junction the barrier is increased (Fig. 1.2(c)). For a large reverse bias voltage the current in the p-n junction is limited by the reverse saturation current. The sources of the reverse current are the minority carriers in the p and n-regions. Their concentration is independent of the magnitude of the applied voltage but strongly dependent on doping and on temperature. The salient feature of the p-n junction diode is its ability to conduct large currents in the forward bias direction while it blocks current flow in the reverse bias direction. This nonlinearity is widely used to rectify alternating currents.

A light-emitting diode is a p-n junction device which can efficiently convert electrical energy into light (Grovenor 1989). The semiconductor materials chosen for these types of optical applications are selected based on the efficiency of the radiative processes in the material and the wavelength of the light which is emitted.

Since GaAs is a direct band gap semiconductor, photons can induce electron transitions without the need of phonon creation and/or annihilation for momentum conservation. Conversely, electron and holes can be injected into a GaAs diode and can recombine to generate photons. It is this efficient photon generation which has made GaAs and its many alloys one of the most important semiconductor materials for opto-electronic applications.

In a photodiode detector, the objective is to absorb photons and generate electron-hole pairs in the region where there is a high electric field. The photogenerated carriers are swept out by the electric field and a current signal in the external circuit is generated. For photodetection in the 1.2-1.6 μm range both Ge and $In_{0.53}Ga_{0.47}As$ (lattice-matched to InP) are the materials of choice due to their large absorption coefficients (Fig. A.2).

Another type of electronic device is the field effect transistor which consists of a channel that lies between the source and the drain. The current flow in the channel is controlled by the gate. The source and drains are both diffused or implanted junctions. The source supplies electrons to the channel which flow towards the drain. The bias on the gate modulates the conductivity of the channel. A complementary metal oxide structure field effect transistor (MOSFET) in the "off" and "on" state is illustrated in Fig. 1.3. The source and drain are electrically disconnected unless there is an n-type inversion layer at the oxide/semiconductor interface to provide a conducting channel between them. The gate switches the transistor on when a positive voltage is applied. This attracts electrons to the oxide/semiconductor interface. The transistor is in the "on" state when an electron flow is established from the source to the drain. This type of MOSFET is called an "enhancement-mode" device since a gate voltage must be provided to induce a channel. While, in a "depletion-mode" device a gate voltage is used to reduce the conductance of the built-in channel (Muller 1986).

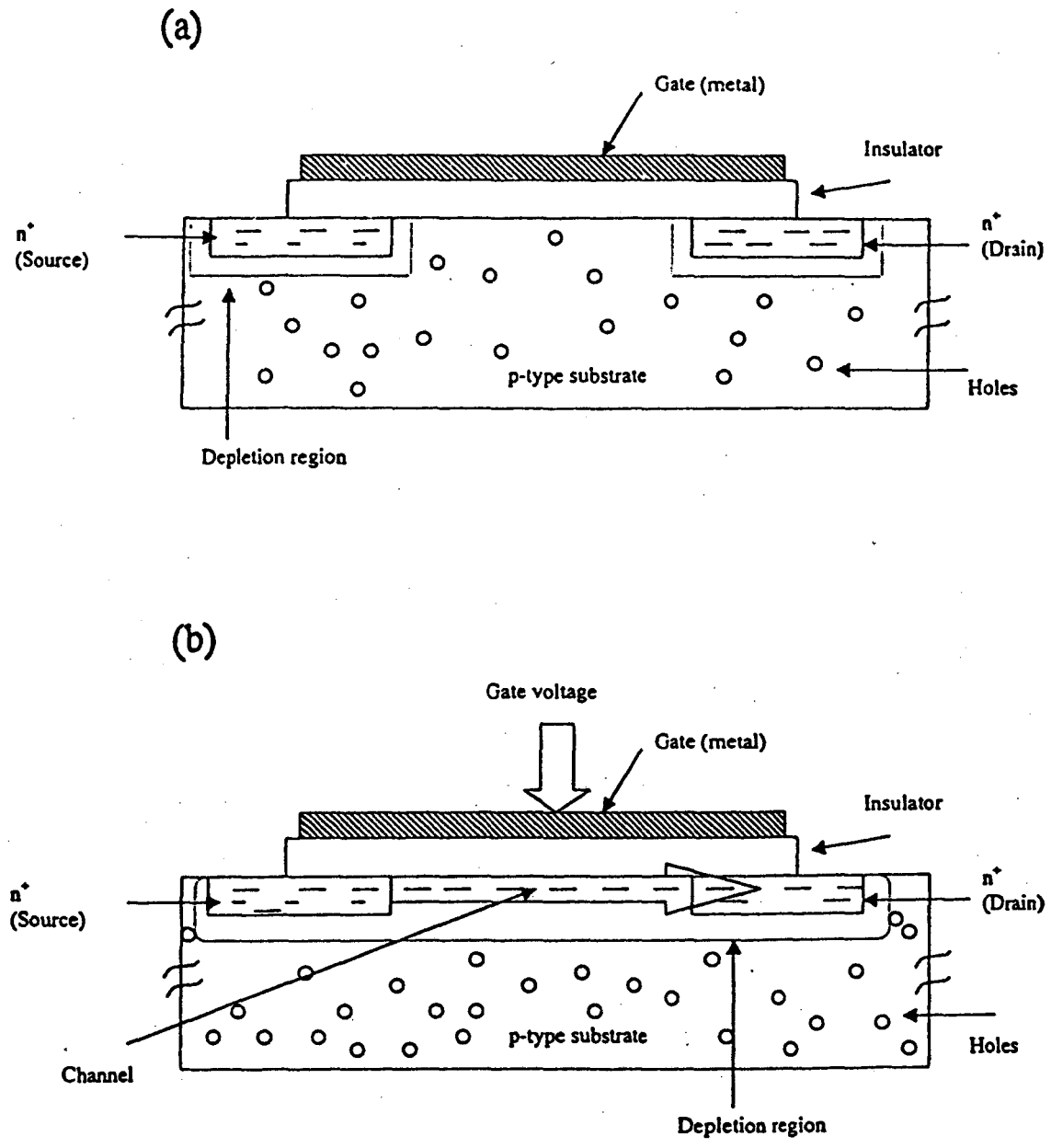

Fig. 1.3 Schematic of a MOSFET structure in the (a) "off" and (b) "on" state (accumulation mode).

1.1.6 Integrated circuits

An integrated circuit consists of a large assembly of individual diodes, transistors, resistors, and capacitors all on one chip. These components may form a microprocessor, a memory, and other types of devices. An array of these devices on one piece of silicon constitute a "chip".

Device fabrication originates with the growth of single crystals of Si. The crystals are grown from a melt at temperatures near 1420°C. In this crystal growth process, a seed crystal is first inserted into the Silicon melt. After equilibration the seed is slowly withdrawn from the melt. Crystal growth occurs by solidification at the interface between the solid Si and the melt. Following crystal growth the ingot is sliced into wafers about 0.725 mm thick. To eliminate surface imperfections, the wafers are polished with a slurry until a mirror smooth surface is obtained. These polished wafers are then ready to be used as substrates for integrated circuits. At present, most of the wafers are 200 mm (8 inch) in diameter, but the semiconductor industry is moving towards 300 mm wafers which would lead to an increase in yield of number of chips produced per wafer and reduction in cost per chip.

The core of the IC fabrication process is based on the repeated application of a number of basic semiconductor processing steps which include: oxidation, photolithography, etching, diffusion, evaporation or sputtering, chemical vapor deposition, ion implantation, and epitaxy.

One of the most attractive properties of Si is its ability to grow a native oxide layer. This native oxide layer serves both as an electrical insulator and as a barrier to impurity diffusion. These two properties of the silicon dioxide layer have allowed Si to

become the most widely used semiconductor substrate for the fabrication of integrated circuits. This SiO_2 layer is grown by placing the wafer in a quartz-tube furnace in an oxidizing atmosphere containing either pure oxygen or water vapor at temperatures of 900 to 1200°C. Typical furnaces may have a three zone temperature control feature which enables the furnace to maintain the temperature within a fraction of a degree over a distance of 0.5 m in the center zone (Jaeger 1988).

Photolithography is used to define the circuit pattern on each layer of a chip. The wafer is coated with photoresist, a light-sensitive organic film. Spin coating is the most common method of applying photoresist on a wafer. The wafer is mounted on a vacuum chuck which contains a number of small holes in its surface. The vacuum chuck design allows for an intimate contact between the wafer and the chuck when vacuum is obtained. A spigot deposits a precise amount of photoresist material on the surface of the wafer. The wafer is spun at speeds of 1000 to 5000 rpm for 30 to 60 sec to produce a thin uniform layer (Jaeger 1988). Softbaking or prebaking is performed to remove the solvent and improve adhesion. Exposure of the photoresist is achieved using a stepper which transfers the image on mask to the wafer. The stepper has a sophisticated lens system to reduce the pattern on the mask to the microscopic dimensions required for the circuitry of the chip. The photoresist is exposed by ultraviolet light that passes through the mask. In the case of positive resist, exposure to the uv light results in bond breaking. The exposed resist is subsequently removed using a solvent. Negative resist remains in regions which have been exposed to the uv light. Once the photoresist has been patterned, the wafer is ready for etching.

Wet or dry etching techniques can be used to remove SiO_2 in selected regions which have not been protected by the hardened photoresist. A buffered oxide etch is a solution which contains hydrofluoric acid which etches SiO_2. Wet etching techniques tend to be isotropic in nature, whereas highly anisotropic etch profiles can be achieved using dry etching processes. A few of these dry etching processes include: plasma, sputtering, and reactive ion etching. After etching is completed, the protective layer of photoresist is removed.

Dopants which are used to form the n-type and p-type regions are introduced into the Si wafer by ion implantation and/or diffusion. Ion implantation and diffusion was discussed in depth in sections 2.1 and 1.1.4, respectively.

The individual electronic devices are interconnected by metal or by doped poly Silicon lines. Aluminum is typically chosen for this application due to its high electrical conductivity and its ability to form a protective oxide layer on the top surface (Mayer et al. 1990). More recently, IBM has introduced products into the marketplace which utilize copper interconnects. The driving force for this innovation is the lower electrical resistivity of copper (1.67×10^{-8} Ω m) as compared to that of aluminum (2.65×10^{-8} Ω m). The lower resistance reduces RC delays and improves the high frequency performance of the chip.

The final stages in the fabrication of ICs consist of assembly and packaging. A dicing machine cuts up the wafer into the individual chips (die). The chips are then mounted using an epoxy or by eutectic bonding on to the packaging units which contain metal leads. Wire bonding is used to make the electrical connections between the bonding pads on the die and the leads on the package.

1.2 Motivation for the study of ion implantation for electrical isolation

Electrical isolation is employed in integrated circuits to restrict parasitic current flow between neighboring devices or between the substrate and specific parts of a device. In addition, electrical isolation reduces the effects of parasitic capacitances and resistances (Williams 1990).

Electrical isolation is typically achieved by ion implantation or mesa etching. In implant isolation, the undesired conductive material is rendered semi-insulating by irradiation induced damage related defect levels (inert noble gas or isoelectronic ions) or the electrical activation of impurities which have an electronic deep level in the bandgap. Deep level centers are formed which compensate the shallow dopants. Carrier mobilities are decreased because of the increased ionized defect scattering.

Mesa etching involves etching away portions of the electrically active surface layer of the wafer and leaving "mesas" of the active layer. For device isolation, ion implantation is an attractive alternative to mesa etching because it maintains a planar structure. This is highly desirable in the fabrication of devices and wafer processing, because it allows for more flexibility in multi-layer circuit design and fabrication. In addition, implant isolation intrudes less under mask edges than mesa etching (Pearton 1990).

In GaAs integrated circuits, implant isolation has been used to reduce the backgating effect (D'Avanzo et al. 1982 and de Souza et al. 1992). Backgating involves the electrical interaction between neighboring devices by applying a negative bias to closely spaced n-type contacts. An expansion of the depletion region at the interface occurs which tends to gate the device from the backside. It results in a reduction of the

drain-to-source current in a field effect transistor by biasing the substrate-active layer interface.

It is of particular interest to develop ion implantation and annealing techniques for forming high resistivity InGaAs layers which are compatible with typical integrated circuit and device fabrication processes. Due to the small band gap (0.75 eV at 300K) of InGaAs, this semiconductor alloy has an intrinsic carrier concentration which is high in comparison to GaAs and InP (Table A.2). The calculated intrinsic resistivity is approximately 900 Ohm-cm (using values of 10,000 and 300 $cm^2\ V^{-1}\ s^{-1}$ for electron and hole mobilities, respectively). Therefore, to increase the resistivity of the InGaAs layers beyond intrinsic values it is essential to reduce both the free carrier concentration and the mobility as much as possible.

1.3 Properties and device applications of $In_{0.53}Ga_{0.47}As$

$In_{0.53}Ga_{0.47}As$ is lattice-matched to InP. It is a promising material for electronic and optoelectronic applications. Very high electron mobility, high electron saturation velocity, and a large intervalley separation in the conduction band are a few of its attractive material properties as compared to other III-V materials and alloys (Table A.2).

$In_xGa_{1-x}As$ is a direct band gap semiconductor over the entire composition range. Its direct band gap means rapid photon absorption near the surface. Only thin layers are needed to absorb most photons. In addition, the band gap (0.75 eV [1.67 μm] at 300K) is well matched to 1.3-1.55 μm wavelength radiation for which the silica fibers exhibit the lowest loss in optical transmission. As a result, it is used for the development of detectors for optical communication.

In a typical long wavelength p-i-n diode, $In_{0.53}Ga_{0.47}As$ is the light absorbing semiconductor material. Up to 98% of the incident radiation can generate electron-hole pairs in the active region (Mayer et al. 1990). Surface recombination can lead to large photocurrent losses. Top-illuminated p-i-n diodes with a transparent cap of InP have minimal loss of efficiency arising from absorption outside of the depletion region, since the InP is transparent to all wavelengths above 0.92 μm. Fig. 1.4 shows the typical structure of an $In_{0.53}Ga_{0.47}As$ p-i-n diode. The spectral response at room temperature for a Ge and $In_{0.53}Ga_{0.47}As$ p-i-n diodes are shown in Fig. 1.5. For the Ge photodiode, a slowly rising response is observed starting at 1.8 μm due to the indirect band gap. Its direct band gap absorption near 1.5 μm results in a larger response at this wavelength. The spectral response at smaller wavelengths can be improved for the $In_{0.53}Ga_{0.47}As$ p-i-n diode with the use of a wide band gap window (shown by the dashed curve).

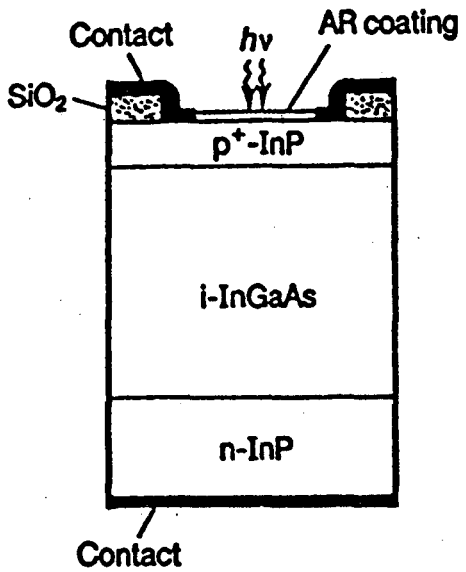

Fig. 1.4 An $In_{0.53}Ga_{0.47}As$/InP p-i-n photodiode structure. (Wood 1994)

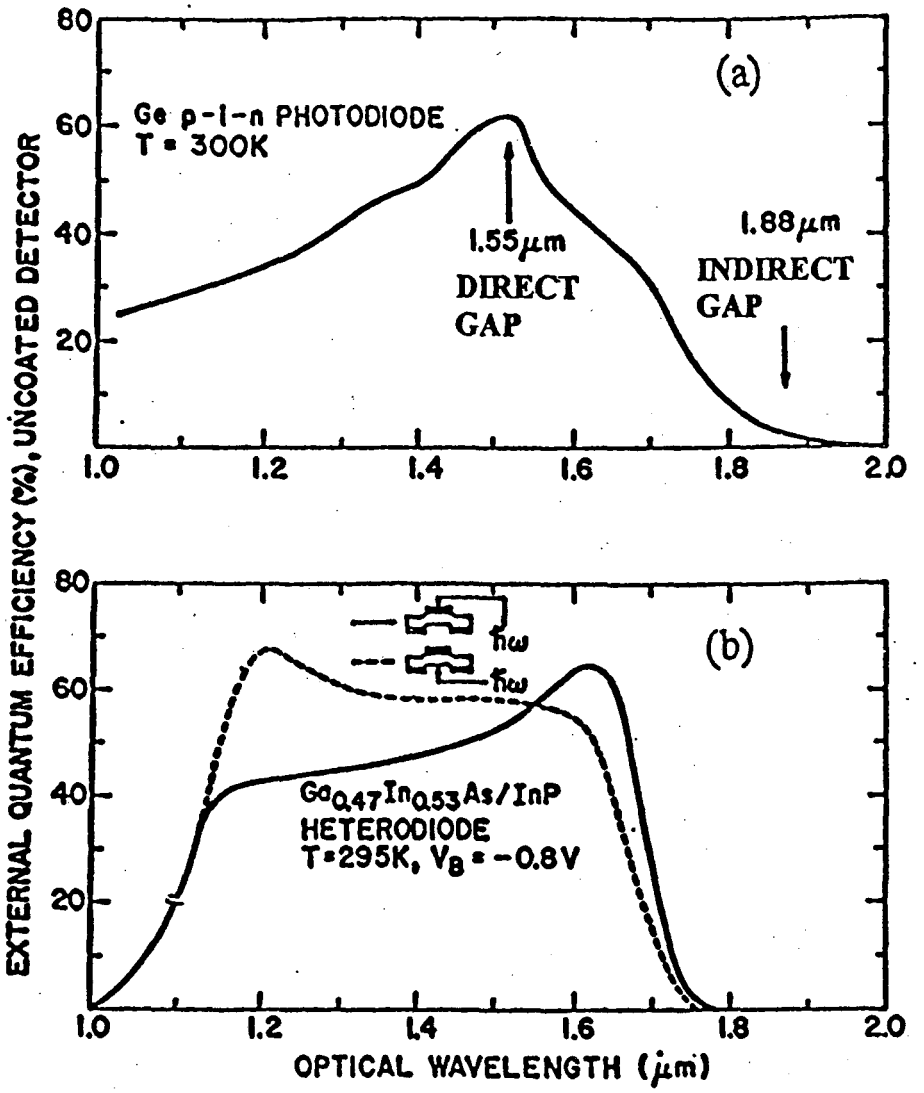

Fig. 1.5 Spectral response at room temperature of a (a) Ge and (b) $In_{0.53}Ga_{0.47}As$ photodiode.

1.4 Technological interests in high resistivity layers

High resistivity $In_{0.53}Ga_{0.47}As$ epilayers are desirable for a wide variety of semiconductor device applications. The response time and speed of InGaAs based photodiodes are often degraded by the RC time constant of the detector/external circuit and excess leakage currents (Akano et al. 1996). A trench technique is usually employed to improve device performance which consists of etching a deep trench around the active volume of the photodetector to produce an isolating region. This etching process enhances device performance, but results in a nonplanar geometry. High resistivity $In_{0.53}Ga_{0.47}As$ layers produced by ion implantation is an attractive alternative approach because it allows for planar processing which could potentially increase device yields and provides for flexibility in device layout.

In addition to device isolation, high resistivity layers are of particular interest for high-speed metal-semiconductor-metal (MSM) photodetectors (Böttcher et al. 1992 and Kuhl et al. 1990). A MSM photodetector is a planar structure with two top metal contacts (Wood 1994). It essentially consists of two back-to-back Schottky diodes. A Schottky diode is a metal-semiconductor junction which exhibits properties similar to a p-n junction which was discussed in section 1.1.5. Hence, the I-V characteristics and the rectifying behavior for the Schottky diode follow that of the p-n junction. For long wavelength detectors, the low Schottky barrier height of InGaAs (0.2 eV) results in large leakage currents. There are two approaches to overcome this problem (Kuhl et al. 1990, Böttcher et al. 1992). One approach involves using a barrier enhancement layer which has a larger bandgap than InGaAs, such as AlInAs, between the metal and InGaAs. The use of this cap layer followed by a graded InGaAlAs transition region can increase the

barrier height and reduce leakage currents. Alternatively, a high resistivity InGaAs absorbing layer may be used.

2 Review of ion implantation for electrical isolation of III-V semiconductors and alloys

2.1 Ion implantation basics

Ion implantation has evolved into one of the most essential processes for the fabrication of integrated circuits using Si and III-V compound semiconductors. There are two important applications of ion implantation with respect to compound semiconductors. First, implantation of dopant ions is used to establish the desired n-type or p-type conductivity. Second, the implantation of ions to convert a conductive layer into a highly resistive one. The latter one is referred to as "implant isolation".

Ion implantation is a process in which energetic impurity ions are introduced into a single crystal substrate in order to change its electronic properties. Comprehensive reviews of ion implantation can be found in many articles and textbooks (Ghandi 1994, Mayer 1970, Williams 1984). Implantation is typically performed with ion energies in the 30-200 keV range, but for modern shallow junctions the energy may be as low as a few keV. The ion dose can be tightly controlled by measuring the ion current. Some of the advantages of ion implantation include: control of dopant impurity species, control of doping concentration, control of implanted thickness layer, choice of dopant profile through multiple implants at different doses and energies, and high throughput. In addition, regions of the substrate can be implanted selectively by using masking materials. One of the significant advantages of ion implantation is that it is a "low" temperature process (relatively speaking) which limits the diffusion of the implanted

species. Currently, one of the foci of ion implantation research is to devise better methods to activate the implanted dopants and remove the damage, while minimizing the amount of dopant diffusion.

The basic components of an ion implanter consist of an ion source, mass spectrometer, high voltage accelerator, scanning system and target chamber. The ion source produces a plasma containing the desired impurity ions, as well as other atomic and molecular species. The impurity atoms are ionized by collision with energetic electrons emitted from a hot filament. A magnetic field is provided to increase the ionization efficiency of the source. The positive dopant ions are accelerated to the exit side of the source chamber which is biased at a large negative potential (15-20 kV) with respect to the filament. Consequently, the ion source also serves as preacceleration stage supplying ions with energies ranging between 15 to 20 keV. The mass spectrometer selects the impurity ion species of interest. The electric field along the accelerator column imparts energy to the impurity ions. Pairs of x- and y-axis deflection plates are used to scan the beam across the wafer to produce a uniform implantation dose. Good electrical contact is made between the wafer and the target holder. In this manner, electrons can flow to or from the wafer to neutralize the implanted ions. The electron current **I** is integrated over time **t** to measure the total dose:

$$Q = \int_0^t I \frac{dt}{nqA} \tag{2.1}$$

where **A** is the wafer area and **n** is 1 for singly ionized ions and 2 for double ionized species. To accurately measure the dose, precautions must be taken to minimize errors due to secondary electrons. Secondary electrons can be emitted as a result of the ion

bombardment of the target. To minimize secondary electron dose errors, the wafer is biased with a small positive voltage (i.e., tens of volts).

Energy loss processes determine the final depth distribution of the energetic ions inside the solid and the amount of lattice disorder produced. We distinguish between two types of energy loss processes: electronic and nuclear. Electronic energy loss involves the interaction between the incident ions and the electrons of the host material. Owing to the small masses of the electrons, electronic collisions lead to a negligible deflection of the ion trajectory. Nuclear energy loss involves the nuclear interaction between the incident ions and the host atoms. Nuclear collisions result in large angle deflections of the ion trajectory and displacements of the target atoms resulting in crystalline damage in the target.

The range and distribution of implanted ions can be calculated by the Lindhard, Scharff, and Schiøtt (LSS) theory (Lindhart et al. 1963). This theory finds that for heavy ions and at energies lower than ~ 200 keV nuclear stopping is more important than electronic stopping. On the other hand, electronic stopping is more important for lighter ions and higher energies. Figure 2.1 illustrates the dependence of the nuclear and electronic energy loss rate on the energy of the projectile. It can be seen that nuclear collisions dominate at low energies and electronic collisions at higher energies. In the energy range where nuclear stopping dominates, host atoms are displaced. Nuclear stopping is usually treated as a classical elastic collision problem between charged particles with an appropriate screening factor to take into account the surrounding electrons. Over the range considered, nuclear stopping is generally not a strong function of the energy of the projectile. Interaction with the crystal is a statistical process, and the

implanted impurity profile can be approximated by a Gaussian distribution. This approximation assumes an amorphous target material. The atomic density of the implanted atoms as a function of depth is given by LSS:

$$n(x) = \frac{\varphi}{\sigma_p \sqrt{2\pi}} \exp\left[-\frac{(x - R_p)^2}{2\sigma_p^2} \right] \tag{2.2}$$

where φ is the implanted dose (atoms/cm^2), σ_p is the standard deviation in the projected range (or straggle), and R_p is the projected range. The above approximation ignores any effects caused by guidance of the ions along specific crystalline orientations in so-called channels. The projected range depends on the velocity of the ion and the stopping power of the substrate material. For implants of a given incident energy, a high mass ion (low velocity) will come to rest closer to the surface, whereas, a lower mass ion (high velocity) will have a larger penetration depth.

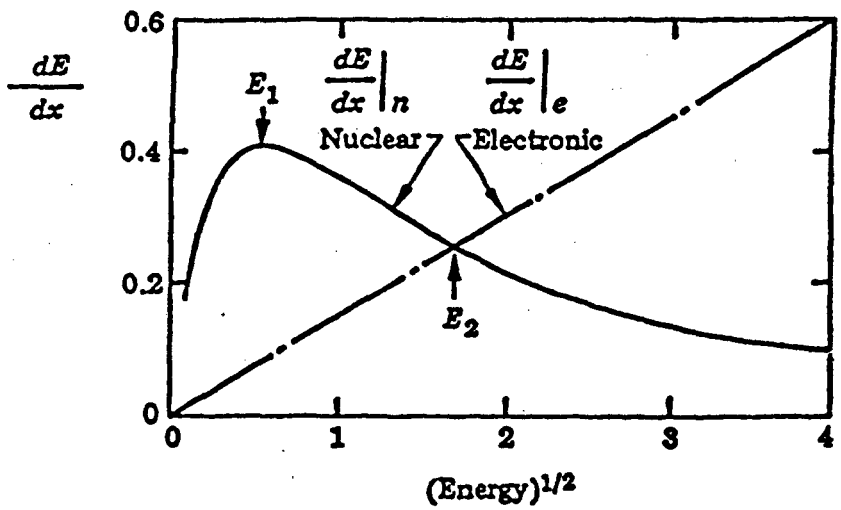

Fig. 2.1 Rate of energy loss (dE/dx) versus (Energy)$^{1/2}$ showing nuclear and electronic loss contributions. (Mayer et al 1990)

Some further issues that must be addressed with ion implantation are channeling and beam annealing. Channeling occurs in a single crystal when the ion beam is aligned with an axis of the crystal and is steered into the open spaces (Tesmer et al. 1995). The steering is due to the small-angle screened Coulombic collisions between the ions and the host atoms along the channel. Channeling results in non-Gaussian implant profiles with long tails. To avoid channeling the crystal is generally misaligned, so that the ions are incident in a nonchanneling direction. In this manner, the crystalline target approximates an amorphous target. Furthermore, high ion implantation dose rates can lead to a substantial rise in target temperature due to the high power injection into the specimen by the ion beam. The temperature of the implant is crucial because it affects the diffusion of both the implanted ions and the defects.

2.2 Implantation Damage

Implantation damage in semiconductors has been studied in great detail (Ghandi 1994, Jaeger 1988). During ion implantation, the energetic impurity ions undergo many collisions with host atoms before coming to rest. As a result, many atoms are displaced, some of which in turn displace further host atoms resulting in a cascade of atomic collisions. This leads to the formation of vacancies, interstitial atoms, amorphous regions, and other types of defects. The number of displaced atoms can be calculated assuming a hard-sphere model for the elastic collisions. The displacement energy $\mathbf{E_d}$ is the energy required to knock an atom off its lattice site. The displacement energy for Si and GaAs is 14 -15 eV. If the lattice atom receives an energy of less than $\mathbf{E_d}$ the host atom will not be displaced. In addition, if the incident ion recoils with an energy less than $\mathbf{E_d}$, it will not displace any additional atoms. Therefore, to observe a net increase in

the number of displaced host atoms the incident ion must have an energy greater than $2E_d$. Assuming no additional energy loss mechanisms, the number of host atoms displaced by the incident ion is:

$$N_d = \frac{E_o}{2E_d} \tag{2.3}$$

where E_o is the incident ion energy.

Damage effects in GaAs are more complex than in Si due to the binary nature of the compound. The host atoms recoil differently due to the difference in atomic weights between Ga (69,71) and As (75). As a result, there remains an excess of the heavier element (As) closer to the surface. It has been reported that the difference in annealing of damage between Si and GaAs may be attributed to the non-stoichiometry in the ion implanted layers (Gamo et al. 1977). Annealing of heavy ion implant damage in GaAs results in highly twinned material (Almonte 1996).

For electrical isolation purposes, implant damage can be beneficial. For instance, ion implantation damage in GaAs is used to produce semi-insulating material with a carrier concentration which is of the order of 10^{11} cm^{-3}.

2.3 *Fundamentals of implant isolation and mechanisms for achieving high resistivity layers*

There are two ways to achieve isolation using implantation: deep level formation through lattice damage or through the introduction of deep level impurities. Lattice damage in the epilayers can be created by the bombardment with energetic inert or isoelectronic ions. In this manner, the defects form deep levels which compensate shallow dopants. Due to free carrier scattering with these defects also the mobility drops.

In general, in most III-V semiconductors, ion implantation induces Fermi level shifts towards the midgap of the semiconductor. However, there are some exceptions which include InAs where the implantation induced defects shift the Fermi level into the conduction band, and in $In_{0.53}Ga_{0.47}As$ where the Fermi level shifts to the upper 1/3 of the bandgap. Fermi level shifts in irradiated semiconductors will be discussed in greater detail in section 2.4.

Compensation of dopants can also be achieved through the implantation and activation of deep level impurities. N-type materials must be implanted with deep acceptors while p-type semiconductors require deep donors to achieve effective compensation.

The compensation of residual impurities by shallow impurities of opposite type cannot be achieved with sufficient precision to produce semi-insulating material. Doped semiconductors can be made semi-insulating, if they are counter-doped appropriately with a deep impurity of opposite conductivity type, whose impurity level is close to the middle of the bandgap.

2.4 Heavily damaged III-V semiconductors and amphoteric native defects

The electrical properties of GaAs and InP, irradiated with large electron doses, have been reported (Brudynl et al. 1982). N-type (Te doped $n\sim10^{16}cm^{-3}$), p-type (Zn doped $p\sim10^{16}cm^{-3}$), and semi-insulating (Cr doped) GaAs samples were irradiated with electrons with energies between 2.2 and 2.3 MeV and doses up to $10^{19}cm^{-3}$. For irradiation doses of up to $10^{18}cm^{-3}$, an increase in resistivity to the range of 10^{9} Ω–cm with an accompanying shift of the Fermi level position towards the middle of the

bandgap (~0.7 eV) was observed. The Fermi level (E_F) position was dependent upon irradiation conditions only and did not depend on the original doping conditions of the samples (Fig. 2.2). Similar electron irradiation experiments performed on InP revealed a Fermi level shift towards the upper one third of the bandgap (~1.0 eV) (Fig. 2.3).

The final position of the Fermi level in a heavily damaged semiconductor is defined as the Fermi Stabilization Energy (E_{FS}). Fig. 2.4 shows E_{FS} for various III-V semiconductors. E_{FS} is almost constant for all III-V semiconductors when measured with respect to the vacuum level and lies 4.9 eV below this level. The Fermi stabilization level is located in the upper 1/3 of the bandgap for ion irradiated $In_{0.53}Ga_{0.47}As$. The damage related levels consist of a distribution of energy levels. Ion irradiation leads to an increase in carrier concentration because energy levels in the upper end of the distribution merge with the conduction band edge and act as donors.

The position of E_{FS} within the bandgap is an important material property worthy of consideration when studying implant isolation of III-V semiconductors. If the E_{FS} is located near the middle of the bandgap, the effect of irradiation will be to compensate both p-type and n-type layers. On the other hand, if the E_{FS} is found closer to the conduction band or the valence band, irradiation will lead to an increase in the free electron or hole concentrations, respectively.

The E_{FS} in heavily damaged semiconductors can best be explained by the amphoteric native defect model (Walukiewicz 1989 and 1993). Amphoteric native defects change their electrical characteristics depending on the position of the Fermi level. As can be observed in Fig. 2.2, a large concentration of native defects always leads to the same ultimate position of the Fermi level in GaAs. Fig. 2.5 shows the defect

formation energies for vacancies and complex defects in GaAs. The $\mathbf{E_{FS}}$ position is controlled by the following defect reactions for the Ga sublattice and As sublattice, respectively:

$$V_{Ga}+As_{As}\leftrightarrow As_{Ga}+V_{As} \quad (2.4)$$

$$Ga_{As}+V_{Ga}\leftrightarrow V_{As}+Ga_{Ga} \quad (2.5)$$

The formation energy of charged native defects depends on $|\mathbf{E_F}-\mathbf{E_{FS}}|$. For n-type GaAs acceptor-like defects (V_{Ga}, $Ga_{As}+V_{Ga}$) are predominantly formed. Whereas, donor-like defects (V_{As}, $As_{Ga}+V_{As}$) are formed in p-type GaAs. When the formation rates for both types of defects are equal an equilibrium will be reached, and the Fermi level will be stabilized.

The amphoteric native defect model has been used to explain Schottky barrier heights, doping induced superlattice intermixing, and maximum free carrier concentrations which can be achieved in III-V semiconductors (Walukiewicz 1987, 1988a, 1988b, 1989).

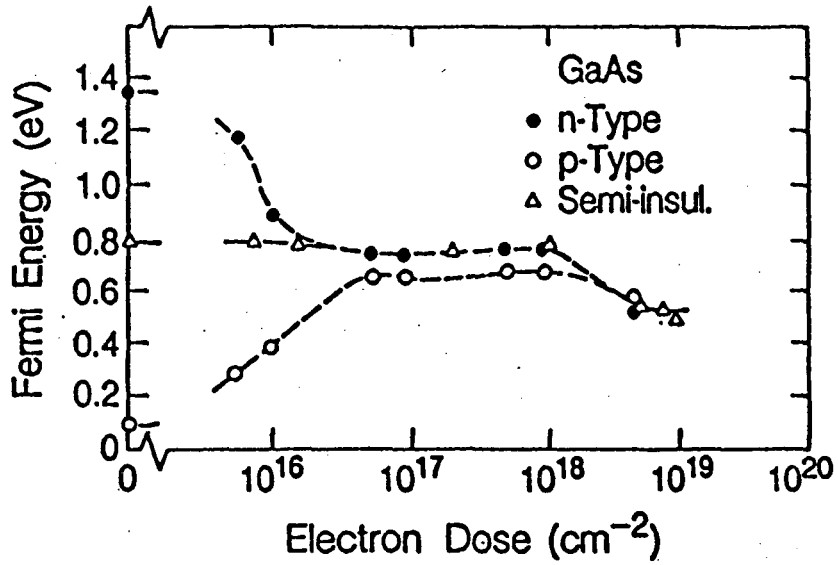

Fig. 2.2 Fermi level position in electron irradiated GaAs as a function of electron dose. (Brudynl et al. 1982)

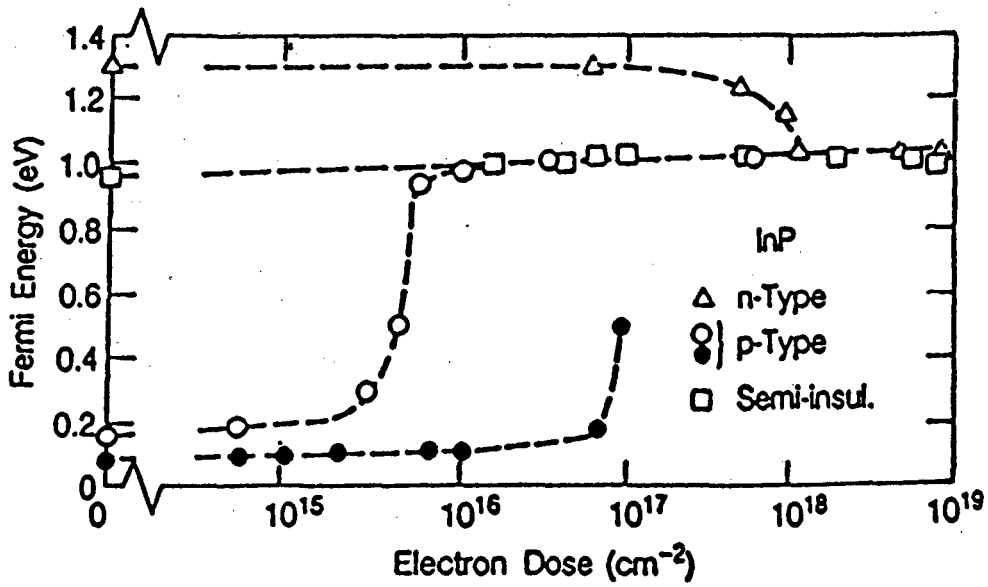

Fig. 2.3 Fermi level position in electron irradiated InP as a function of electron dose. (Brudynl et al. 1982)

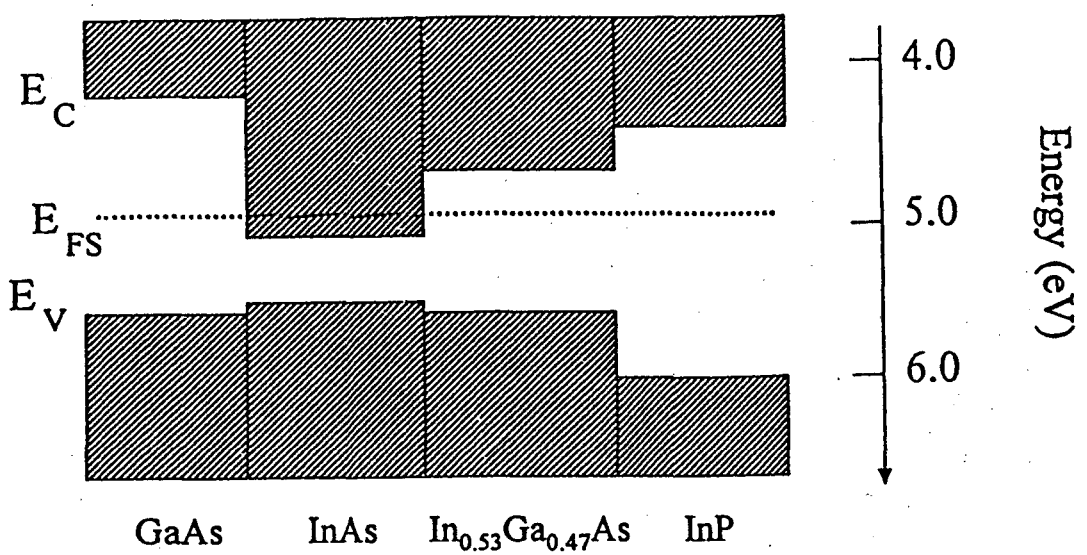

Fig. 2.4 Fermi level stabilization energies for III-V semiconductors. (Walukiewicz 1993)

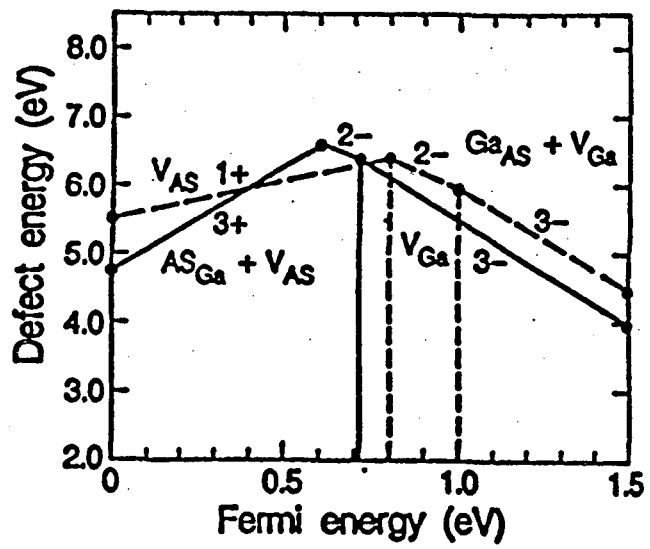

Fig. 2.5 Defect formation energies of simple vacancies and complex defects. The maximum of the curve corresponds to the Fermi Stabilization energy for a given defect system. (Walukiewicz 1989)

2.5 Semi-insulating bulk crystals and diffusion of transition metal impurities in GaAs and InP

The technological importance of semi-insulating (SI) material is based on the fact that devices fabricated on SI GaAs substrates are self-isolating and ideally suited for integrated circuit fabrication. Field effect transistors produced on SI GaAs substrates have a much lower drain capacitance than those fabricated on doped substrates and are therefore faster.

Chemical impurities which form midgap levels in GaAs and have been used to produce SI GaAs include O, Cr, and the native defect EL2 . Oxygen exhibits two energy levels in GaAs (E_c-0.14eV, E_c-0.57 to 0.75eV) and has a solid solubility greater than $10^{17}cm^{-3}$ (Skowronski et al. 1990). Resistivities of the order of 10^8 Ω-cm can be obtained with n-type GaAs which has been doped with O. There have been many theories proposed to explain the electrical behavior of O in n-type GaAs. One of the theories suggests that O bonds with Si_{Ga} (which is the dominant donor impurity in n-type GaAs) to form inactive Si-O complexes. As a result, the donors are passivated and the material becomes p-type. The excess O is ionized and the Fermi level shifts towards the midgap. One of the experimental findings which lends support to this theory is that O doped SI GaAs exhibits a relatively high mobility (4000 $cm^2\ V^{-1}\ s^{-1}$). A highly compensated material would not have such a high mobility as is observed in this case. Unfortunately, it is impractical to use O as a dopant to produce SI GaAs, because it is a highly mobile impurity at temperatures above 650°C which are required for device processing.

Cr in GaAs behaves as a single acceptor and its energy level lies 0.79 eV above the valence band top (Martin et al. 1980). Resistivities as high as 10^9 Ω–cm can be

achieved with Cr doping of n-type GaAs (Grand 1982). Outdiffusion of Cr to the surface and subsequent loss of semi-insulating properties have been observed upon high temperature annealing of Cr doped GaAs (Lindquist 1977). Radio tracer diffusion experiments suggest that Cr diffuses through the lattice interstitially (Tuck et al. 1979). Of particular interest is the redistribution of Cr in implanted GaAs substrates. Pileup of Cr near the peak of the damage formed by ion implantation has been observed and explained by defect gettering effects (Evans et al. 1980).

In the 1980's, successful growth of LEC GaAs with EL2 reduced the role of SI Cr-doped GaAs. The net impurities in high purity LEC-grown GaAs are p-type with concentrations in the range of $5x10^{14}$-$10^{15}cm^{-3}$ (Oliver 1981, Hunter 1984). The native defect, EL2, is a deep donor in GaAs and exhibits an energy level which lies 0.75 eV below the conduction band. This defect is stable at temperatures up to 950°C. EL2 has been observed in LEC GaAs crystals grown with greater than 0.475 As atom fraction in the melt. Fig. 2.6 illustrates the dependence of resistivity and free carrier concentration of LEC undoped GaAs on As atom fraction in the melt (Holmes et al. 1982). The crystal is p-type below 0.475 As atom fraction and semi-insulating above it. EL2 concentrations ranging from $5x10^{15}cm^{-3}$ to $1.7x10^{16}cm^{-3}$ have been observed (Fig. 2.7). Studies have confirmed that EL2 involves the native defect As_{Ga} (Lagowski et al. 1982 and Weber 1982). However, controversy still exists as to whether EL2 is the isolated As_{Ga} itself or a complex of two more defects, one of which is the anti-site.

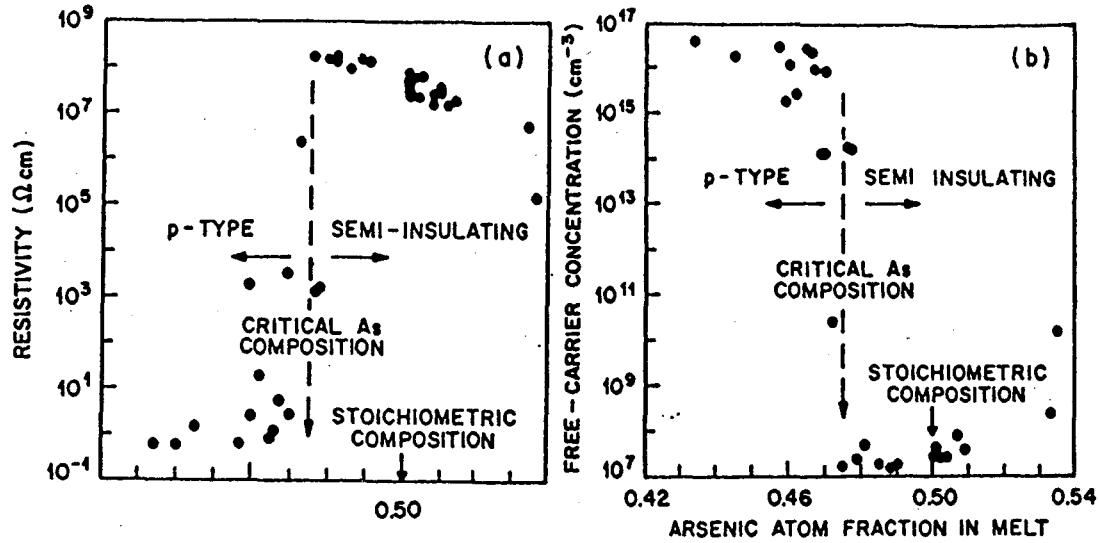

Fig. 2.6 Variation of electrical resistivity (a) and carrier concentration (b) of LEC GaAs with melt stoichiometry. (Holmes et al. 1982)

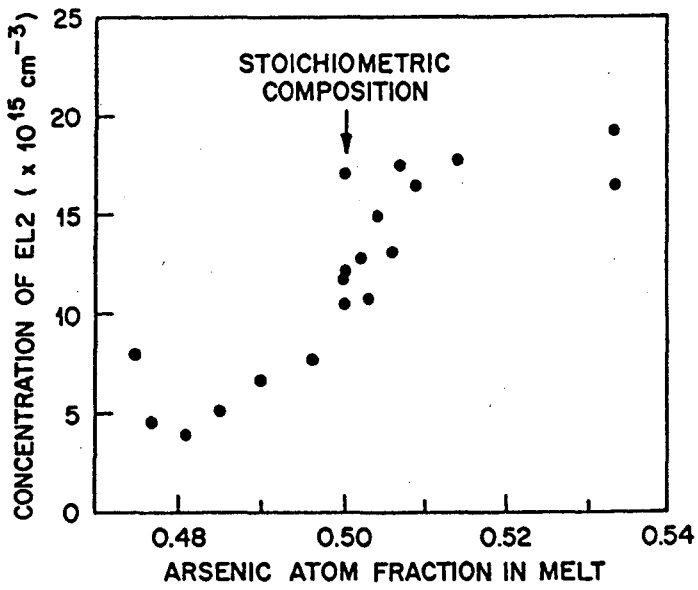

Fig. 2.7 Concentration of EL2 determined by optical absorption as a function of melt stoichiometry. (Holmes et al. 1982)

InP doped with Fe is a technological important semi-insulating substrate material for the fabrication of devices which are based on the epitaxial growth of ternary and quaternary III-V alloys. Fe is a deep acceptor in InP located 0.79 eV above the valence band edge and it compensates the residual shallow donors to yield high resistivity material (Juhl et al. 1987). Semi-insulating InP with resistivities of the order of 10^7 Ohm-cm can be achieved (Avella et al. 1997).

The redistribution of Fe in InP has been widely studied (Brozel et al. 1982, Holmes et al. 1981, Oberstar et al. 1981, Eaves et al. 1982, Makram-Ebeid et al. 1982). Fig. 2.8 shows an accumulation of Fe impurities at the surface followed by a depletion region for a Fe doped InP substrate annealed at 800°C for 30 minutes (Oberstar et al. 1981).

There is a lack of data available for values of diffusion coefficients and activation energies for transition metal impurities in GaAs and InP. Table 2.1 lists values for these parameters which have been reported in the literature.

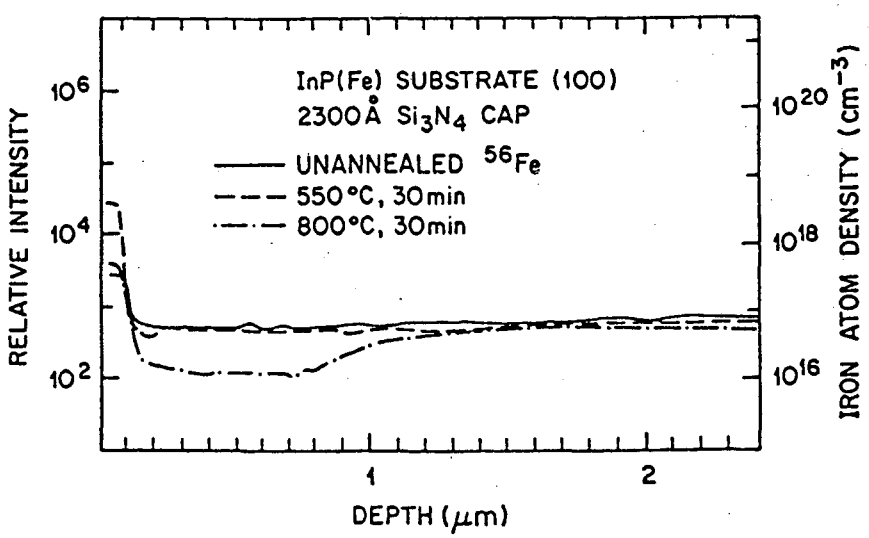

Fig. 2.8 Depth profiles of Fe in a semi-insulating InP substrate after 30 min. annealing at 550°C and 800°C. (Oberstar et al. 1981)

Table 2.1 Diffusion coefficients and activation energies for transition metal impurities in III-V semiconductors.

Impurity	**D_o ($cm^2 s^{-1}$)**	**E_a (eV)**	**Temperature Range (°C)**	Reference
Fe in GaAs	4.2×10^{-2}	1.8	850-1150	Boltaks et al.
	2.2×10^{-3}	2.32	750-1050	1975
	1.5×10^{-2}	2.0	950-1100	Uskov et al.
				1974
				Prikhodko et al.
				1978
Cr in GaAs	4.3×10^{3}	3.4	-----	Linh et al. 1981
Fe in InP	3	2.0	610-950	Shishiyanu et al.
	6.8×10^{5}	3.4	580-720	1977
	2.5×10^{-4}	1.7	700-900	Holmes et al.
				1981
				Kamda et al.
				1984

2.6 *High resistivity ion implanted GaAs, InP, $In_{0.53}Ga_{0.47}As$ epilayers*

Proton bombardment of p-type and n-type GaAs have been used to produce semi-insulating layers. Both single and multiple energies in the range of 100 keV to 3 MeV have been used for device isolation purposes. A typical implant dose is ~$10^{13}cm^{-2}$ (Donnelly 1977a and 1977b). Free carrier concentrations in these ion implanted layers are lower than $10^{11}cm^{-3}$. One disadvantage of device isolation by proton bombardment is that significant annealing can occur above 350°C. O^+ implantation has been used to avoid this problem and is stable for temperatures up to 800°C (Favennec et al. 1973). However, the implantation depths are much shallower than those obtained with proton bombardment due to the heavier ion mass. Low dose (10^{11}-10^{12} cm^{-2}) B^+ implants have also been used for device isolation (Clauwert et al. 1987). The isolation in these layers has been reported to be stable up to temperatures as high as 500°C.

In the case of InP, proton bombardment is not as effective in forming high resistivity layers as in GaAs (Donnelly et al. 1977b). The defects created tend to shift the Fermi level position to the upper part of the bandgap (Fig. 2.4). As a result, the maximum resistivity of n-type InP is of the order of 10^3-10^4 Ω–cm. In p-type InP, much higher resistivities can be achieved (10^8 Ω–cm). For p-type material, the implantation dose is critical. For doses higher than the critical dose the epilayer exhibits a p-to-n conversion with the same limiting resistivity for n-type material.

Implant isolation of $In_{0.53}Ga_{0.47}As$ by ion bombardment of H^+ has been investigated for as-grown layers with resistivities of the as-deposited films of 0.005 Ω-cm (Pearton et al. 1989). Layers which were bombarded by protons and annealed between temperatures of 100 to 500°C, exhibited a reduction in the measured resistivity

to below that of the as-grown value. B^+ implantation of $In_{0.53}Ga_{0.47}As$ has shown a maximum resistivity of 12 Ω-cm, an increase of two orders of magnitude compared to that of the as-grown material (Yamamura et al. 1993). However, these values are still too small for effective device isolation. In the case of O^+ implanted $In_{0.53}Ga_{0.47}As$ layers, a maximum resistivity of 10 Ω-cm was achieved after annealing at 350°C for 30s (Akano et al. 1996). For annealing temperatures above 350°C the resistivity decreased towards that of the unimplanted value.

There have been a few reports on Fe^+ implantation of $In_{0.53}Ga_{0.47}As$ (Pearton et al. 1989, Gulwaldi et al. 1991, Gruska et al. 1993). For $In_{0.53}Ga_{0.47}As$ layers (Fe doped) grown by liquid phase epitaxy, the position of the Fe^{2+}-Fe^{3+} acceptor level was determined to lie 0.39± 0.02eV above the valence band edge (Srocka et al. 1994). Since, the bandgap of $In_{0.53}Ga_{0.47}As$ is 0.75 eV at 300K, this deep acceptor level lies near midgap and fulfills one of the requirements for choosing the proper transition metal impurity to obtain high resistivity layers. An estimated near intrinsic resistivity (~10^3 Ohm-cm) was reported for Fe^+ implanted layers (Gulwaldi et al. 1991). In this work, the entire $In_{0.53}Ga_{0.47}As$ layer did not have a uniform ion concentration, since only a single ion energy implantation was performed. As a result, there were regions of unimplanted $In_{0.53}Ga_{0.47}As$ which had to be considered in the resistivity measurements. The as-grown samples were grown by LPE and contained a background concentration of the order of 10^{14} cm^3. Typical undoped InGaAs layers, depending on the growth techniques and conditions, can have higher donor concentrations of ~ 10^{15}-10^{17} cm^{-3} due to background impurities. The electrical behavior as a function of a wide range of annealing temperatures has not been reported. The degree to which Fe acts as a compensating

dopant in $In_{0.53}Ga_{0.47}As$ layers has not been assessed since no Hall effect measurements have been performed. A comprehensive investigation of the electrical properties and thermal stability of fully isolated $In_{0.53}Ga_{0.47}As$ layers with uniform Fe^+ implant concentration is still lacking. A correlation of the electrical and diffusive properties of Fe^+ implanted and annealed layers would be of particular interest for forming layers of high resistivity.

3 Experimental Procedures

3.1 Sample Processing

3.1.1 Growth of $In_{0.53}Ga_{0.47}As$ epilayers on InP

The $In_{0.53}Ga_{0.47}As$ layers used in the ion implantation studies were grown on <100> semi-insulating InP substrates. The resistivity of the substrate was ~ $2.5x10^7$ Ω–cm. These thin films were grown by Metal Organic Vapor Phase Epitaxy (MOVPE) and were unintentionally doped n-type. The thickness of the as-grown layers ranged from 0.4-0.8 μm. The concentration of Fe in the semi-insulating substrate was of the order of $10^{16}cm^{-3}$.

For the diffusion experiments, the $In_{0.53}Ga_{0.47}As$ layers were grown by Molecular Beam Epitaxy (MBE). These layers were also grown on SI InP (Fe doped) substrates and were unintentionally doped n-type. The Fe from the substrate was used as the source of Fe atoms. The thicknesses of the as-grown layers were 2.2 μm. A control experiment was performed to better understand the data from the diffusion experiments. For this set of experiments the $In_{0.53}Ga_{0.47}As$ layers were grown on a S doped substrate with thicknesses of 1 μm.

3.1.2 Ion implantation

Ion implantation of inert gas ions (e.g. Ne) was performed in a Varion Extrion #5 machine with an endstation which can be cooled with LN_2. Energies ranging from 20 to 200 keV could be implanted for singly ionized species. During implantation, all samples were tilted 7 ° away from the normal to avoid channeling. Samples were mounted onto Al plates which are screwed onto the endstation paddle.

Implantation of the transition metal impurities was done at the Research School of Physical Sciences & Engineering at the Australian National University in Canberra, Australia, using a 1.7 MV NEC Tandem high energy ion implanter. Ion energies in the range of 15 keV to 10 MeV (for multiply charged ion species) could be achieved.

Implantation conditions for all of the samples can be found in Appendix B.

3.1.3 Thermal annealing

Following implantation, the implanted impurities were located in random positions and there was considerable lattice damage created by the stopping process. Thermal annealing was required to repair the lattice damage and electrically activate the impurities by promoting short range diffusion of these impurities onto lattice sites.

In III-V semiconductors annealing at temperatures above 650°C for GaAs and 350°C for InP results in degradation of the surface of the semiconductor by the loss of the group V element. Some form of protection must be provided during thermal annealing. Proximity annealing in which the sample is placed face-to-face with another GaAs wafer was used for the implantation work and ampoule annealing was employed for the diffusion experiments.

Samples were annealed by rapid thermal annealing (RTA) in a Heatpulse 210T RTA system. A rapid thermal annealing furnace is illustrated in Fig. 3.1. The annealing chamber consisted of upper and lower banks of high-intensity, tungsten-halogen lamps and water-cooled, reflective walls. These banks contain a total of thirteen 1.5 kW lamps. The maximum input power was limited to 18 kW. This power was converted into radiant energy which was trapped within the reflectors and was efficiently absorbed by the sample holder Si wafer. The temperature within the RTA was measured by a type K thermocouple embedded in the 4 inch wafer. The RTA was used in the temperature control mode in which the annealing temperature and time is specified and the system automatically adjusts the light intensity to provide maximum heating and cooling rates with accurate steady-state temperature and time. The samples were placed on the 4 inch Si wafer with the $In_{0.53}Ga_{0.47}As$ epilayer side up inside the quartz chamber. Another piece of GaAs was placed on top of the sample to create an As overpressure. The samples were annealed in a N_2 ambient.

For the diffusion experiments, the $In_{0.53}Ga_{0.47}As$ samples were sealed in an evacuated quartz ampoules together with crushed bulk GaAs. Elemental arsenic was also added to the ampoule to adjust the partial pressure of As_4 to about 1 atm at the diffusion temperature. The ampoule was cleaned with a 5% HF solution, rinsed with deionized water, methanol and then blown dry with N_2 prior to sealing. Sealing was done with a hydrogen torch. Annealing was performed at 550°C for 1 hour in a horizontal tube furnace. The sealed ampoules were annealed in flowing N_2.

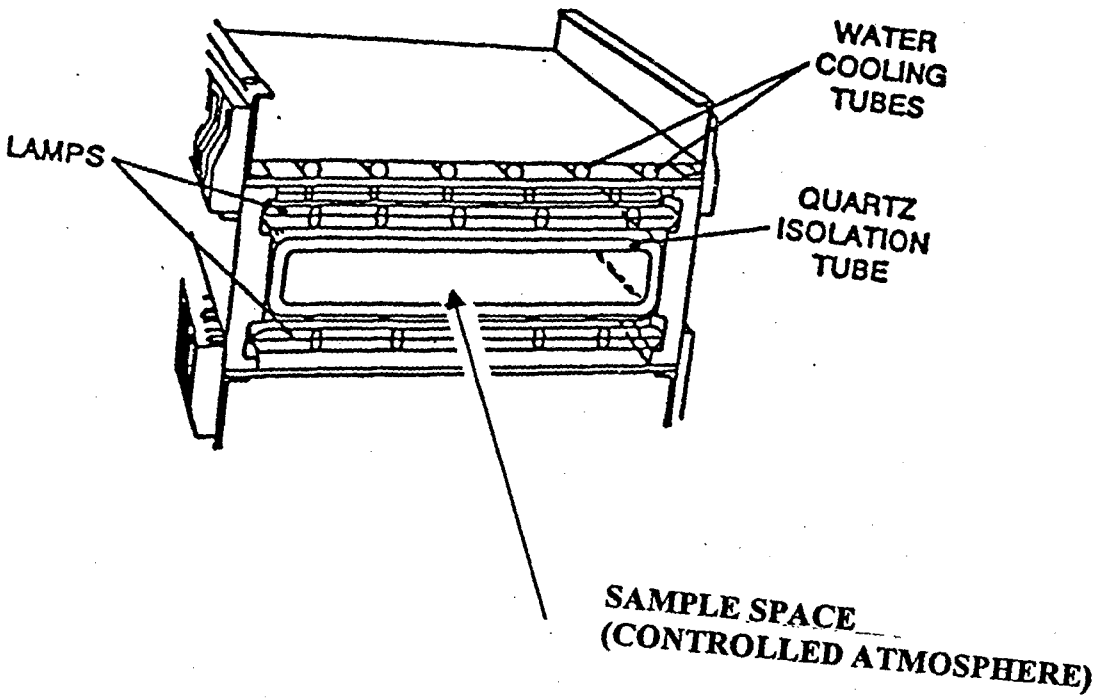

Fig. 3.1 Schematic of a typical rapid thermal annealing furnace.

3.2 Characterization Methods

3.2.1 Hall Effect and Resistivity

Hall Effect was used to measure the total concentration of free carriers in the $In_{0.53}Ga_{0.47}As$ epilayer. In order to perform electrical measurements contacts have to be made on the semiconductor samples. For the n-type $In_{0.53}Ga_{0.47}As$ layers, InSn alloyed contacts were formed by annealing at 300°C for 10 minutes in flowing N_2. Copper wires were etched in HCl and then coated with InSn on the tips and pressed onto the contacts.

In the Hall Effect apparatus there were sixteen modes of measurement. Modes 1-8 were used to measure the resistivity of the semiconductor and the carrier concentration was determined from modes 9-16. From these two measurements, the mobility could be calculated. For all measurements, a magnetic field of 3kG was used. Experimental details of the Hall Effect measurements are given in Appendix C.1 (i.e., Van der Pauw technique, block schematic of Hall system, etc.).

3.2.2 Rutherford Backscattering Spectrometry (RBS) and channeling RBS (c-RBS)

The thickness of the un-implanted $In_{0.53}Ga_{0.47}As$ layers was measured using RBS. In addition, channeling RBS was employed to characterize the radiation damage caused by the implantation. RBS was performed at the Ion Beam Analytical Facility at the Lawrence Berkeley National Laboratory. The ion beam was generated by a 2.5 MeV Van de Graaff electrostatic accelerator. In these experiments a 1.95 MeV He^+ beam was used. The diameter of the beam was 2 mm. Two silicon surface barrier detectors are installed in the chamber which have an energy resolution of 18 keV. One was located at 165° and the other at 100-120°. The detector solid angle was 2 msr. The samples were mounted on a two axis goniometer in the experimental chamber which was used to align

the crystal with respect to the beam. An electron suppression shield biased at -900V was used to suppress any secondary electrons. For each spectrum about 4μC of charge was collected at a beam current of about 10nA. To minimize ion damage, after obtaining the channel by tilting and rotating the sample, the sample was translated to a fresh spot for data collection.

3.2.3 Secondary ions mass spectrometry (SIMS)

The distribution of the compensating dopants in the as-implanted and annealed layers was examined by SIMS. The SIMS analysis was performed at Charles Evans and Associates using a CAMECA IMS-3f double focussing magnetic sector ion microanalyzer. Dynamic SIMS was used in which the intensity of one peak for a particular mass was recorded as a function of time. Oxygen bombardment (8 keV) was used with SIMS monitoring of positive secondary ions. The sputtering rate was ~10 μm/hr. For Fe, the detection limit was 10^{15} cm^{-3}. Data were collected in the form of secondary ion counts vs. time. The secondary ion counts were converted to atomic concentration using relative sensitivity factors determined from ion implanted standards. For ion implanted standards the implant dose can be controlled accurately to within 5%. Sputtered time was converted to depth using stylus profilometer measurements of the sputter crater depths and the total sputter time. The depth scale calibration is accurate to within ± 10% and depends on target and projectile mass.

3.2.4 Electrochemical capacitance voltage (ECV)

For depth profiling of the doping concentration an ECV profiler was used. ECV profiles were obtained using the BioRad Polaron instrument. Ohmic contacts were placed on the samples using InGa. The electrolytic solution used was "Pear etch"

($HCl:HNO_3$: CH_3OH 36:24:1000). For etching conditions, the voltage applied was selected so that an etching current of 0.2 mA cm^{-2} and etching rate of 1 μm/hr were obtained. C-V measurements were performed at steps of 0.01 μm. The measuring voltage was chosen where $1/C^2$ was a straight line.

3.2.5 X-ray diffraction (XRD)

To determine the lattice mismatch and strain between the $In_{0.53}Ga_{0.47}As$ epilayer and the InP substrate, x-ray rocking curves were obtained. A Siemens D5000 diffractometer was used for θ-2θ scans (or normal coupled scan) and rocking curve measurements. The incident radiation was Cu K_α E=8.04928 keV ($\lambda \sim 1.54051$ Å). The x-ray tube voltage was 40 kV and the current was set at 30 mA. For rocking curve measurements, a Ge (022) monochromator was used.

3.2.6 Transmission electron microscopy (TEM)

In an effort to examine if there were precipitates in the Fe doped layers, the as-implanted and annealed samples were studied by transmission electron microscopy. TEM was performed using a JEOL 200CX high resolution electron microscope. Cross-sectional samples were prepared by mechanical grinding, followed by ion milling using an Ar^+ beam on a liquid nitrogen cooled stage. Selected area diffraction was performed to identify the lattice structure.

4 Results and Discussion

4.1 Implant isolation by lattice damage: Ne implantation

Implantation schedules consisting of multiple energy implants were used to obtain uniform concentrations over the entire $In_{0.53}Ga_{0.47}As$ layer. The Ne^+ ion implant energies ranged from 50 to 200 keV. Doses were chosen to obtain an average volume concentration of $5x10^{15}cm^{-3}$, $5x10^{17}cm^{-3}$, $5x10^{19}cm^{-3}$. The implantation energies and doses can be found in Appendix B. All of the samples were implanted at room temperature. The channeled RBS spectra for the Ne^+ implanted samples are shown in Fig. 4.1. A 1.95 MeV He^+ beam aligned along the <110> was used. In order to determine the optimal implantation conditions which would improve the resistivity in the epilayers, three separate samples were implanted with Ne concentrations ranging from $5x10^{15}cm^{-3}$ to $5x10^{19}cm^{-3}$. None of the implanted samples became completely amorphous as can be seen from the spectra none of which coincided with the random spectrum.

A maximum resistivity of 5 Ω-cm was measured for the layer implanted with $5x10^{17}$ atoms cm^{-3} and annealed at 300°C for 30s (Fig. 4.2). Similar defect annealing characteristics are observed for all of the implanted $In_{0.53}Ga_{0.47}As$ layers. When annealing at temperatures above 300°C the resistivity decreased for all of the ion implanted and annealed samples.

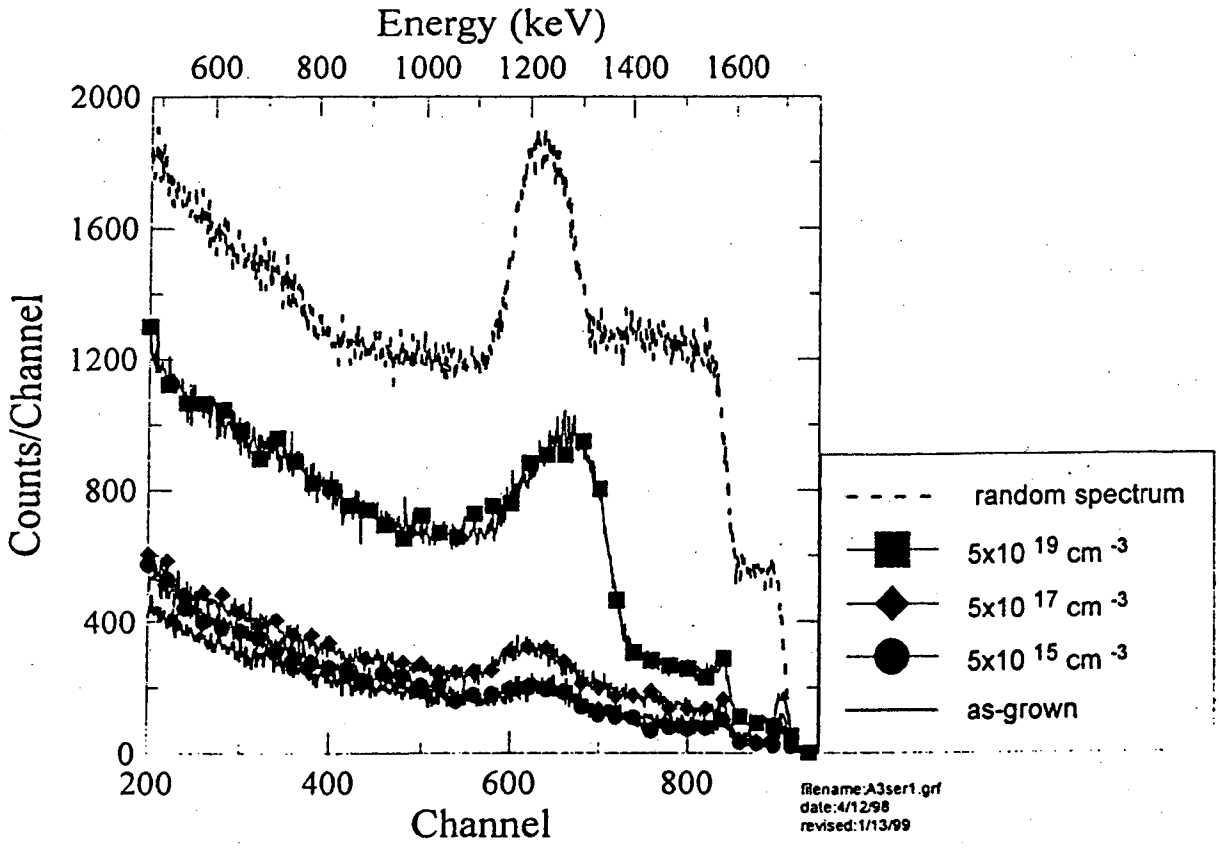

Fig. 4.1 1.95 MeV He^+ <110> aligned backscatter spectra of $In_{0.53}Ga_{0.47}As$ layers implanted with Ne concentrations ranging from $5x10^{15}$-$5x10^{19}cm^{-3}$.

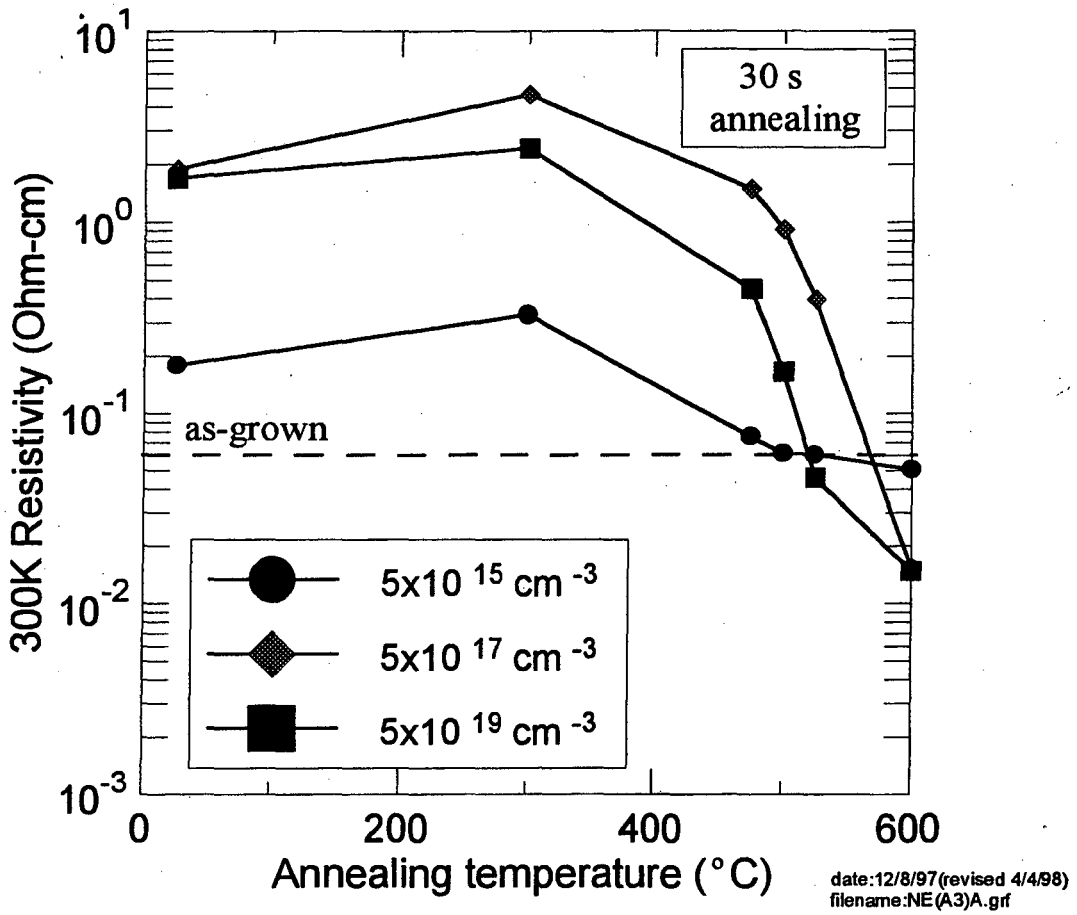

Fig. 4.2 Room temperature resistivity measurements for the Ne^+ implanted $In_{0.53}Ga_{0.47}As$ layers as a function of annealing temperature. All samples were annealed for 30s. The resistivity of the as-grown layer is also shown.

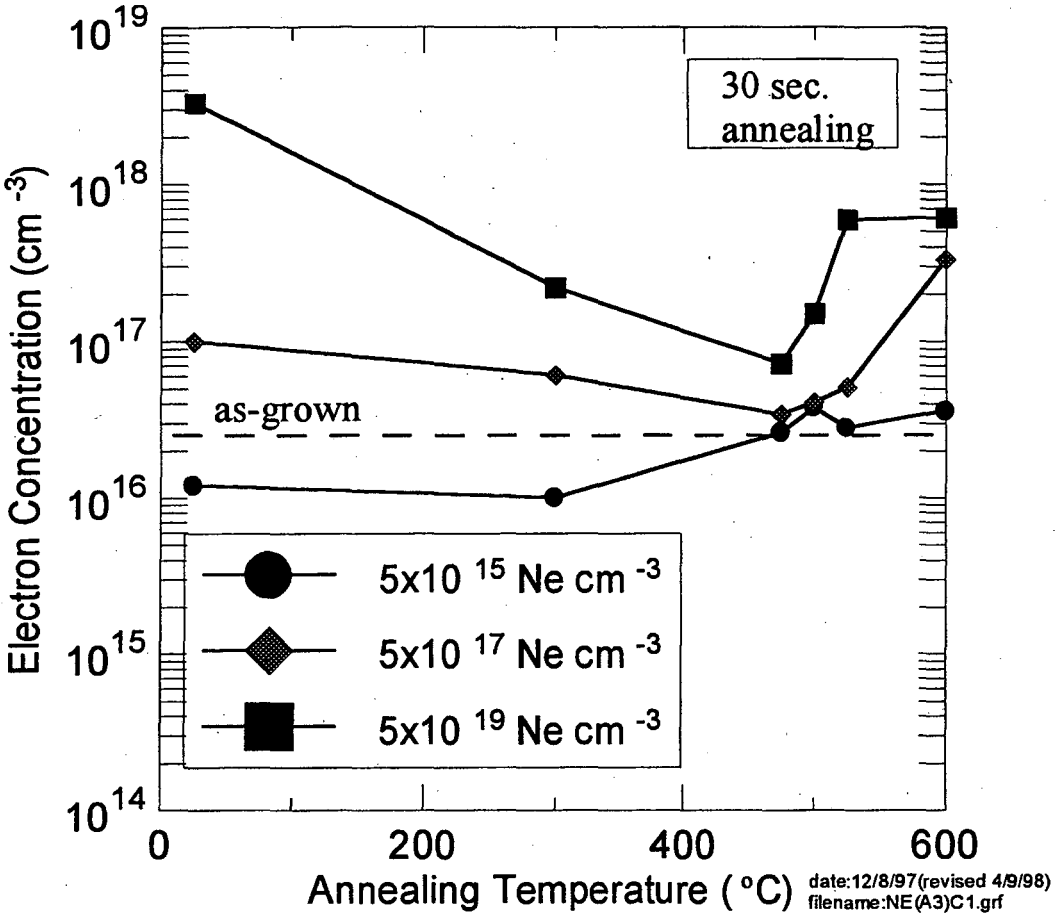

Fig. 4.3 Room temperature Hall Effect measurements for the Ne^+ implanted $In_{0.53}Ga_{0.47}As$ layers as a function of annealing temperature. All samples were annealed for 30s. The electron concentration of the as-grown layer is also shown.

Free carrier concentrations in the epilayers were determined by Hall Effect measurements at room temperature (Fig. 4.3). In general, an increase in the free electron concentration beyond than the original value was observed. In the as-implanted samples the concentration of these carriers increases with implant ion concentration. The damage induced carriers observed in the Ne^+ implanted and annealed layers suggests the formation of defect related damage levels which lie near the conduction band edge. This is consistent with a Fermi stabilization energy close to the conduction band edge (Walukiewicz 1993).

The mobility is calculated (Fig. 4.4) from the resistivity and Hall Effect values. Although the mobility is reduced significantly by approximately three orders of magnitude for the sample with the highest implantation damage (i.e. $5x10^{19}$ Ne^+ cm^{-3}), we found that the resistivity did not increase accordingly. Clearly, this is due to the increase in the electron concentration (higher than the original value) which was measured for the as-implanted $In_{0.53}Ga_{0.47}As$ layers. It is evident that the mobility has not totally recovered after annealing at a temperature of 600°C. This may be due to ionized impurity scattering since a high electron concentration was measured. In addition, residual defects may still be present after annealing.

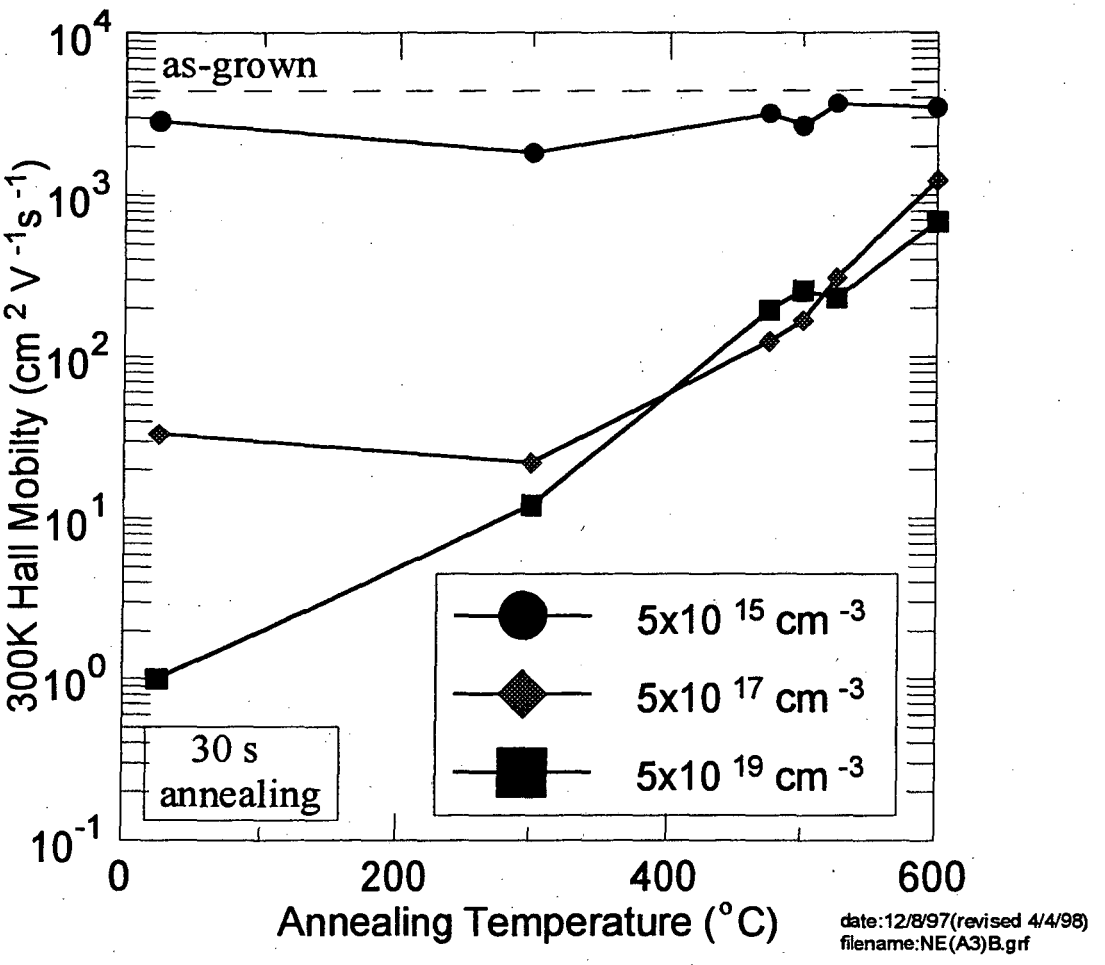

Fig. 4.4 Room temperature mobility measurements as calculated from the electron concentration and the resistivity values. All samples were annealed for 30s. The mobility of the as-grown layer is also shown.

For the sample implanted with the highest Ne concentration, the electron concentration ($n \sim 3 \times 10^{18} cm^{-3}$) exceeded the effective density of states ($N_c \sim 2.08 \times 10^{17} cm^{-3}$) in the conduction band for $In_{0.53}Ga_{0.47}As$ which would suggest that the material was metallic. The mobility measurements show evidence of defect band conduction rather than conduction within the conduction band due to the extremely small values of mobility which were measured. The decrease in electron concentration as a function of annealing temperatures up to about 475°C can be best be understood by a defect band which becomes narrower with annealing temperature.

Of particular interest is the increase in electron concentration observed at annealing temperatures above 500°C. A similar effect has been observed in B^+ implanted $In_{0.53}Ga_{0.47}As$ layers which were annealed at 600°C (Yamamura et al. 1993). These results suggest the formation of shallow donors by implantation and the subsequent annealing. These donors may be attributed to defect complexes which are not annihilated, but are converted into a new stable state after annealing at 600°C. It may be speculated that the two types of defects which would exhibit donor-like behavior are In, Ga, or As interstitials and Arsenic vacancies. Assuming (1) a preferential loss of As at the surface during thermal annealing and (2) that the donor-like defects can be attributed to V_{As}, then the profile of the free electron concentration within the epilayer should be non-uniform, rising rapidly towards the sample surface. An electro-chemical capacitance measurement was performed to determine the electron concentration within the epilayer implanted with $5 \times 10^{17} cm^{-3}$ Ne^+ and annealed at 600°C for 30s. The electron concentration appeared to be uniform in the $In_{0.53}Ga_{0.47}As$ epilayer (Fig. 4.5) which

suggests that no significant indiffusion or outdiffusion of donor-like defects has taken place which one would expect if there was As loss at the surface.

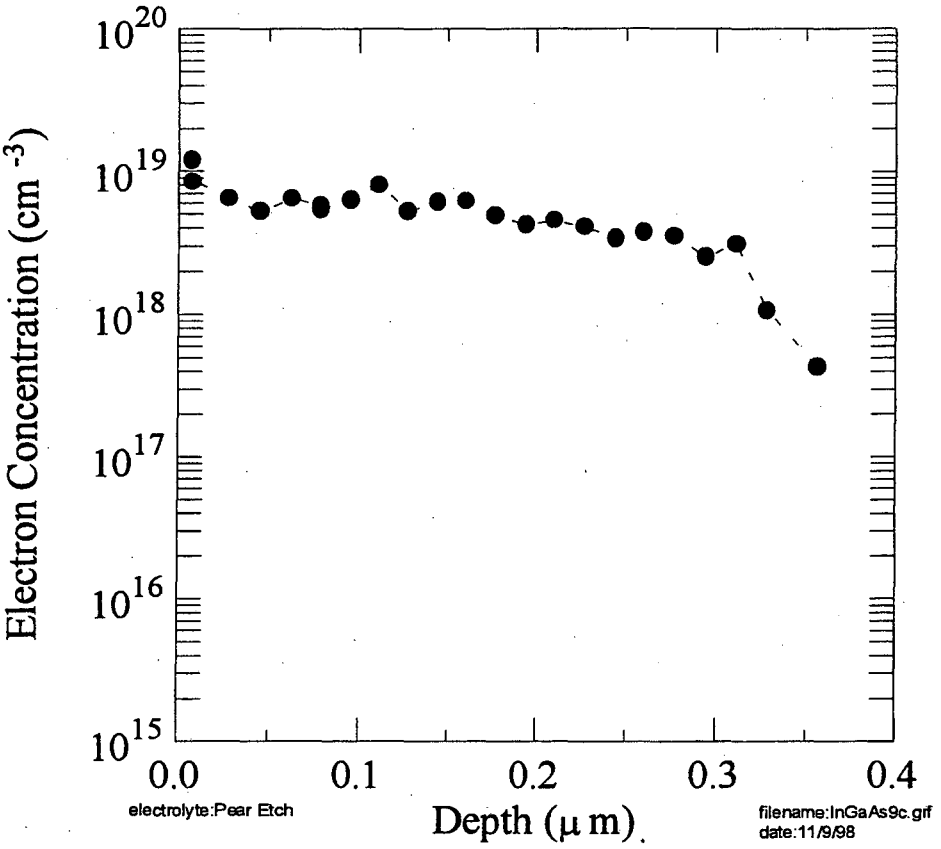

Fig. 4.5 Carrier concentration as a function of depth measured by electrochemical capacitance-voltage profiling for the $In_{0.53}Ga_{0.47}As$ layer implanted with $5x10^{17}$ Ne atoms cm^{-3} and annealed at 600°C for 30s.

4.2 Implant isolation by compensation of dopants

4.2.1 Fe implantation

Implantation of Fe was studied because it forms a deep acceptor level ($E_{V.B.}$ +0.39 eV) in $In_{0.53}Ga_{0.47}As$ (Srocka et al. 1994). The epitaxial layers were implanted with concentrations ranging from $2x10^{17}cm^{-3}$ to $2x10^{18}cm^{-3}$ (Appendix B). The highest increase in resistivity was obtained for the sample implanted with a concentration of $2x10^{18}cm^{-3}$. Room temperature resistivity and free electron concentration for the as-implanted and the annealed samples are shown in Fig. 4.6. Similar electrical properties were observed for the sample implanted at LN_2 temperature. The optimal annealing temperature for maximum resistivities found for both of the samples implanted at LN_2 and RT was 800°C. The highest resistivities for the samples implanted at LN_2 and RT were approximately 320 Ω-cm and 770 Ω-cm, respectively. At annealing temperatures greater than 800°C the resistivity decreased and the free electron carrier concentration increased (Fig. 4.6). The value of the mobility approaches that of the as-grown material, but has not totally recovered at the highest annealing temperature which suggests residual damage (Fig. 4.7).

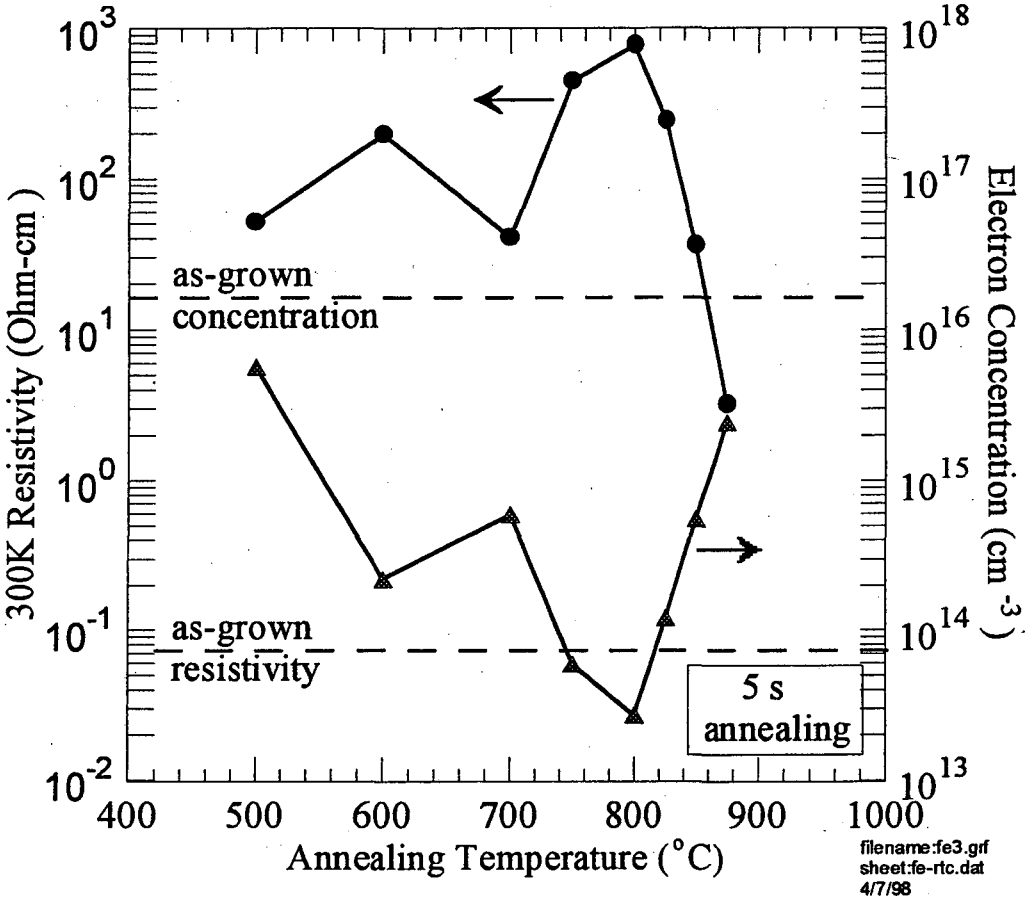

Fig. 4.6 Room temperature Hall Effect and resistivity measurements for the Fe^+ (RT) implanted $In_{0.53}Ga_{0.47}As$ layers as a function of annealing temperature. The samples were annealed for 5s. The electron concentration and resistivity values of the as-grown layer are also shown.

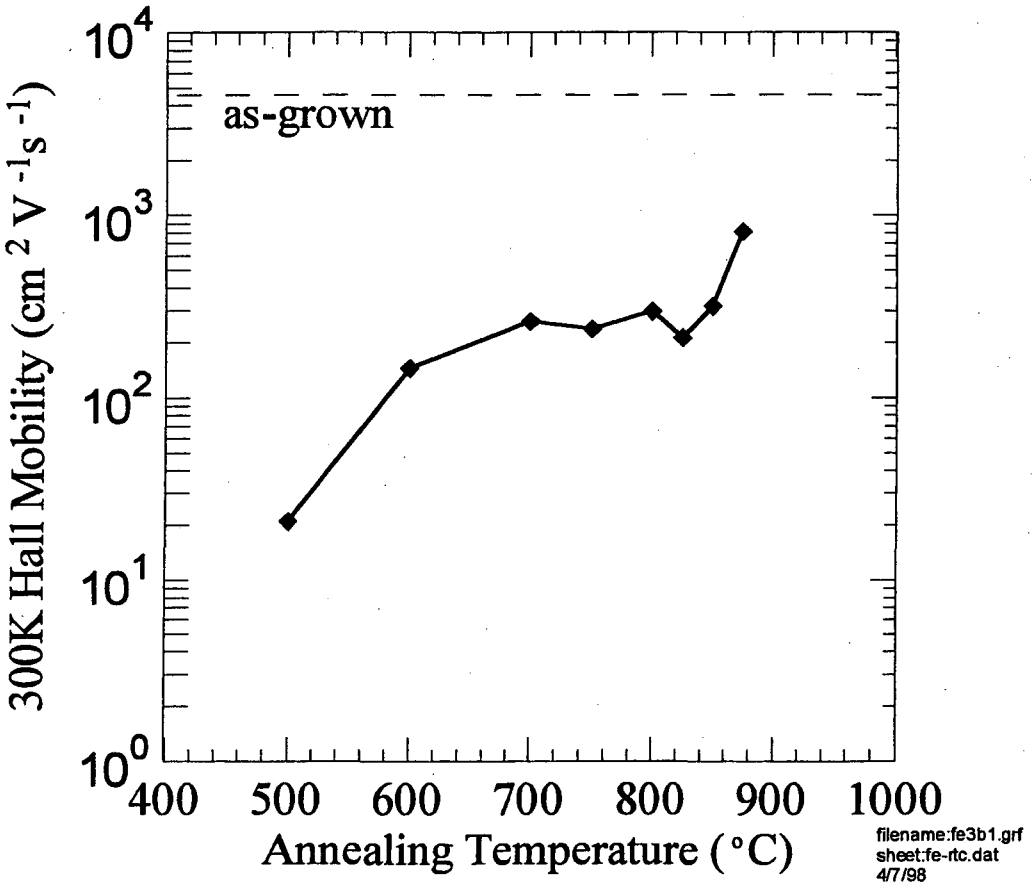

Fig. 4.7 Room temperature mobility measurements for the Fe^+ (RT) implanted $In_{0.53}Ga_{0.47}As$ layers as a function of annealing temperature. The samples were annealed for 5s. The mobility of the as-grown layer is also shown.

An interesting kink is produced in the resistivity and Hall effect dependencies on temperature when annealing at 700°C. Several samples were measured in the temperature range 550-750°C and this kink near 700°C appears to be reproducible. One explanation for the presence of this kink may be gettering of Fe at dislocation loops. In GaAs, dislocations loops begin to anneal at temperatures above 700°C (Sealy 1988, Kular et al. 1980). If dislocation loops start to anneal above this temperature, a higher concentration of Fe is available for compensation. Therefore, the release of Fe from dislocations results in higher compensation of donors as is observed from the electrical measurements. In order to verify this hypothesis electron microscopy is required to ascertain the concentration of dislocation loops as a function of annealing temperature within the annealing range in question.

The concentration of deep Fe acceptors ($2x10^{18}$ cm^{-3}) was greater than that of the donor concentration ($10^{16}cm^{-3}$) in the as-grown material. Since the concentration of free carriers is still higher than the intrinsic value ($n \sim 6.7x10^{11}cm^{-3}$) for the layers implanted at RT and annealed at 800°C ($n \sim 2.7x10^{13}cm^{-3}$), we must assume that damage related donors form or that Fe precipitates and becomes electrically inactive. The Fermi energy for the sample exhibiting the highest compensation of carriers is calculated to be approximately 0.23 eV below the conduction band which correlates with the E_{FS} for irradiated $In_{0.53}Ga_{0.47}As$. Indeed this in turn supports the formation of defect related donors. Channeling RBS spectra for the as-implanted and annealed layers indicate that there is significant residual damage after 800°C annealing (Fig. 4.8). These structural results strongly support our explanation for the electrical data. It is evident that the damage is not completely annealed before the electrical activation occurs. Ideally, for

obtaining a maximum shallow donor compensation it would be desirable to anneal out all of the damage related donors before the Fe deep levels are electrically activated.

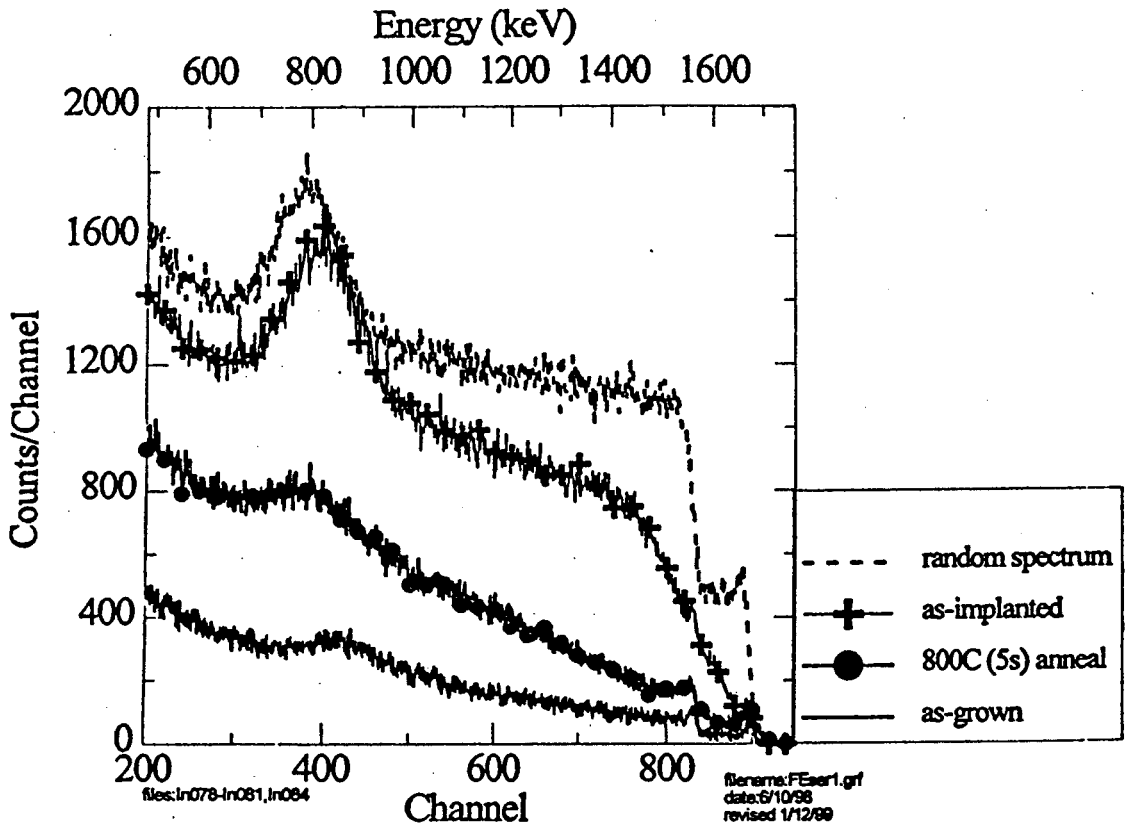

Fig. 4.8 1.95 MeV He^+ <110> aligned backscatter spectra of $In_{0.53}Ga_{0.47}As$ layers implanted with Fe at RT and after annealing at 800°C for 5s.

Transmission electron microscopy was performed on the Fe^+ implanted and annealed layers to determine if Fe had precipitated in the $In_{0.53}Ga_{0.47}As$ layers. FeP precipitates have been reported in Fe-doped InP grown by MOCVD (Chu et al. 1994). Precipitates were found for Fe concentrations of $10^{17}cm^{-3}$. In addition, the formation of FeAs precipitates has been observed in GaAs/AlGaAs heterostructures grown by Liquid Phase Epitaxy (LPE) (Katcki et al. 1996). Cross-sectional TEM of the Fe implanted $In_{0.53}Ga_{0.47}As$ layers revealed end-of-range implantation damage (observed as dark spots in the micrograph) in the InP substrate (Fig. 4.9). Dislocation loops were observed in the sample which was annealed at 800°C for 5s (Fig.4.10). In order to examine the possibility of Fe precipitation at the dislocation loops, Selected Area Diffraction (SAD) was performed on the annealed layers. The SAD patterns did not exhibit any extra spots which one would expect for a precipitate having a crystal structure different from that of the host semiconductor material. Therefore, we concluded from these TEM results that there was no appreciable precipitation of the Fe in the $In_{0.53}Ga_{0.47}As$ layers for the concentrations of Fe used in these series of experiments ($2x10^{18}cm^{-3}$). However, the possibility of the Fe atoms preferentially occupying sites at dislocation cores (without forming precipitates) can not be excluded.

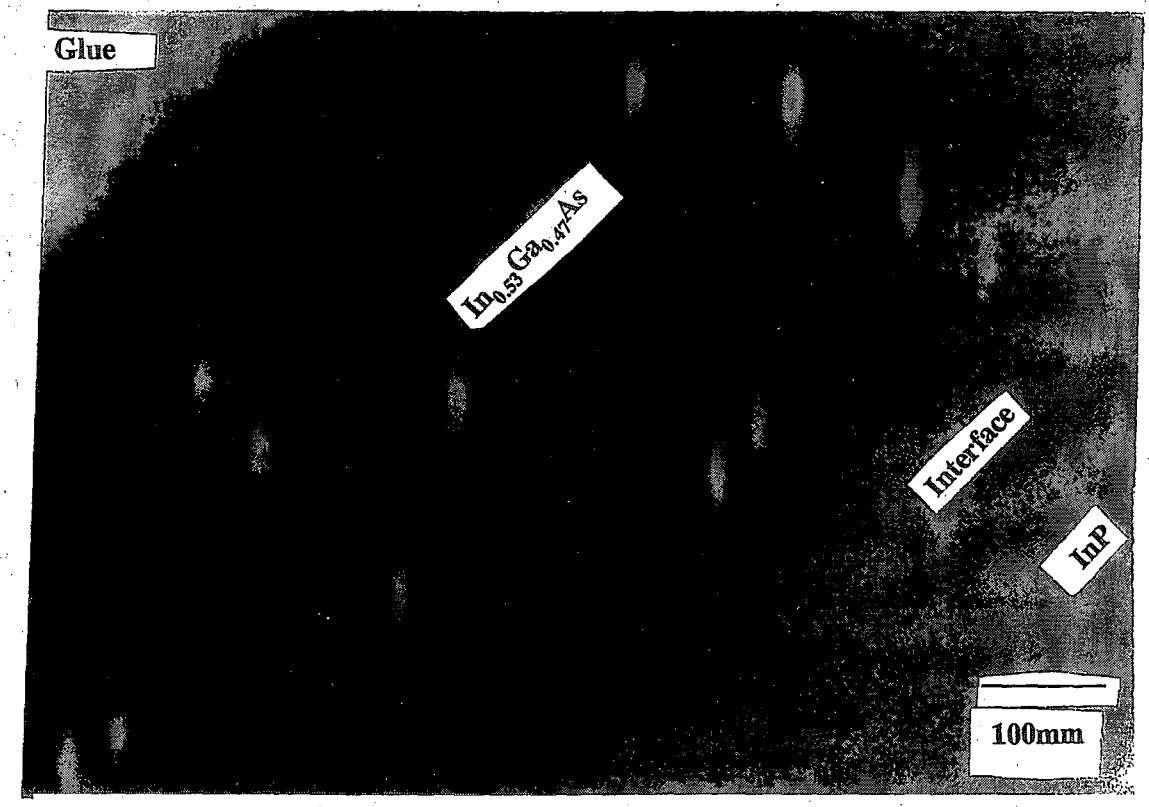

Fig. 4.9 Cross-section Transmission Electron Microscope micrograph of Fe^+ implanted $In_{0.53}Ga_{0.47}As$ layer.

Fig. 4.10 Cross-section Transmission Electron Microscope micrograph of Fe^+ implanted $In_{0.53}Ga_{0.47}As$ layer after annealing at 800°C for 5s.

Annealing at 875°C for 5s lead to an increase in the free electron concentration (Fig.4.6). SIMS analysis was performed to investigate the distribution of the compensating dopants in the annealed layers. The As SIMS signal was monitored in order to locate the interface between the epilayer and the substrate. The SIMS profile for the as-implanted Fe shows the tail end of the Fe implant distribution reaching into the InP substrate. From the SIMS analysis (Fig. 4.11) it became evident that the increase in electron concentration was a result of the rapid out-diffusion of compensating Fe from the $In_{0.53}Ga_{0.47}As$ epilayer.

It is clear from the SIMS profile that there is a driving force for the Fe to diffuse from the $In_{0.53}Ga_{0.47}As$ layer into the InP substrate. This behavior can be attributed to a "size effect" or higher diffusivity of the Fe in the epilayer than in the substrate. The latter argument is discussed in section 4.3. In terms of the "size effect", from Table 4.1 we observe that In has a larger ionic radii than Ga. Therefore, Fe atoms could theoretically be accommodated with less strain on the In sites than on the Ga ones. Since, the InP lattice has more In sites, it may be more energetically favorable for the Fe to diffuse into the InP.

Of particular interest is the pile up of impurities which occurred at the interface between the epilayer and the substrate. This topic will be covered in detail in section 4.4.

Table 4.1 Ionic radii for Fe, In, and Ga.

5 Ion	Radii (pm)
Fe^{+3}	67
Fe^{+2}	82
In^{+3}	92
In^{+}	132
Ga^{+3}	62
Ga^{+}	113

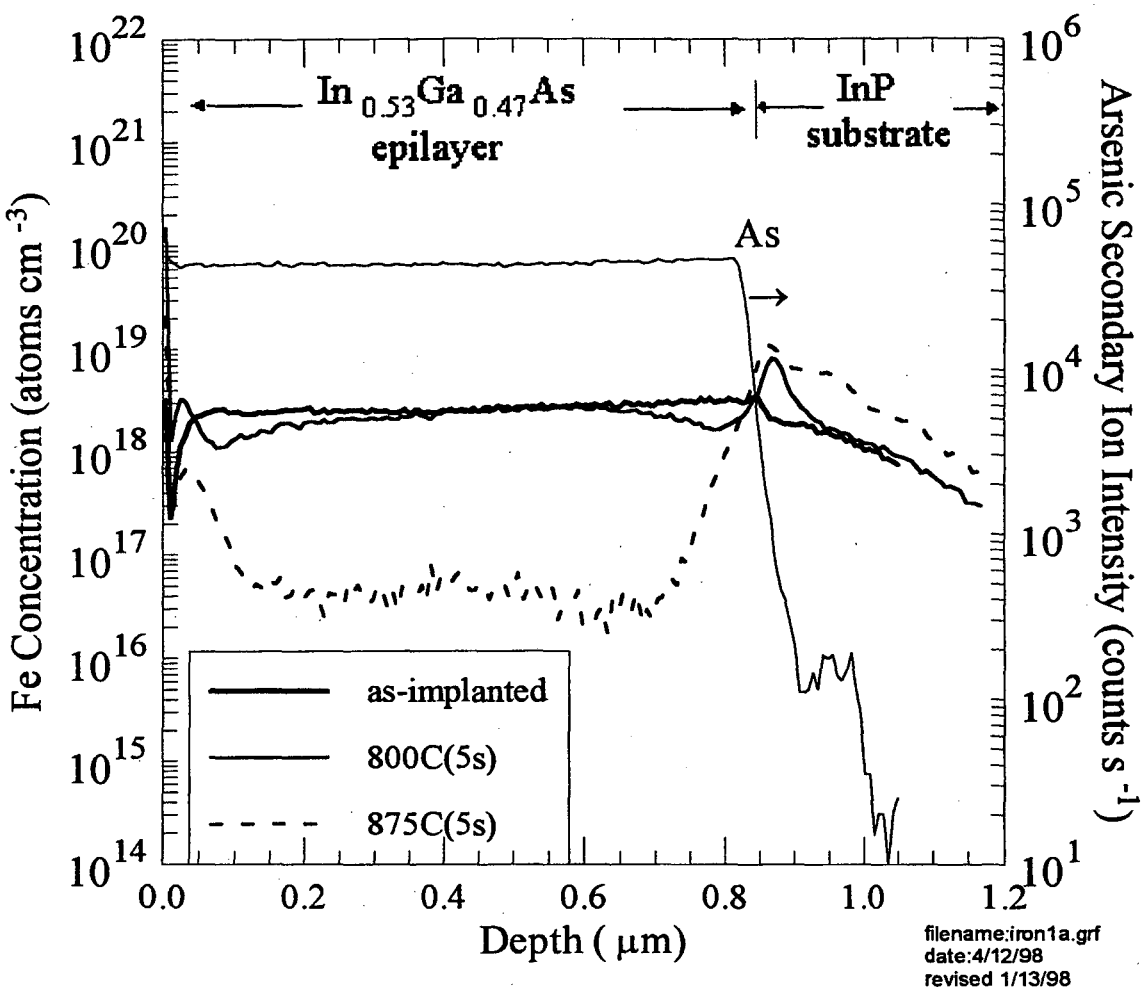

Fig. 4.11 SIMS depth profiles for $In_{0.53}Ga_{0.47}As$ layers implanted (bold solid line) with Fe at RT and annealed at 800°C for 5s (solid line) and 875°C for 5s (dashed line). The As SIMS signal (right axis) was used only as a marker to locate the interface between the epilayer and the substrate and was not quantified.

4.2.2 Fe and C dual implantation

An effective approach to obtaining semi-insulating layers is based on close compensation of shallow donors and acceptors and the introduction of deep level impurities to pin the Fermi level midgap. In this series of experiments, the effect of dual implantation with Fe and C in $In_{0.53}Ga_{0.47}As$ was studied. From the results in the previous section, it became evident that not all of the shallow donors are compensated. In an effort to increase the level of compensation, the samples were implanted with C which forms a shallow acceptor in $In_{0.53}Ga_{0.47}As$. The $In_{0.53}Ga_{0.47}As$ layers were implanted with 400 keV C to a dose of $4x10^{13}cm^{-2}$. From the room temperature resistivity measurements (Fig. 4.12), it is apparent that implantation of C did not result in an increase in the resistivity to a value greater than what is obtained with Fe implantation alone. Implantation resulted in a three order of magnitude increase in the electron concentration as measured by Hall Effect (Fig. 4.13). This is in fact consistent with the Ne^+ implantation study which showed that the electron concentration increased after implantation (Fig. 4.3). This effect can most likely be attributed again to the formation of defect related damage levels which lie near the conduction band. At temperatures greater than 800°C, the resistivity decreased probably due to outdiffusion of the Fe as was observed in Fig. 4.11.

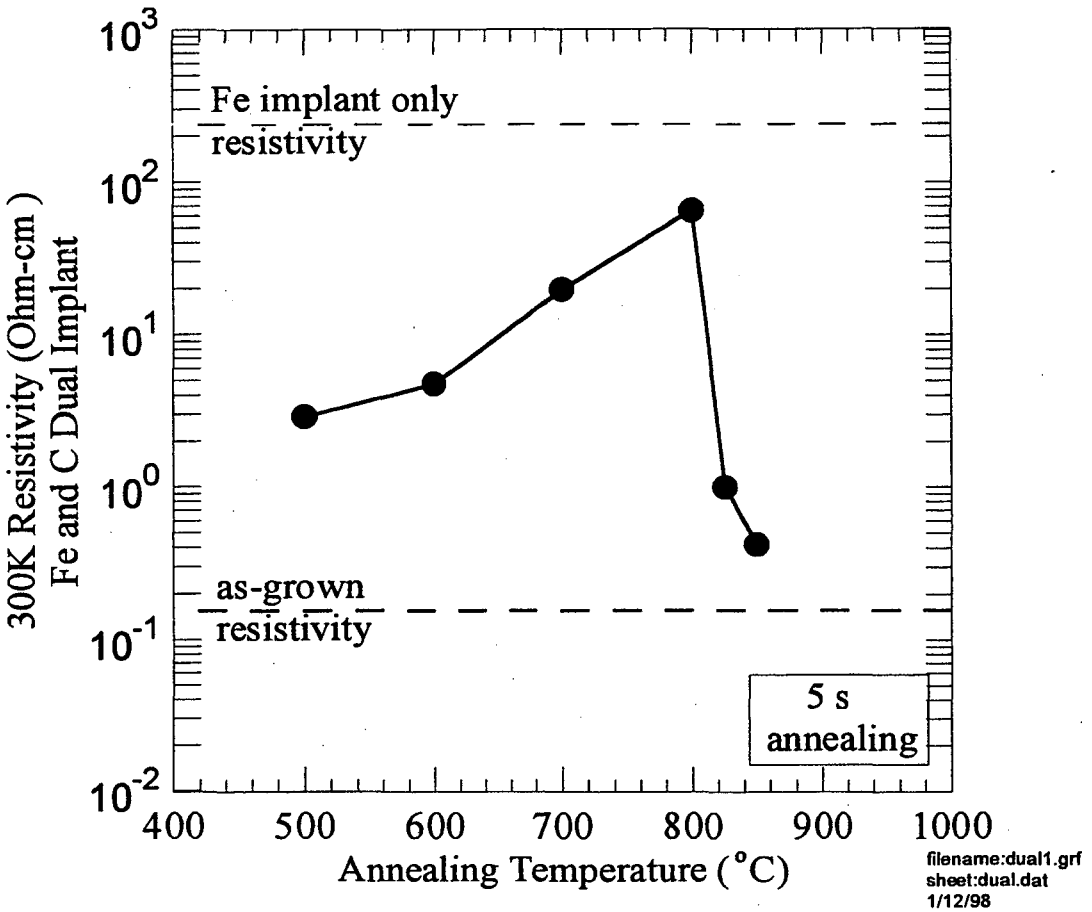

Fig. 4.12 Room temperature resistivity measurements for the Fe^+ and C^+ implanted $In_{0.53}Ga_{0.47}As$ layers as a function of annealing temperature. The samples were annealed for 5s. The resistivities of the as-grown and the Fe^+ implanted only layers are also shown.

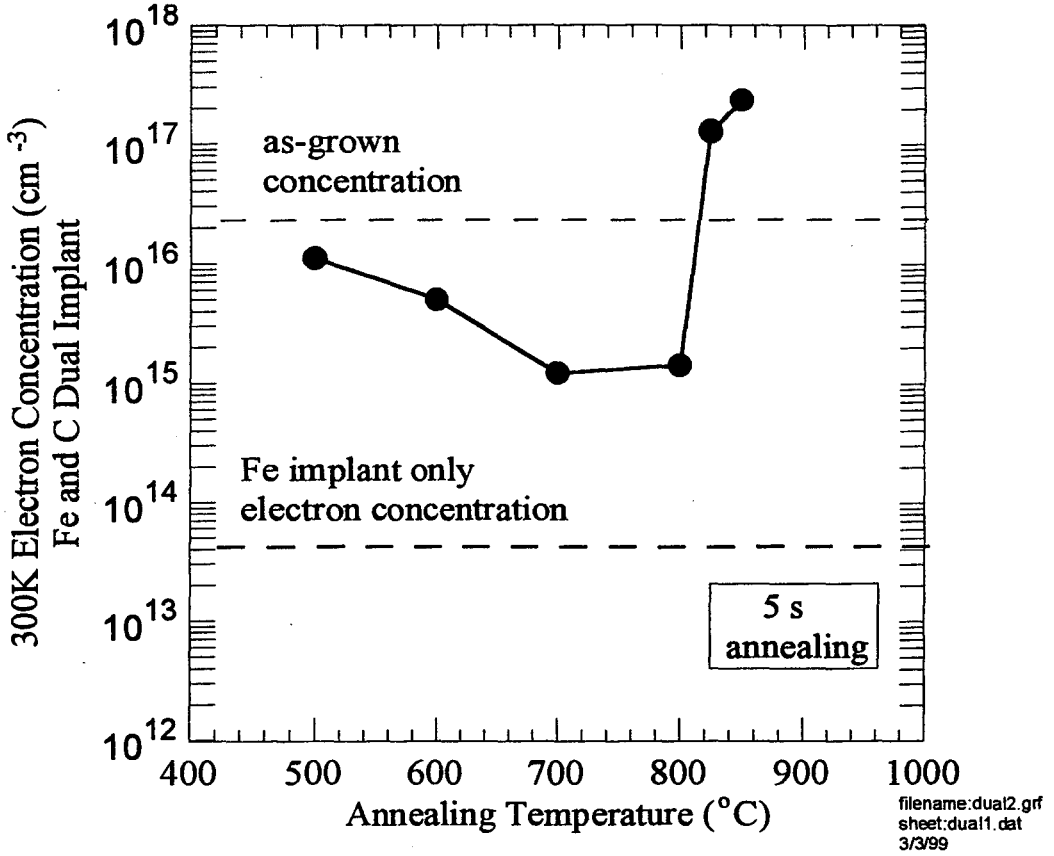

Fig. 4.13 Room temperature electron concentration measurements for the Fe^+ and C^+ implanted $In_{0.53}Ga_{0.47}As$ layers as a function of annealing temperature. The samples were annealed for 5s. The electron concentrations of the as-grown and the Fe^+ implanted only layers are also shown.

4.3 *Diffusivity of Fe in $In_{0.53}Ga_{0.47}As$*

To further our understanding of Fe diffusion in $In_{0.53}Ga_{0.47}As$, experiments were performed to measure the diffusivity of Fe. As-grown layers were annealed in a sealed ampoule at 550°C for 1 hour. These experiments were designed so that the Fe in InP substrate served as a supply of Fe atoms for the outdiffusion process. Performing the SIMS analysis (Fig. 4.14), we observed something which was very interesting and unexpected. It was apparent that there was significant in-diffusion of Fe from the outer surface, in addition to the some interdiffusion at the boundary between the epilayer and the substrate. The indiffusion of Fe from the surface may be attributed to some form of Fe contamination, although precautions were taken during the sample preparation process to minimize any sort of contamination. Autodoping may also be responsible for this Fe indiffusion. It is possible that the Fe out-diffuses from the Fe doped substrate and enters the $In_{0.53}Ga_{0.47}As$ film. In order to conclusively ascertain the source of Fe contributing to near the surface distribution, a control experiment was performed in which the $In_{0.53}Ga_{0.47}As$ layer used was grown on a S-doped substrate, instead of a Fe-doped one. It is clearly evident from the SIMS profile (Fig. 4.15), that in this case there was also significant indiffusion of Fe from the surface. Based on these results the possibility of autodoping from the substrate is excluded and contamination is confirmed as the source of Fe indiffusing from the surface. We can calculate that 10^{13} atoms cm^{-2} of Fe contamination (less than a monolayer) produces the surface profile observed in Fig. 4.14. The small concentration of residual Fe impurities necessary to form the observed contamination may be found in the etchants used or in the bulk GaAs which was crushed and added to the ampoule to provide the As overpressure.

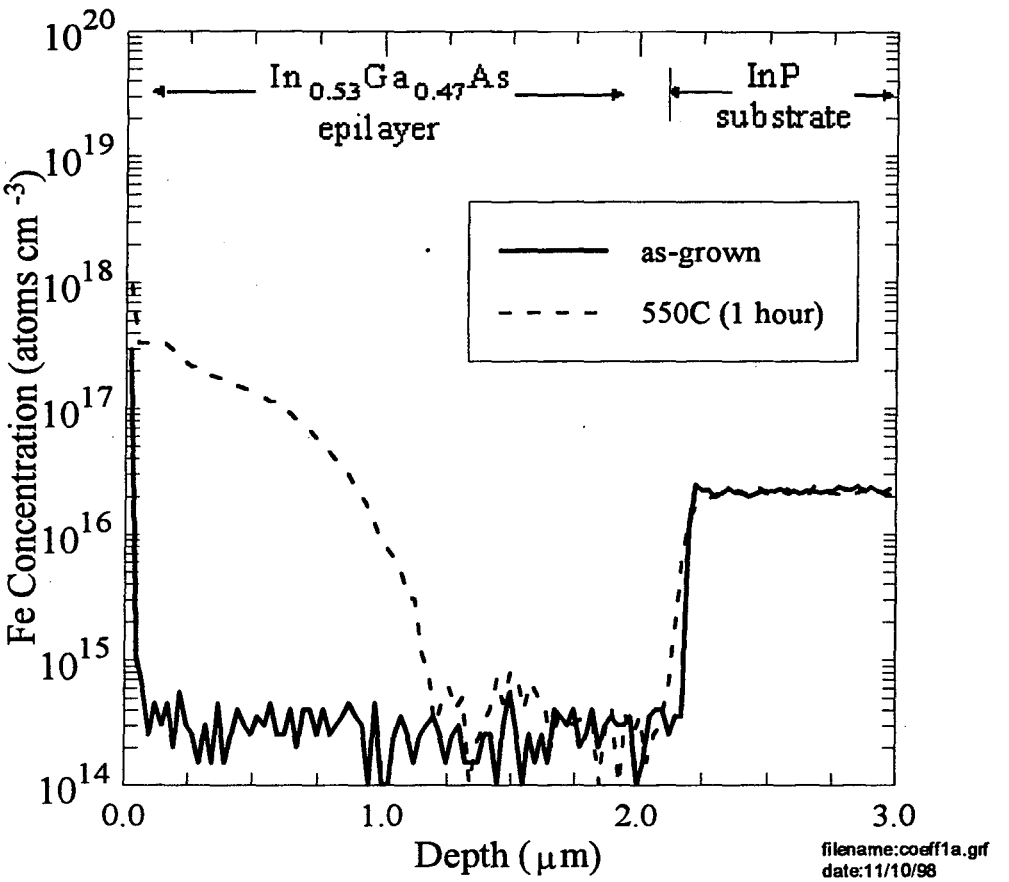

Fig. 4.14 SIMS depth profiles for $In_{0.53}Ga_{0.47}As$ layers as-grown (bold solid line) and annealed at 550°C for 1hr (dashed line). The $In_{0.53}Ga_{0.47}As$ layer was grown on Fe doped substrate.

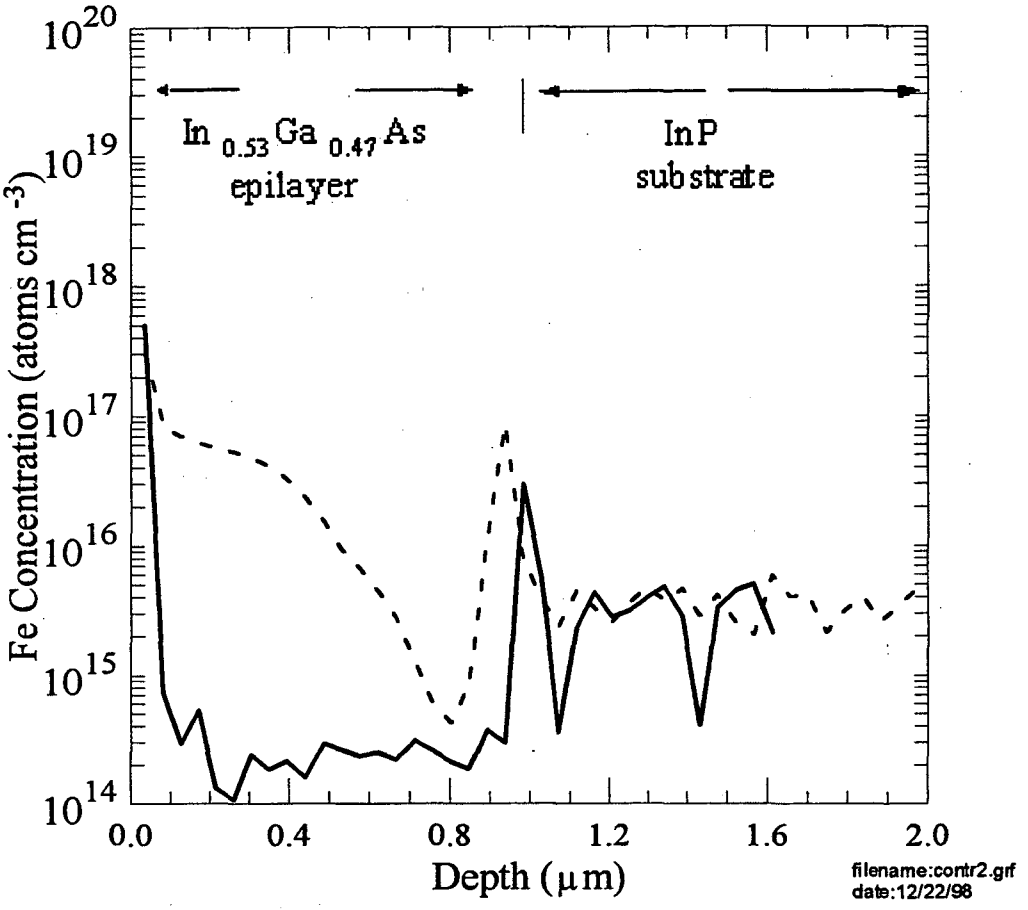

Fig. 4.15 SIMS depth profiles for $In_{0.53}Ga_{0.47}As$ layers: as-grown (bold solid line) and annealed at 550°C for 1hr (dashed line). The $In_{0.53}Ga_{0.47}As$ layer was grown on a S doped substrate.

Nevertheless, from the SIMS analysis (Fig. 4.14) a classic complementary error function distribution is obtained at the surface from which a diffusion coefficient of $4x10^{-13}cm^2s^{-1}$ is derived for T= 550°C. It is not possible to fit the Fe concentration profile at the interface with a complementary error function due to the composition gradient which exists in the region near the interface. In a case such as this, the diffusivity is composition dependent.

Since, we found no values reported in the literature for the diffusivity of Fe in $In_{0.53}Ga_{0.47}As$, the diffusion coefficient of Fe in other III-V semiconductors was compared to the one obtained in these experiments. Although, it is noteworthy that these materials are very different from $In_{0.53}Ga_{0.47}As$ and that the purpose of this comparison was to get an idea of how the diffusivity obtained in these experiments compares with that obtained for other semiconductors. The diffusivities of Fe in GaAs and InP were calculated using reported values of the pre-exponential factors and the activation energies and extrapolating to 550°C (the temperature for which the diffusivity was measured for $In_{0.53}Ga_{0.47}As$) (Table 4.2). As usual there is a large spread in the values obtained for the diffusion coefficients. Some factors which may explain these discrepancies include: (1) different methods used in the study of the diffusion behavior, and (2) different semiconductor materials (e.g.., different concentrations of dislocations, native defects, impurities, etc.). The diffusivity of Fe in $In_{0.53}Ga_{0.47}As$ which was measured in this work is consistent with the value reported for GaAs by Boltaks et al. (Boltaks et al. 1975).

Using the most recent values for the diffusivity of Fe in InP, given in Table 4.2, it is evident that the diffusivity of Fe in InP is lower than in $In_{0.53}Ga_{0.47}As$. This is also confirmed qualitatively by the results given in Fig. 4.14.

Table 4.2 Diffusion data for Fe in GaAs and InP.

III-V	Temperature Range (°C)	D_o ($cm^2 s^{-1}$)	E_a (eV)	$D_{550°C}$ ($cm^2 s^{-1}$)	Reference
GaAs	850-1150	$4.2x10^{-2}$	1.8	$3.98x10^{-13}$	Boltaks et al. 1975
	750-1050	$2.2x10^{-3}$	2.32	$1.36x10^{-17}$	Uskov et al. 1974
	950-1100	$1.5x10^{-2}$	2.0	$8.47x10^{-15}$	Prikhodko et al. 1978
InP	610-950	3	2.0	$1.7x10^{-12}$	Shishiyanu et al. 1977
	580-720	$6.8x10^{5}$	3.4	$1.03x10^{-15}$	Holmes et al. 1981
	700-900	$2.5x10^{-4}$	1.7	$9.71x10^{-15}$	Kamda et al. 1984

4.4 *Interfacial impurity gettering in $In_{0.53}Ga_{0.47}As$*

From the SIMS analysis (Fig.4.11), it is evident that a pile-up of Fe atoms occurs at the interface between the epilayer and the substrate. This phenomenon is observed for annealing temperatures as low as 700°C. We formed several hypotheses in an attempt to explain this gettering effect. They include: (1) the pileup is the result of thermal strain, (2) or an artifact of the SIMS analysis, or (3) is related to the nature of the interface. Any kind of strain at the interface may lead to defects causing impurity gettering in this region. One source of strain may be attributed to a lattice mismatch between the epilayer and the substrate. X-ray diffraction was performed to determine the lattice mismatch between the epilayer and the substrate. The peaks for the epilayer and the substrate for the (400) reflection are shown in Fig. 4.16. From the peak positions a lattice strain of 3.2×10^{-2} % is obtained. Since this number is very small, the effect of the strain due to the lattice mismatch is negligible.

Another source of strain can result from the difference between the thermal expansion coefficients between the epilayer and the substrate. The tabulated values for the linear thermal expansion coefficients for $In_{0.53}Ga_{0.47}As$ and InP are 5.66×10^{-6}/°C and 4.75×10^{-6}/°C, respectively. Using the following expression

$$\varepsilon = \Delta\alpha_{th}\, \Delta T \qquad (4.1)$$

for a ΔT=(700-25)°C a thermal strain of 0.06% is obtained. During thin film growth, a thermal strain is also produced. This contribution to the thermal strain is already incorporated within that strain determined from the x-ray measurements. Though, only a small fraction of the thermal strain is represented by this measurement since the growth occurred at ~ 500°C. In the above case the calculation for thermal strain was performed

at a temperature of 700°C which was the lowest temperature at which interfacial impurity gettering was observed in this series of experiments. For this reason, the strain obtained in the above calculation (0.06%) is found to be larger than the one from the x-ray measurements ($3.2x10^{-2}$ %). In any case, the thermal strain appears to be rather small and is believed to be negligible.

Interfacial impurity gettering may also be due to an artifact of the SIMS analysis. It is well known that a large concentration of an electronegative element (i.e., oxygen) in a sample can enhance the positive secondary ion yield of impurities (Brundle et al. 1992). Therefore, a large oxygen concentration at the interface would result in an enhanced Fe signal. To further investigate this possibility, a SIMS analysis was performed on the sample to measure the concentration of oxygen at the interface using a Cs^+ primary ion beam. From the oxygen SIMS profile (Fig. 4.17), there does not appear to be a high concentration of oxygen present at the interface between the epilayer and the substrate. Although, the effect of ion knock-on must be taken into consideration. Ion knock-on may lead to permanent displacement of impurities and result in a change of the original impurity distribution within the semiconductor material. This effect becomes pronounced when the sputtering process is performed from a region of higher atomic concentration to a lower one, as in this particular case.

Interfacial impurity gettering can most likely be attributed to the nature of an interface. An interface is a layer in which contamination and defects may be present. This latter hypothesis is confirmed by the observation that interfacial impurity gettering has been reported for homoepitaxy of InP (Fig. 4.18) (Chevrier et al. 1980). In such a homogeneous material system, there is neither a lattice mismatch nor a difference in the

linear thermal expansion coefficients between the epilayer and the substrate which could enhance impurity gettering.

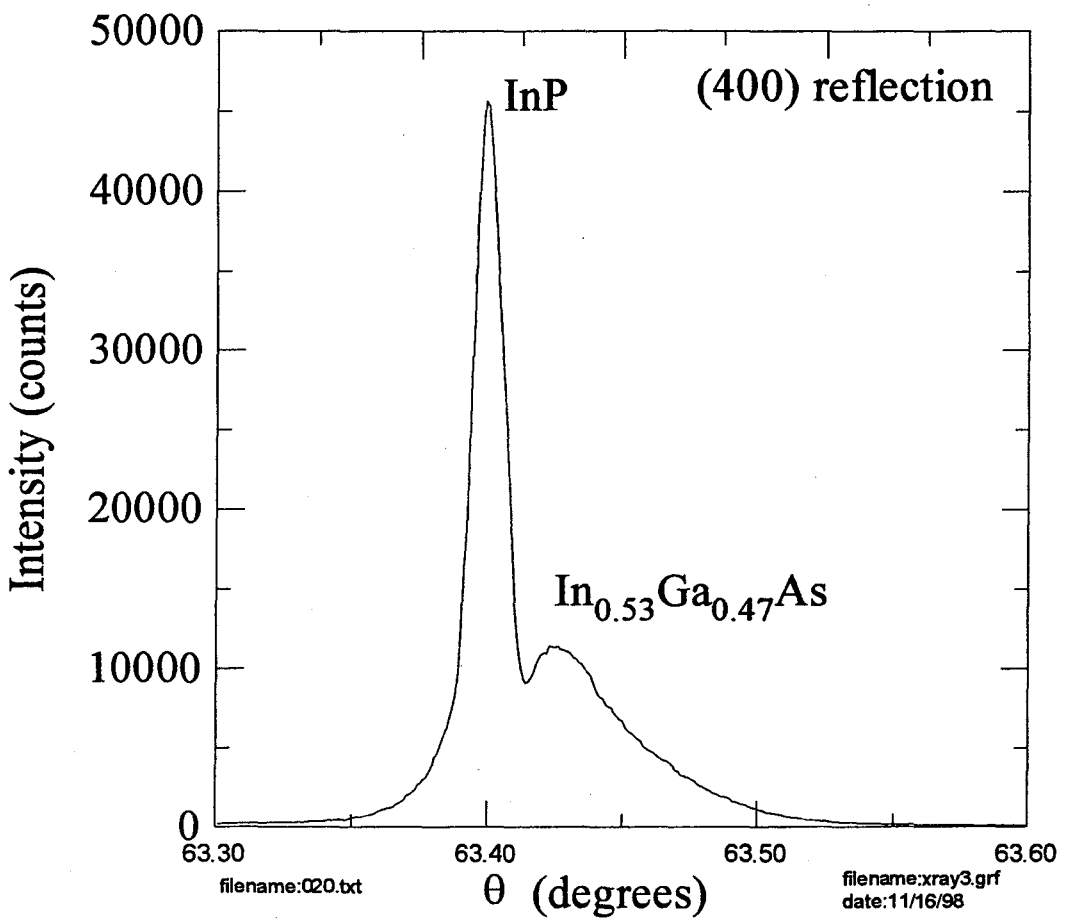

Fig. 4.16 X-ray diffraction curve for the (400) reflection for the $In_{0.53}Ga_{0.47}As$ epilayer grown on the InP substrate.

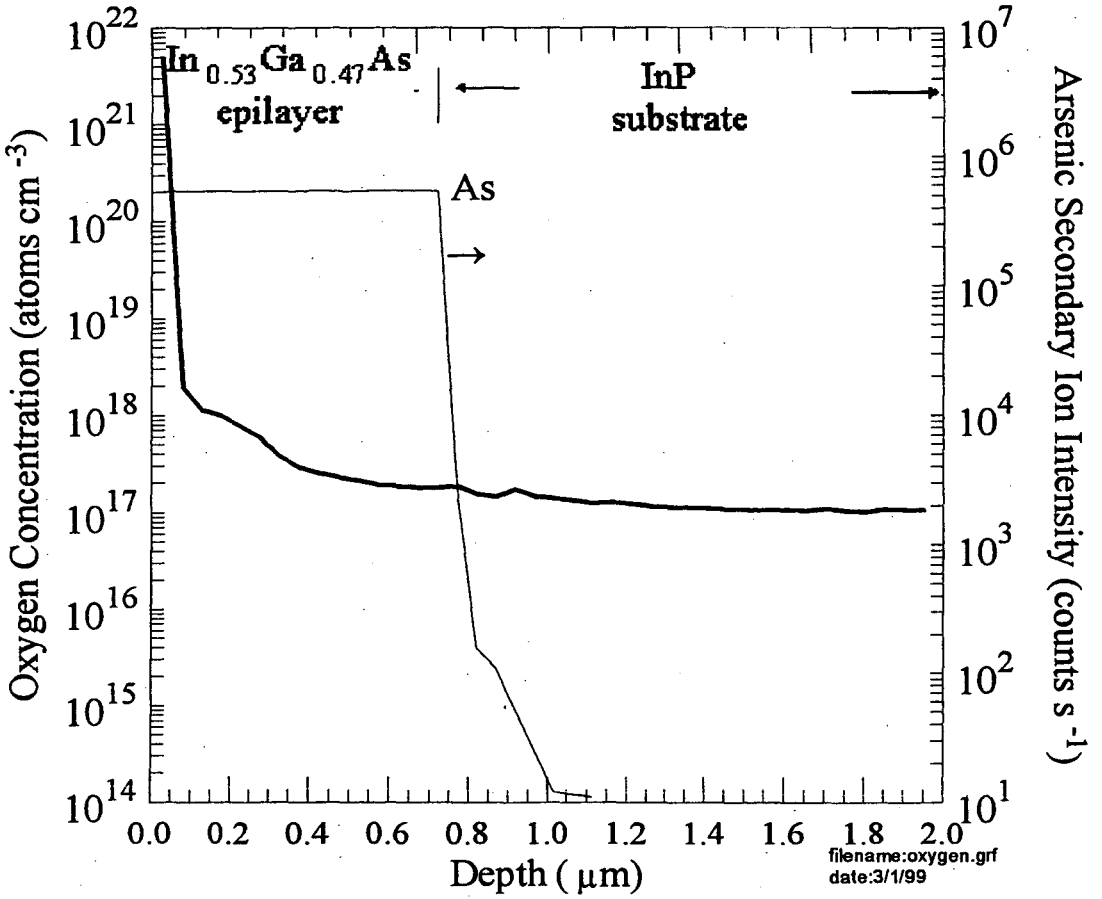

Fig. 4.17 SIMS depth profiles of the O concentration in $In_{0.53}Ga_{0.47}As$ as-grown epilayer. The $In_{0.53}Ga_{0.47}As$ layer was grown on a Fe doped substrate.

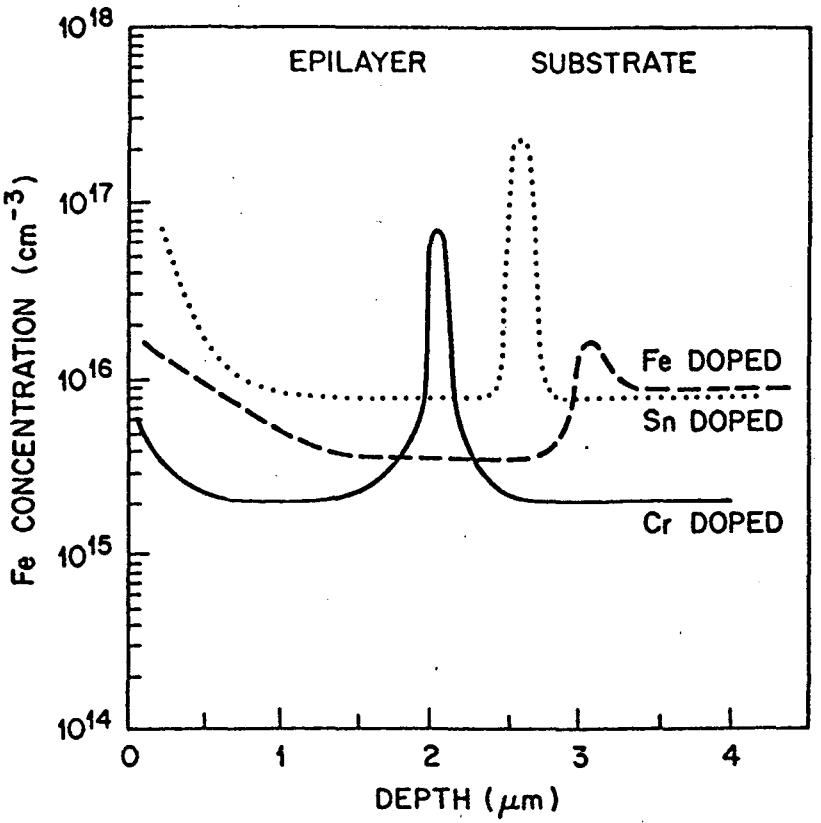

Fig. 4.18 SIMS depth profiles of the Fe concentration in epitaxial InP layers grown on Fe-doped, Sn-doped and Cr-doped substrates showing interfacial impurity gettering. (Chevrier et al. 1980)

5. Summary and Conclusions

The electrical properties of Ne^+ and Fe^+ implanted $In_{0.53}Ga_{0.47}As$ layers have been investigated. In addition, the thermal stability of the implant isolation in the layers was examined as a function of implant dose and annealing temperature. The Ne^+ implanted layers reach a maximum resistivity of 5 Ω-cm. This is an increase of two orders of magnitude compared to the resistivity of the as-grown layers. The stability of the resistive state of these layers extends up to a temperature of approximately 300°C. Similar defect annealing characteristics were observed for all of the Ne^+ implanted and annealed layers as is evident from the resistivity measurements (i.e., above 300°C the resistivity decreased for all of the samples). Radiation damage induced defects producing free charge carriers were observed upon implantation and during annealing. The concentration of these free carriers increased with increasing implantation dose. A phenomenological model was proposed to understand the annealing temperature dependency of the electron concentration. The electron concentration decreased up to annealing temperatures of ~475°C. At annealing temperatures greater than this the electron concentration increased due to the formation of complex donor-like defects which were stable in the temperature regime. The resistivities achieved via Ne^+ implantation are too low for practical device applications. Nevertheless, from these Ne^+ implantation studies, we gained valuable understanding of the effects of damage in ion implanted $In_{0.53}Ga_{0.47}As$ layers which could be applied to the Fe^+ implantation work.

A higher value of resistivity was achieved with Fe^+ implantation (770 Ω-cm). This resistivity value is near the intrinsic limit (~1000Ω-cm) which was the goal for this work. The SI properties of these layers were stable up to 800°C. No significant out-

diffusion of Fe was observed for the samples annealed up to this temperature. The free carrier concentration measured for the layer exhibiting the highest compensation was ~$2.7x10^{13}$ cm^{-3} which is almost two orders of magnitude greater than the intrinsic carrier concentration. We postulated that although the concentration of deep acceptors was greater than that of the shallow impurity donors, not all of the donors were compensated due to the formation of damage related donors or precipitation of impurity acceptors. Transmission Electron Microscopy and Selected Area Diffraction revealed no Fe precipitates in the implanted and annealed layers. From the electrical measurements, the Fermi energy for the layer exhibiting the highest compensation was calculated to lie 0.23 eV below the conduction band. This position of the Fermi level correlates well with the Fermi Stabilization energy (0.25 eV) in $In_{0.53}Ga_{0.47}As$ which was indicates the formation of damage related energy levels. Furthermore, channeling-RBS confirmed the presence of residual damage in the annealed layer (Fig. 4.8). It was evident that not all of the implantation damage was completely annealed out prior to electrical activation of the Fe.

Co-implantation of Fe (deep acceptor) and C (shallow acceptor) was investigated in an effort to increase the level of donor compensation in the $In_{0.53}Ga_{0.47}As$ layers. From the room temperature resistivity measurements (Fig. 4.12), it became apparent that the implantation of C did not increase the resistivity in the layers to values higher than what was achieved with implantation of Fe alone. This may be attributed to the formation of defect related energy levels which lie near the conduction band associated with the implantation process in $In_{0.53}Ga_{0.47}As$.

SIMS analysis (Fig.4.11) showed Fe out-diffusion which resulted in the loss of the semi-insulating electrical characteristics. To further our understanding of Fe

diffusion in $In_{0.53}Ga_{0.47}As$, the diffusion coefficient of Fe was measured for the first time. The diffusivity of Fe was measured to be $4x10^{-13}$ cm^2 s^{-1} at 550°C. This experimental value is consistent with the value reported for Fe diffusion in GaAs, $D_{GaAs,550°C}$~ $3.98x10^{-13}cm^2s^{-1}$ (Boltaks et al. 1975). The results from the diffusion studies suggest that Fe has lower diffusivity in InP than in $In_{0.53}Ga_{0.47}As$.

Several possibilities for interfacial impurity gettering (Fig. 4.11) in $In_{0.53}Ga_{0.47}As$ were proposed and discussed in detail. This phenomenon can most likely be attributed to the nature of the interface which may have defects and contaminants. Support is given to this hypothesis by the fact that interfacial impurity gettering has also been observed in homoepitaxy of InP (Chevrier et al. 1980).

Through a thorough understanding of the mechanisms of activation and redistribution of the Fe^+ in the annealed layers, it was possible to optimize the implantation and annealing conditions to produce $In_{0.53}Ga_{0.47}As$ layers of near uniform resistivities sufficiently high for device isolation purposes.

6. Further Research

It would be of particular interest to investigate the electrical properties of Ti^+ implanted $In_{0.53}Ga_{0.47}As$ layers. Ti is a promising transition metal for this purpose because it forms a midgap donor level in $In_{0.53}Ga_{0.47}As$ [$E_{C.B.}$-0.37 eV (Baber et al. 1992)]. In addition, it is possible that the solubility limit of Ti in $In_{0.53}Ga_{0.47}As$ may be higher than that of Fe. A higher solubility limit would allow for more compensation of free carriers. InP implanted with Ti^+ has shown less redistribution upon annealing as compared to Fe (Ullrich et al. 1991). This behavior was attributed to a higher solubility limit and a lower diffusivity of Ti in InP as compared to Fe. The technique that could be

employed would consist of producing a slightly p-type $In_{0.53}Ga_{0.47}As$ layer by implantation of shallow acceptors into the as-grown $In_{0.53}Ga_{0.47}As$. Subsequent implantation of Ti^+ would pin the Fermi level midgap. It would be interesting to compare the diffusive properties of the Ti^+ implanted layers with those obtained for the Fe^+ implanted layers in this work.

7. Appendices

Appendix A: Material properties of III-V semiconductors and alloys

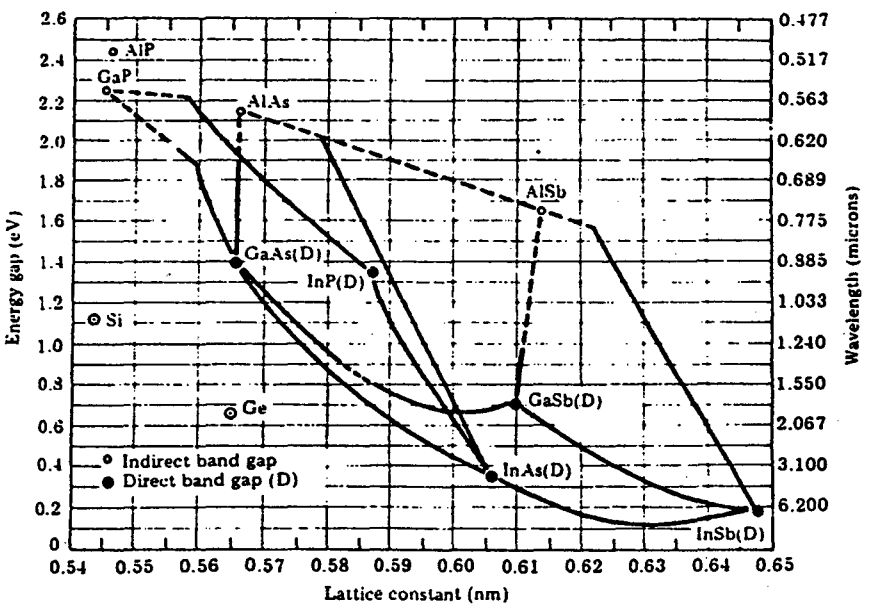

Fig. A.1 Energy gap and lattice constant for several III-V materials at room temperature. The boudaries joining the binary compounds give the ternary energy gap and lattice constant. The solid and dashed lines indicate direct and indirect band gap semiconductors, respectively. (Mayer et al. 1990)

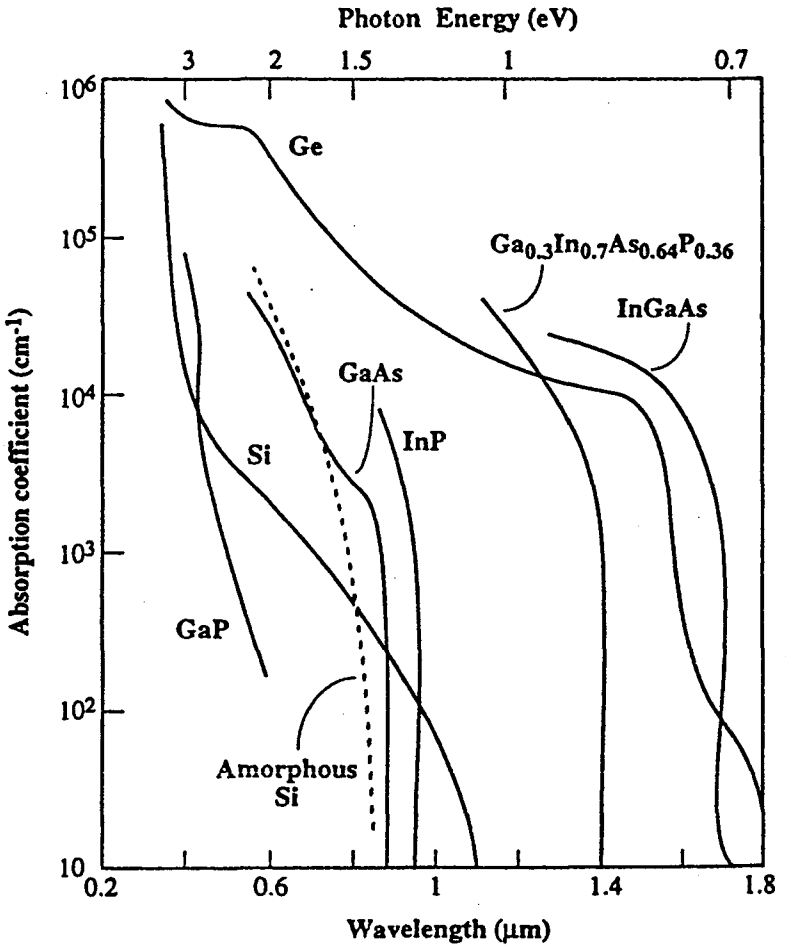

Fig. A.2 Logarithm of the linear absorption coefficient as a function of wavelength for several semiconductors. (Singh 1995)

Table A.1 Theoretical ground state and bound excited state energies in meV of acceptors in III-V semiconductors. (Baldereschi et al. 1973)

	$1S_{3/2}$	$2S_{3/2}$	$2P_{1/2}$	$2P_{3/2}$	$2P_{5/2}$
AlSb	42.4	12.4	3.3	17.5	10.5
GaP	47.5	13.7	4.2	19.1	11.7
GaAs	25.6	7.6	1.6	11.1	6.5
GaSb	12.5	3.8	0.65	5.6	3.2
InP	35.2	10.5	2.0	15.5	8.9
InAs	16.6	5.1	0.4	7.9	4.4
InSb	8.6	2.7	0.2	4.2	2.3

Table A.2 Electronic properties of several semiconductors at room temperature.

Property	GaAs	InAs	$In_{0.53}Ga_{0.47}As$	InP
E_g(eV)	1.424	0.354	0.75	1.27
m^*/m_o	0.063	0.022	0.032	0.08
$n_i(cm^{-3})$	$2.3x10^6$	$1.3x10^{15}$	$6.7x10^{11}$	$3.8x10^7$
$\Delta E_{\Gamma\Lambda}$ (eV)	0.33	0.87	0.61	0.61
$v_{sat}(10^7$ cm/s)	1.8	3.5	2.1	2.4
μ_e (cm^2 V^{-1} s^{-1})	$8.0x10^3$	$3.0x10^4$	$1.0x10^4$	$4.5x10^3$
μ_h (cm^2 V^{-1} s^{-1})	300	450	300	300
$\rho_i(\Omega$-cm)	$3.3x10^8$	0.16	900	$3.4x10^7$

Appendix B: Implant Conditions

Sample	Implant Ion (Implant Temperature)	Energy (keV)	Dose (atoms cm^{-2})	Implant Ion Concentration (atoms cm^{-3})
A3-1	Ne (RT)	200 100 50	$1x10^{11}$ $4x10^{10}$ $2x10^{10}$	$5x10^{15}$
A3-2	Ne (RT)	200 100 50	$1x10^{13}$ $4x10^{12}$ $2x10^{12}$	$5x10^{17}$
A3-3	Ne (RT)	200 100 50	$1x10^{15}$ $4x10^{14}$ $2x10^{14}$	$5x10^{19}$
Sample#1 Fe-RT	Fe (RT)	900 500 300 210 85 40	$8x10^{13}$ $2x10^{13}$ $1.5x10^{13}$ $2x10^{12}$ $7x10^{12}$ $1x10^{12}$	$2x10^{18}$
Sample #1 Fe-LN	Fe (LN)	900 500 300 210 85 40	$8x10^{13}$ $2x10^{13}$ $1.5x10^{13}$ $2x10^{12}$ $7x10^{12}$ $1x10^{12}$	$2x10^{18}$
Sample #2 Fe-RT	Fe (RT)	1250 700 400 250 90	$1.25x10^{14}$ $4x10^{13}$ $2x10^{13}$ $1.3x10^{13}$ $8x10^{12}$	$2x10^{18}$
Sample #2 Fe-LN	Fe (LN_2)	1250 700 400 250 90	$1.25x10^{14}$ $4x10^{13}$ $2x10^{13}$ $1.3x10^{13}$ $8x10^{12}$	$2x10^{18}$
Sample #3 Fe-RT	Fe (RT)	1250 700 400 250 90	$1.25x10^{13}$ $4x10^{12}$ $2x10^{12}$ $1.3x10^{12}$ $8x10^{11}$	$2x10^{17}$

Sample	Implant Ion (Implant Temperature)	Energy (keV)	Dose (atoms cm^{-2})	Implant Ion Concentration (atoms cm^{-3})
Sample #4	Fe	1250	$1.25x10^{14}$	$2x10^{18}$
	(RT)	700	$4x10^{13}$	
		400	$2x10^{13}$	
		250	$1.3x10^{13}$	
		80	$8x10^{12}$	
	C	400	$4x10^{13}$	$1.6x10^{18}$
	(RT)			

Appendix C: Major characterization techniques

C.1 Hall Effect and resistivity

An extensive review of Hall Effect has been given by Schroder (1990). Deflection of charge carriers moving in a magnetic field is the basis of Hall Effect. The configuration for Hall Effect measurements for a p-type sample is shown in Fig. C.1. The current **I** (holes) flows in the positive x-direction. The magnetic field points in the positive z direction. A charged particle **q** in a magnetic field **B** experiences a Lorentz force:

$$\overline{F} = q\left(\overline{v}x\overline{B}\right) \tag{C.1}$$

The holes are deflected in the negative y direction which produces an electric field ($\mathbf{E_H}$) in the positive y direction. At equilibrium, the Lorentz force along the y direction is balanced by the electrostatic force caused by the initial separation of charge. No further deflection of charge carriers occurs after equilibrium is established. This balance of electrostatic and electromagnetic forces results in the following relations:

$$q\left(\overline{v}x\overline{B}\right) = q\overline{E}_H \tag{C.2}$$

$$E_H = vB = \frac{JB}{qp} = R_H JB \tag{C.3}$$

where **J** is the current density, **p** is the hole concentration, and $\mathbf{R_H}$ is the Hall coefficient. In the case of conduction by both electrons and holes, the Hall coefficient is:

$$R_H = \frac{r\left(p - b^2 n\right)}{q\left(p + bn\right)^2} \tag{C.4}$$

b is the ratio of electron and hole mobilities (μ_n/μ_p) and **r** is a scattering factor which depends on the type of scattering mechanism in the semiconductor and has values

ranging between 0.5 and 2. For lattice scattering **r** is $3\pi/8$, for ionized impurity scattering this factor is $315\pi/512$, and for neutral impurity scattering **r** is 1 (Smith 1959 and Beer 1963). At sufficiently large **B** ($B\mu >> 1$) **r** approaches unity.

If the current were carried by electrons, the carriers drift velocity would be along the negative x direction. The electrons would be deflected in the negative y direction (same direction as the holes). Consequently the Hall field would point in the negative y direction, so that the polarity of the Hall potential is reversed for electrons as compared to that of holes. Thus, the polarity of the Hall voltage directly shows whether the current is carried by holes or electrons.

The electrical contacts on the samples used in this work were prepared for Hall Effect measurements using van der Pauw's method (van der Pauw 1958a and 1958b). Conformal mapping is used in van der Pauw's theory of Hall Effect measurement of irregularly shaped samples (Fig. C.2). He showed that the resistivity and carrier concentration of a flat sample of arbitrary shape can be determined if the following requirements are fulfilled: 1) the contacts are at the periphery of the sample, 2) the contacts are small, 3) the sample is homogeneous in thickness and resistivity, and 4) singly connected (the sample does not contain any isolated holes). Van der Pauw's finds that the resistivity can be expressed in the form:

$$\rho = \frac{\pi d}{\ln 2} \frac{\left(R_{12,34} + R_{23,41}\right)}{2} f\left[\frac{R_{12,34}}{R_{23,41}}\right] \qquad \text{(C.5)}$$

for a layer of thickness **d** and where $\mathbf{R_{12,34}} = \mathbf{V_{34}/I_{12}}$. The resistance is obtained by dividing the voltage across contact 3 and contact 4, by the current which enters the

sample at contact 1 and leaves through contact 2. f is a weak function of $R_{12,34}/R_{23,41}$ ($\mathbf{R_r}$) and satisfies the relation:

$$\frac{R_r - 1}{R_r + 1} = \frac{f}{\ln(2)} \arccos h\left\{\frac{\exp\left[\ln 2 / f\right]}{2}\right\} \tag{C.6}$$

This function is plotted in Fig. C.3. The Hall coefficient can be found using the expression:

$$R_H = \frac{d\Delta V_{24,13}}{2BI} \tag{C.7}$$

where $\Delta V_{24,13} = V_{24}(+B) - V_{24}(-B)$. Measurements are taken with the polarity of the magnetic field reversed (i.e., +B, -B).

The conductivity of a two layer structure and substrate conduction must be examined in detail, since electrical measurements in this thesis were performed on epilayers grown on semi-insulating substrates. For an epilayer of thickness $\mathbf{d_l}$ on a substrate of thickness $\mathbf{d_s}$ the ratio of the resistances of the epilayer and substrate is:

$$\frac{R_l}{R_s} = \frac{\rho_l d_s}{\rho_s d_l} \tag{C.8}$$

For semi-insulating InP substrate, a typical value of ρ_s is 2.7×10^7 Ω-cm and a typical wafer thickness is 500 μm. If the epilayer thickness is 0.7 μm, then the calculation of the ratio of resistances yields:

$$\frac{R_l}{R_s} = \rho_l \left(2.6 \times 10^{-5}\right) \tag{C.9}$$

If the resistivity of the epilayer is greater than 10^5 Ω-cm then the substrate will be carrying an appreciable fraction of the current. For these measurements, the current

carried through the substrate can be neglected; since the maximum resistivity measured for the epilayer was ~770 Ω-cm.

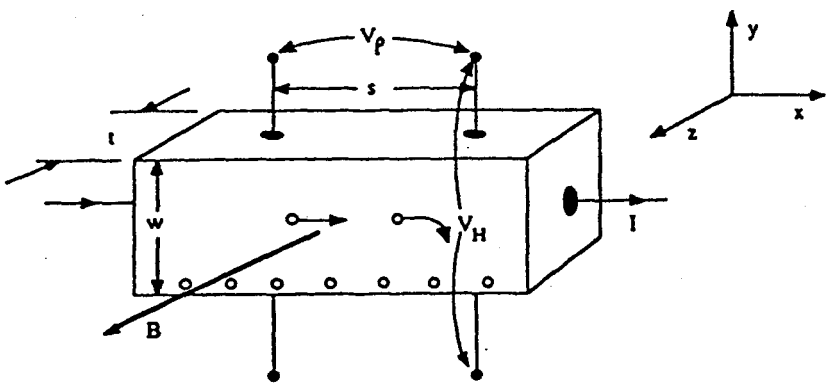

Fig. C.1 Geometry for Hall Effect measurement of a p-type semiconductor.

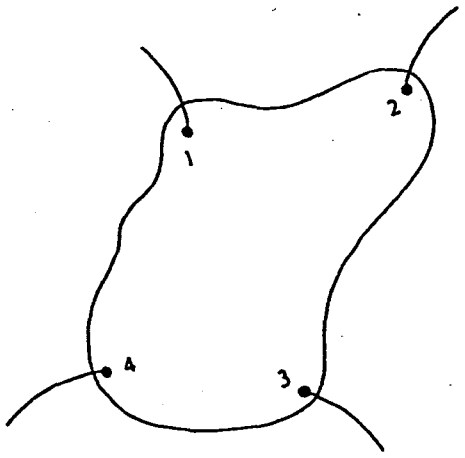

Fig. C.2 Electrical contact configuration using van der Pauw method.

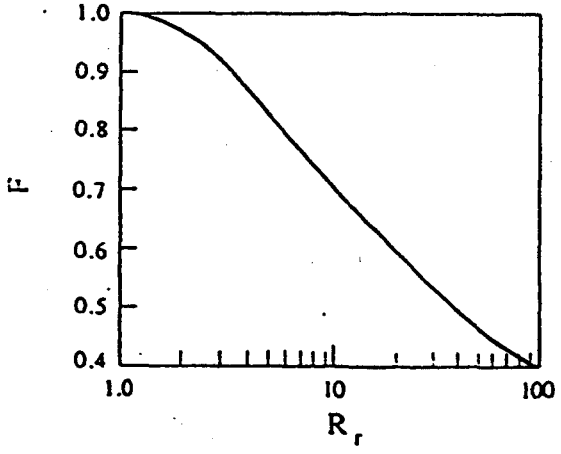

Fig. C.3 The dependence of f on the ratio $R_{12,34}/R_{23,41}$.

C.2 Rutherford backscattering spectrometry (RBS) and channeling RBS (c-RBS)

For RBS typically a Van de Graaf accelerator is used to produce a He^+ ion beam in the MeV energy range. The high energy beam (1-2 MeV) of monoenergetic collimated light ions (H^+, He^+) is directed towards the sample. A small number of the light ions are backscattered and are detected by a solid state detector that measures the energy of the particles. Some of the applications of RBS include: accurate determination of stoichiometry, elemental aerial density, and impurity distributions in thin films.

Some of the advantages of this technique include the following: (1) it is an absolute method that does not require the use of standards (2) the technique is quick with typical acquisition times of about 10 minutes, and (3) it is relatively nondestructive as compared to other characterization techniques such as SIMS and TEM. One of the disadvantages of RBS is that it has a poor sensitivity to light elements in heavy matrices. Some references which discuss Rutherford Backscattering Spectrometry (RBS) are Chu et al. 1978, Ziegler 1985, Rimini 1995, Tesmer et al. 1995, and Schroder 1990.

Channeling RBS is used for the evaluation of lattice damage in thin films. For channeling RBS the sample is mounted on a goniometer. Fig. C.4 is a schematic diagram of the RBS setup for channeling experiments. The sample can be rotated through a tilt angle θ (rotation about the vertical axis) and azimuthal angle ϕ (rotation about the crystal normal).

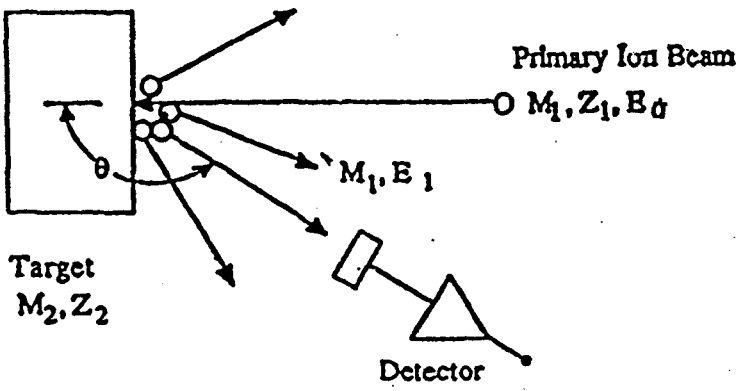

Fig. C.4 Schematic illustration of RBS setup.

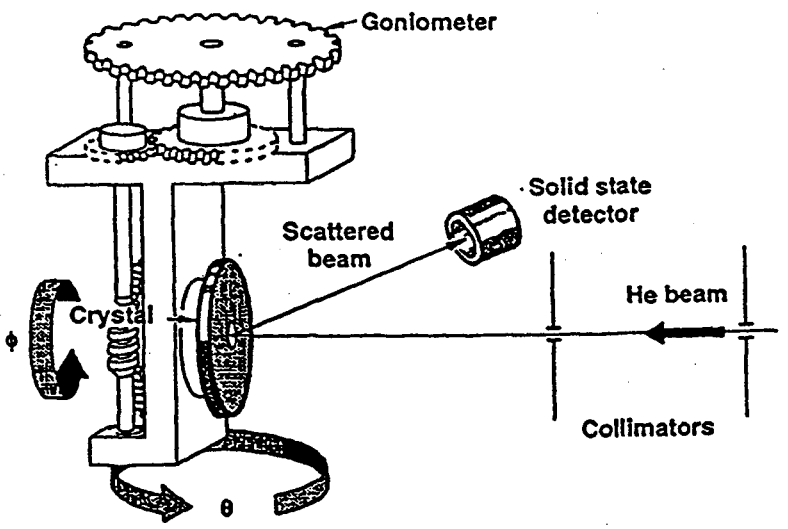

Fig. C.5 Schematic view of the setup for channeling experiments. The ion beam impinges on the sample mounted on a two axis goniometer. (Tesmer et al. 1995)

A schematic diagram of the RBS process is illustrated in Fig. C.5. The projectile ions are of mass $\mathbf{M_1}$, atomic number $\mathbf{Z_1}$, and energy $\mathbf{E_0}$. $\mathbf{M_2}$ and $\mathbf{Z_2}$ are the mass and atomic number of the target (sample). Most of the incident ions lose their energies through electronic collisions and are stopped at some depth below the sample surface. A small fraction of these projectile ions undergo nuclear collisions with the target atoms and are backscattered. These ions lose energy traversing the sample from the point of entry to the scattering location and again on the way back to the surface. They exit the sample and are detected by the detector if they reside in the proper solid angle. Using the principles of conservation of energy and momentum the kinematic relationship can be computed. The kinematic factor is defined as the ratio of the projectile's energy after the collision to its energy before the collision ($\mathbf{E_1/E_0}$) and is:

$$k = \frac{\left[\sqrt{1-(R\sin\theta)^2} + R\cos\theta\right]^2}{(1+R)^2} \qquad \text{(C.10)}$$

where $\mathbf{R}$ is defined by M_1/M_2 and θ is the scattering angle. In order to obtain high mass resolution the kinematic factor should be as large as possible. This can be achieved by placing the detector at a large angle with respect to the incident beam (close to 180°). The unknown mass of the sample can be calculated using the above kinematic expression, since $\mathbf{E_1}$ can be measured and θ, $\mathbf{E_0}$ and $\mathbf{M_1}$ are known parameters.

The relative number of particles backscattered from a target atom into a given solid angle Ω for a given number of incident ions is related to the differential scattering cross section (Chu et al. 1978):

$$\frac{d\sigma}{d\Omega} = \left(\frac{Z_1 Z_2 q^2}{4E}\right)^2 \frac{4}{\sin^4\theta} \frac{\left[\sqrt{1-(R\sin\theta)^2} + \cos\theta\right]^2}{\sqrt{1-(R\sin\theta)^2}} \qquad \text{(C.11)}$$

E is the energy of the projectile particle immediately before scattering. Typical values for scattering cross section of He particles are 1 to 10×10^{-24} cm^2/sr. Since $d\sigma/d\Omega$ can be accurately calculated quantitative measurement can be achieved by RBS. The scattering cross section is proportional to the square of Z_2 (target atomic number). As a result RBS is more sensitive to heavy elements than light elements. RBS allows one to determine the aerial density of atomic species at a depth x by measuring the height of the spectrum. The height of the spectrum (also called the backscattering yield) gives the total number of detected ions or counts. The backscattering yield can be calculated as follows:

$$A = \sigma \Omega Q N_s \tag{C.12}$$

Ω is the detector solid angle in steradians, Q is the total number of ions incidents on the sample, and N_s is the aerial density.

In addition to elemental and quantitative information, RBS is also depth sensitive. A particle which is backscattered from the bulk will have less energy than a projectile ion backscattered from the same element near the surface (see Fig. C.6). This is because a particle below the surface has to undergo electronic collisions and loses energy in order to traverse a distance x from the target surface. The projectile particle at a depth x below the sample surface loses energy on its way in (ΔE_{in}) and on its way out after it is backscattered (ΔE_{out}). Using these energy loss processes RBS can be used to determine the thickness of layers. The detected energy of the projectile ions backscattered from target atoms at a depth x which reaches the detector is:

$$E_1(x) = \left[E_o - \left(\frac{dE}{dx} \right)_{in} \frac{x}{\cos \theta_1} \right] K - \left(\frac{dE}{dx} \right)_{out} \frac{x}{\cos \theta_2} \tag{C.13}$$

$$= KE_o - \left[K\left(\frac{dE}{dx}\right)_{in} \frac{1}{\cos\theta_1} + \left(\frac{dE}{dx}\right)_{out} \frac{1}{\cos\theta_2} \right] x$$

It is a ratio of the measured backscattered energy to the incident energy of the analyzing ion. The film thickness **x** can be calculated from the energy difference **ΔE** between the projectile ions backscattered from the surface and from the place of interaction at a depth x:

$$\Delta E = KE_o - E_1(x) = \left[K\left(\frac{dE}{dx}\right)_{in} \frac{1}{\cos\theta_1} + \left(\frac{dE}{dx}\right)_{out} \frac{1}{\cos\theta_2} \right] x = [S]x \quad \text{(C.14)}$$

S is the backscattering energy loss factor. **S=N[ε]** where **N** is the volume density and **[ε]** is known as the backscattering stopping cross section factor. Values for the energy loss factor for He^+ ion in various materials are well known and can be found in many reference books (see for example Tesmer et al. 1995).

For solid phase epitaxial studies it is crucial to accurately measure amorphous layer thicknesses. To maximize **ΔE** for small change in **x**, i.e., to improve depth resolution, **[S]** should be maximized. The backscattering energy loss factor can be maximized by using the glancing exit angle geometry where θ_2 is large. In this geometry, the detector is placed at a glancing exit angle with the sample surface (θ~100°with respect to the beam). A small change in depth measured along the normal corresponds to a large outgoing path and increased energy loss. The effect is to increase the ion path length required to reach a given depth in the sample measured perpendicularly to the surface.

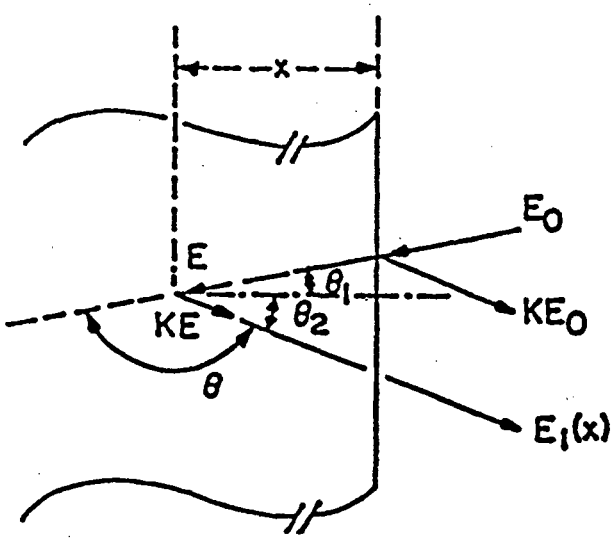

Fig. C.6 Schematic diagram of sample relative to the incident beam. The incident energy of the beam is E_o. The particles backscattered from a depth x from the surface exit the sample with $E_1(x)$.

Channeling is an ion steering effect resulting from the Coulomb repulsion between the positive charged projectiles and the target atoms along rows or planes in a single crystal. Due to the steering action, the ions are directed towards the center of the channel. Since the ions do not come closer than the screening distance of the atoms the probability of large angle backscattering is reduced.

The critical angle for channeling can be expressed as:

$$\Psi_c = \sqrt{\frac{2Z_1Z_2e^2}{Ed}} \qquad \text{(radians)} \qquad \text{(C.15)}$$

$\mathbf{Z_1}$ and $\mathbf{Z_2}$ are the atomic numbers of the projectiles and target atoms, respectively. The spacing between the planes is given by **d** and **e** is the electronic charge ($\mathbf{e^2}$=1.44x10^{-13}cm MeV). Ions entering near the center of a channel are steered within the channel if they travel within the critical angle (eq. C.15). For MeV ^{4}He ions, the critical angle is usually 1 to 2 degrees. Channeling allows for the determination of the lattice location of impurities and the depth profile of the lattice damage if the analysis is performed on a single crystal substrate. Channeling RBS has been used extensively to study solid phase epitaxial regrowth of ion implanted semiconductors. This technique has been reviewed in many references (Rimini 1995, Tesmer and Nastasi 1995).

Whether the thin film is amorphous or single crystal can be determined from channeling RBS. When a sample is "channeled" the rows of the atoms are aligned parallel to the incident projectile ions. Consequently, the projectile ions can penetrate deeply into the sample and have a low probability of becoming backscattered. When an ion beam is aligned with an axis of the single crystal substrate with an amorphous or polycrystalline overlayer, the channeled RBS spectrum shows the random yield (amorphous) for a certain energy width corresponding to the overlayer and then

decreases. The decrease in backscattering yield occurs at the crystalline/amorphous interface where channeling begins. The channeling yield from the substrate appears greater than that of a perfect single crystal because a larger fraction of the particles in the beam are dechanneled due to scattering when traversing the amorphous layer.

An ion beam aligned with a single crystal channel can be dechanneled by defects in the crystal. The ratio of dechanneling to channeling can be used to qualitatively gauge the extent of perfection of a crystal. The height of the spectrum (number of counts per channel) in the underlying crystalline region depends on the thickness of the amorphous layer and decreases with amorphous layer thickness. In an amorphous layer, the aligned yield equals the random yield. Fig. C.7 shows the spectrum for a nearly perfect crystal, an amorphous layer, and a defective crystal. The surface peak for the aligned spectra corresponds to the scattering from the surface oxide layer.

The normalized yield is:

$$\chi = \frac{channeled\ \ yield(\Psi = 0)}{random\ yield\ (\Psi > \Psi_c)} \tag{C.16}$$

χ is a measure for the fraction of dechanneled ions. The rate of change of χ with depth is proportional to the concentration of displaced host atoms. For an amorphous or polycrystalline material χ is one. In channeling RBS, an abrupt interface is indicated by a sharp step in the aligned spectrum.

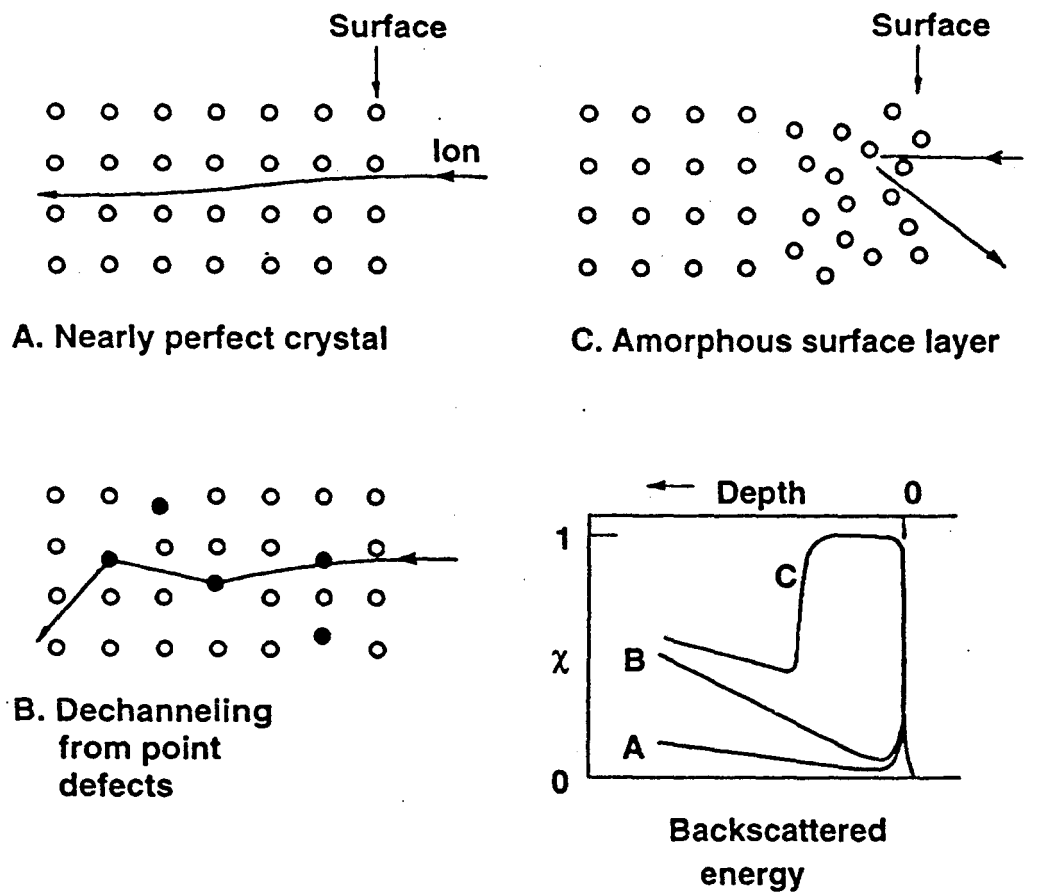

Fig. C.7 Channeling in (a) nearly perfect crystal, (b) crystal with point defects, (c) an amorphous material. The channeling RBS spectrum is for the three cases is shown in (d). (Tesmer 1995)

C.3 Electrochemical capacitance-voltage (ECV) measurements

Electrochemical capacitance-voltage measurements determine the net-dopant concentration as a function of depth. An electrolyte is used to both etch the sample and to form a Schottky contact. A schematic of the electrochemical cell which was used for capacitance-voltage measurements is shown in Fig. C.8. The semiconductor sample is pressed against a sealing ring in the electrochemical cell containing the electrolyte. The plunger presses the semiconductor against the semiconductor. The pump jet is used to agitate the electrolyte and disperse bubbles on the semiconductor surface. The semiconductor is referred to as the working electrode. In addition, there are three other electrodes in the setup. The platinum electrode is used for C-V measurement. The carbon (counter) electrode completes the circuit for etching. The saturated calomel electrode serves as a reference electrode in which the equilibrium (or rest) and overpotential can be measured. Etching of the semiconductor occurs by passing a current between the working electrode and the counter electrode. When there is no current flowing between the counter and working electrode, the potential which is measured is the rest potential. The semiconductor type can be determined by comparing the rest potential with and without illumination. Illumination of the semiconductor results in the creation of electron-hole pairs in the depletion region. These carriers are swept out in opposite directions due to the electric field. Since, p-type and n-type semiconductors produce photovoltages of opposite signs, the type of the semiconductor can be determined. For p-type semiconductor the electrode potential becomes more positive, and conversely for the n-type semiconductor the electrode potential will become more negative.

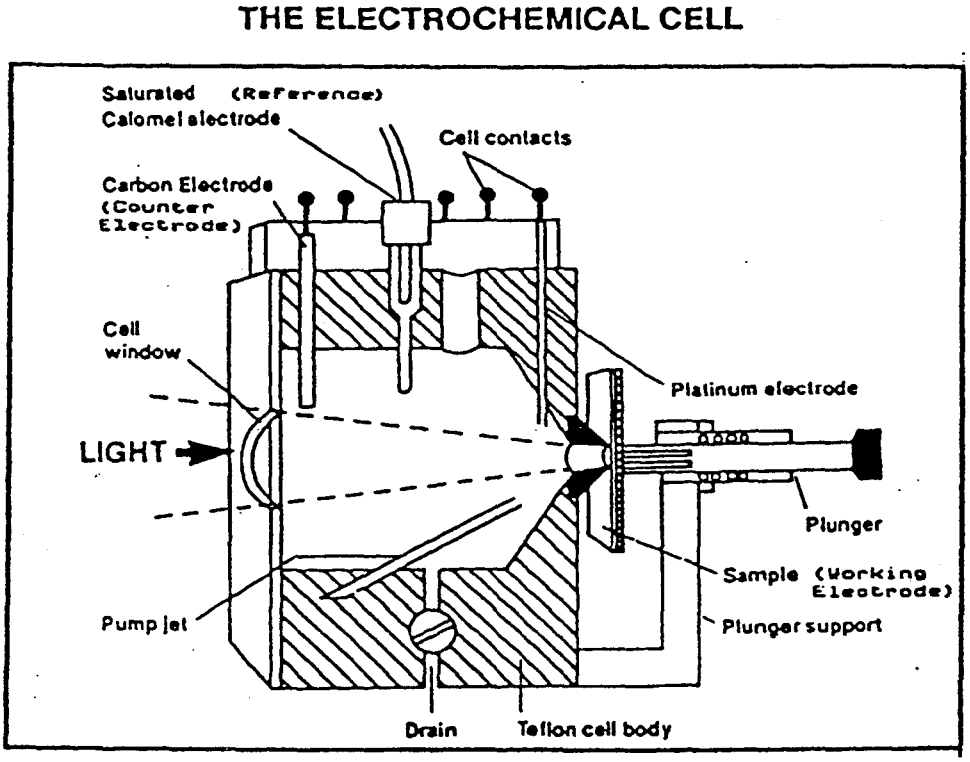

Fig. C.8 Schematic of the electrochemical cell used for C-V measurements.

Since, the interface between the semiconductor and the electrolyte forms a Schottky junction the equations for depletion width and capacitance can be used to determine the carrier concentration. The semiconductor is reverse biased and the concentration at the edge of the depletion region is:

$$N = \frac{1}{q\varepsilon_o\varepsilon_r A^2}\frac{C^3}{dC/dV} \tag{C.17}$$

For n-type semiconductors the capacitance of the depletion region will decrease as the semiconductor is made more positive with respect to the rest potential. As a result, dC/dV and N are negative. In the case of a p-type semiconductor, the capacitance of the depletion region will increase as the semiconductor is made more positive with respect to the rest potential. Consequently, for a p-type semiconductor dC/dV and N will be positive. Experimentally, C and dC/dV are obtained by using a slowly modulated high frequency voltage bias.

Dissolution (etching) of the semiconductor depends on the presence of holes. The dissolution reactions for Si and GaAs are:

$$\begin{aligned} Si + 4h &\Rightarrow Si^{4+} \\ GaAs + 6h &\Rightarrow Ga^{3+} + As^{3+} \end{aligned} \tag{C.18}$$

For a p-type semiconductor, holes are plentiful and etching is readily achieved by forward biasing the semiconductor/electrolyte junction (i.e., the working electrode is made more positive than the rest potential). For n-type material, holes are generated by illuminating and reverse biasing the semiconductor/electrolyte junction. The etching rate is proportional to the current flowing between the semiconductor (working) and counter electrodes. The etch depth can be calculated from Faraday's law of electrolysis:

$$W_r = \frac{M}{zF\rho A}\int_0^t Idt \qquad \text{(C.19)}$$

where **M** is the molecular weight of the semiconductor, **z** is the dissolution valency (number of charge carriers required to dissolve one molecule of the semiconductor), **F** is the Faraday constant (9.64 x10^4C), ρ is semiconductor density, and **A** is the effective contact area. The depletion width is:

$$W_d = \frac{\varepsilon_r \varepsilon_o A}{C} \qquad \text{(C.20)}$$

The concentration is measured at a total depth of :

$$W_{tot} = W_r + W_d \qquad \text{(C.21)}$$

C.4 Secondary ions mass spectrometry (SIMS)

A comprehensive review of SIMS can be found in Brundle (1982). SIMS is the only chemical analysis technique which is capable of measuring impurities at concentration levels as low as 10^{15}-10^{17}cm^{-3}. In SIMS, the samples are sputtered by a focussed energetic primary ion beam that is rastered over a square area, forming a crater typically a few hundred microns on a side. The escape depth of the sputtered atoms is few monolayers for primary ion beam energies in the range of 10 to 20 keV. Secondary ions formed during the sputtering process are accelerated away from the sample surface by a nominal sample voltage of 4500V. Most ejected ions are neutrals and can not be detected by conventional SIMS. A small fraction (1%) of the ejected ions are positive or negative ions. The secondary ions from the center of the crater are focussed into the mass spectrometer for analysis. Acquiring ions only from the center of the crater is achieved by using a physical aperture as an ion-optical gate. The result is an improvement in the depth resolution by the rejection of the secondary ions emitted from

the wall of the sputtered crater where material at different depths is exposed simultaneously. The secondary ions are energy filtered by an electrostatic analyzer, and then mass-separated by the magnet of the mass spectrometer. After passing through the analyzers, the ions are detected either in an analog current mode using a Faraday cup or in pulse counting mode using an electron multiplier.

The sputtering yield (the ratio of the number of emitted particles to the number of incident particles) depends on the target material, crystallographic orientation, energy of primary ions, and incident angle of the primary ion. Preferential sputtering can occur in a multi-component material if the components have different sputtering yields. The component with the lowest yield becomes enriched at the surface. Whereas, that with the highest yield becomes depleted. Once an equilibrium situation is attained, the sputtered material has the same composition as the bulk.

The secondary ion current for a particular element of mass **M** which is being analyzed can be expressed as:

$$i_s^M = I_p Y \alpha^+ \theta_M n \qquad \text{(C.21)}$$

$\mathbf{I_p}$ is the flux of primary particles, **Y** is the sputtering yield, α^+ is the ionization probability for species **M**, and θ_M is the fractional concentration of species **M** in the surface layer, and **n** is the fraction of emitted ions which are collected. The sensitivity of SIMS can vary strongly from element to element since the secondary ion current depends on many factors. Electronegative oxygen (O_2^+) is a secondary ion yield enhancing species for electropositive elements which produce predominantly positive secondary ions. A cesium beam (Cs^+) increases the ionization probability of electronegative elements.

There are a few factors which must be taken into consideration in SIMS analyses which include the "matrix effect" and "the edge effect". SIMS shows a significant difference in the secondary ion yield from the same element in different samples or matrices, this is known as the "matrix effect". To obtain good depth resolution, it is essential that only the signal from the flat bottom portion of the sputtered crater be analyzed. Atoms are ejected from the crater bottom in addition to the sidewalls as sputtering proceeds. The sidewalls may contain a different atomic concentration than the crater bottom. This phenomena is known as the "edge effect".

C.5 X-ray diffraction (XRD)

The use of XRD has found widespread applications in the analysis of heteroepitaxial layers. An excellent review of this technique can be found in Cullity (1978) and Brundle et al. (1992). XRD has been used to identify crystalline phases, and to measure structural properties which include strain, orientation of single crystals, and preferred orientation of polycrystals.

The various x-ray diffraction methods all rely on the Bragg condition which relates the x-ray wavelength to the interplanar spacing and diffraction angle. The fundamental principles are illustrated in Fig. C.9. The diffraction angle 2θ is the angle between the incident and diffracted x-rays. Bragg's law is the condition for which constructive interference from planes with spacing $\mathbf{d_{hkl}}$ is observed (**h,k,l** are the Miller indices of the lattice plane):

$$\lambda = 2d_{hkl}\sin\theta_{hkl} \qquad \text{(C.22)}$$

θ_{hkl} is the angle between the crystal planes and the incident (and diffracted) x-ray beam and $\mathbf{d_{hkl}}$ for cubic crystals is:

$$d_{hkl} = \frac{a_o}{\sqrt{h^2 + k^2 + l^2}} \tag{C.23}$$

for a crystal of lattice constant $\mathbf{a_o}$. In order to observe diffraction, it is essential that the detector be positioned at $2\theta_{hkl}$. In addition, the crystal must be oriented with the normal to the diffracting plane coplanar with the incident and diffracted beam.

The double-crystal diffractometer geometry (Fig. C.10) is useful for the characterization of nearly perfect epitaxial thin films. The incident beam is first diffracted from a perfect single crystal, and hence is monochromatic and well collimated. This is done so that the measured diffraction peak width of the sample is sufficiently narrow for high resolution experiments. The detector is fixed at $2\theta_B$. In a rocking curve, the sample is rotated ("rocked") through the Bragg angle θ_B. The detector slits are opened to receive a large range in 2θ. The resulting curve is a plot of intensity vs. θ. The width of the x-ray rocking (full width half maximum) from heteroepitaxial layers, gives an indication of the crystalline quality of the epilayer. The full width half maximum (FWHM) is a standard and widely quoted parameter. It is important that the geometry and specific x-ray detection conditions (e.g. detector slit width) are known before comparing FWHM values for various epilayers. For instance, glancing angle geometry will yield information on the near surface region, which tends to be of better crystalline quality than that of the interface between the epilayer and the substrate.

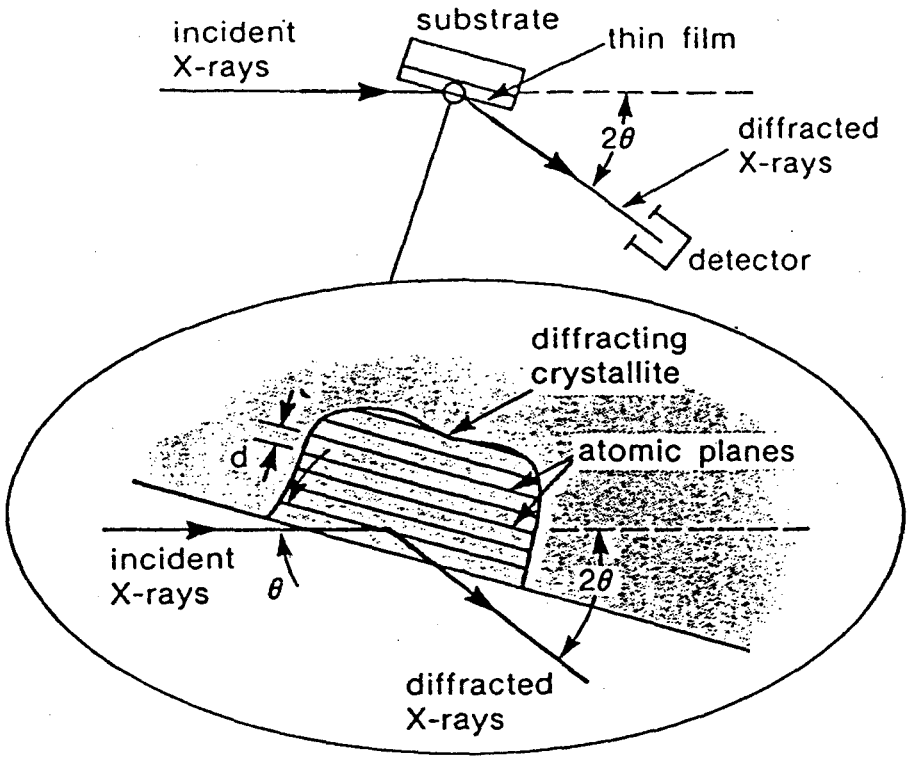

Fig. C.9 X-ray diffraction in a crystal. (Brundle et al. 1992)

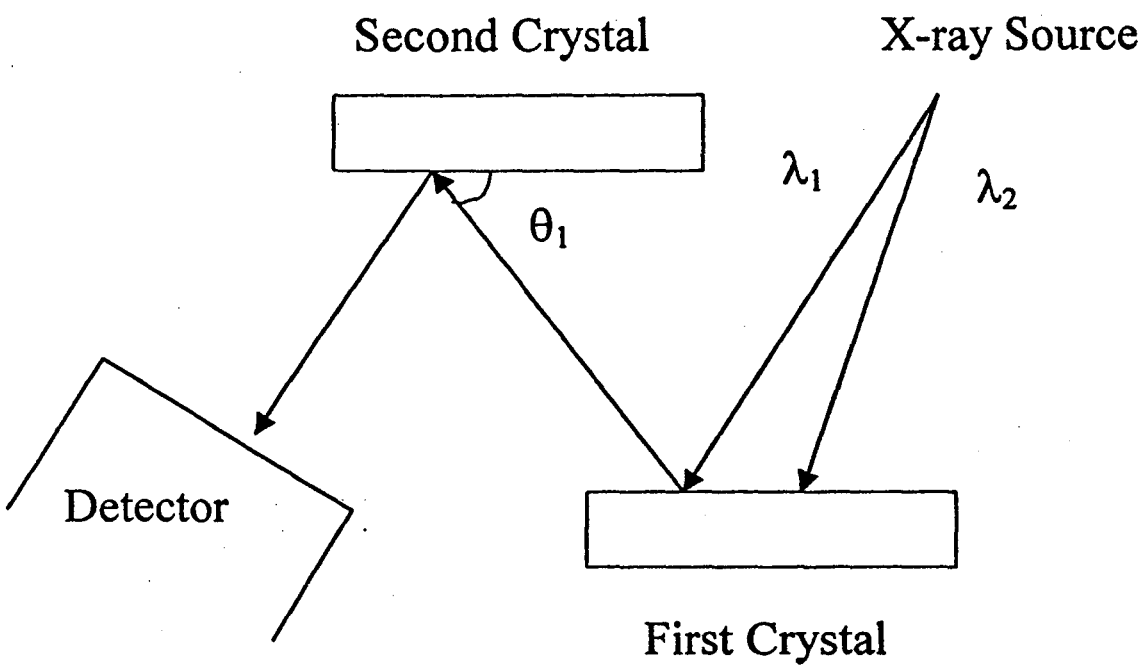

Fig. C.10 Double crystal diffractometer geometry in XRD.

C.6 Transmission electron microscopy (TEM)

For the evaluation of defects at the atomic level in layered structures and their distributions, cross-sectional TEM is the method of choice. Sample preparation of cross-sectional samples consists of the following steps (Fig. C. 11): (1) a pair of epilayer/substrate samples are glued together with a two component epoxy binder, (2) cross-sections with thickness of about 0.5 mm are cut, (3) the specimen is polished down to about 50-70 μm, (4) dimpling is employed for thinning and polishing of the sample down to 30 μm, (5) the specimen is mounted onto a single hole TEM mesh, and (6) ion milling is performed for final thinning. Usually a hole is created in the specimen and the (thin) region near the hole is characterized in TEM.

TEM has been extensively used to characterize the crystal structure, the microstructure of defects, and the composition of crystals. It has extremely high resolution of the order of Å. The high resolution achieved in the electron microscope is attributed to the extremely small wavelengths of the electron beam. High Resolution Transmission Electron Microscopy (HRTEM), also called lattice imaging, yields structural information at the atomic level. Further information on TEM and HRTEM can be found in the references Brundle et al. (1992), Schroder (1990), and Loretto (1994).

In Transmission Electron Microscopy (TEM) a parallel beam of electrons illuminates the specimen. It is essential that the sample be thin enough to transmit electrons. The transmitted and forward scattered electrons form a diffraction pattern in the back focal plane and an image is formed in the image plane. In the image mode, the diffraction lens is focused on to the image plane. Lenses are used to magnify the image. For the diffraction mode, the diffraction lens is focused onto the diffraction plane.

There are two methods for imaging in the TEM, conventional imaging and high resolution imaging. In the conventional imaging mode, the objective aperture (located in the back focal plane) is used to select one electron beam for imaging. For high resolution imaging many diffracted beams are allowed to contribute to the image.

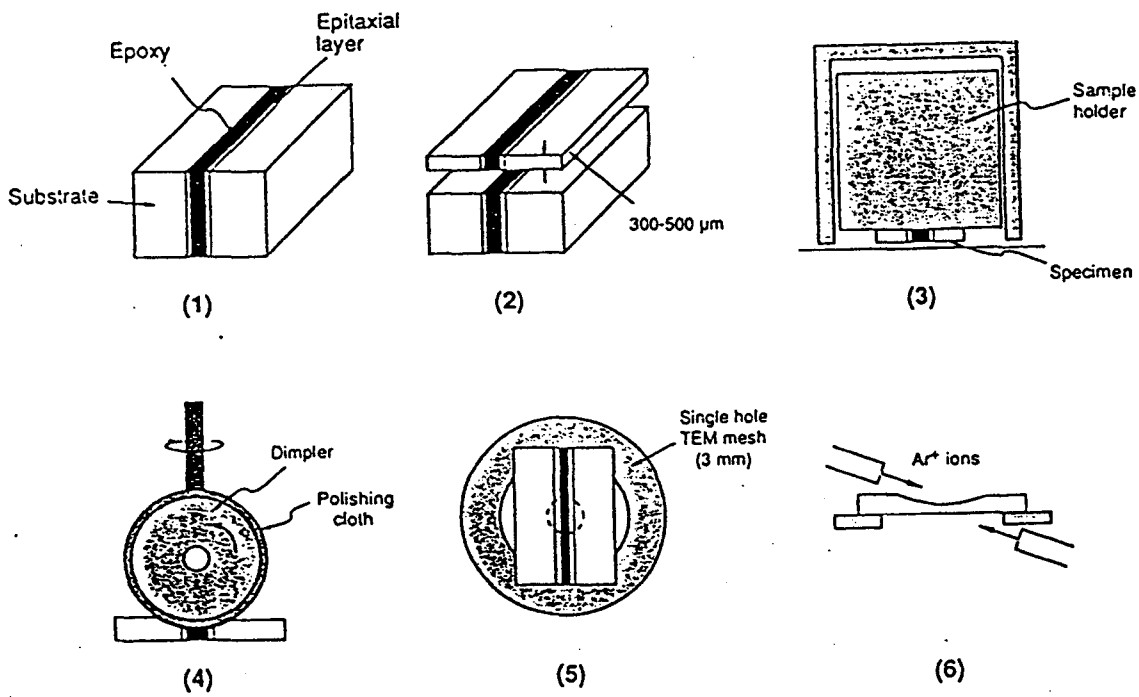

Fig. C.11 Schematic diagram for preparations of thin specimens for cross-sectional TEM: (1) a pair of epilayer/substrate samples are glued together with a two component epoxy binder, (2) cross-sections with thicknesses of about 0.5mm are cut, (3) the specimen is polished down to about 50-70 μm, (4) dimpling is used for thinning and polishing of the sample down to about 30 μm, (5) the sample is mounted onto a single hole TEM mesh, and (6) ion milling is performed for final thinning. A hole is created in the specimen and the (thin) region near the hole is characterized in TEM. (Ueda 1996)

8. References

U. G. Akano, I. V. Mitchell, F. R. Shepard, C. J. Miner, A. Margittai, and M. Svilans, Can. J. Phys. (Suppl.), **74**, S59-S63 (1996)

M. Almonte, M.S. thesis, LBL report- 38437, unpublished (1996)

D. C. D'Avanzo, IEEE Trans. Electron Devices **ED-29**, 1051 (1982)

M. Avella, J. Jimenez, and A. Alvarez, J.Appl. Phys. **82**, 3836 (1997)

N. Baber, H. Scheffler, A. Ostmann, T. Wolf, D. Bimberg, Phys. Rev. B **45**, 4043 (1992)

A. Baldereschi and N. O. Lipari, Phys. Rev. B **8**, 2697 (1973)

A. Baldereschi and N. O. Lipari, Phys. Rev. B **9**, 1525 (1974)

C. R. Barrett, W. D. Nix, A. S. Tetelman, The Principles of Engineering Materials, Prentice-Hall Inc., NJ (1974)

A. C. Beer, Galvanomagnetic Effects in Semiconductors, Academic Press, NY (1963)

B. I. Boltaks, G. S. Kulikov, I. N. Nikulitsa, F. S. Shishiyanu, Inorg. Mater. **11**, 292 (1975)

E. H. Böttcher, D. Kuhl, F. Hieronymi, E. Dröge, T. Wolf, and D. Bimberg, IEEE Quantum. Electron. **QE-28**, 2343 (1992)

H. Bracht, E. E. Haller, K. Eberl, M. Cardona, and R. Clark-P helps, Mat. Res. Soc. Symp. Proc. **527**, 335 (1998)

H. Bracht, E. E. Haller, and R. Clark-Phelps, Phys. Rev. Lett. **81**, 393 (1998b)

H. Bracht, W. Walukiewicz, and E. E. Haller, Mat. Res. Soc. Symp. Proc. **490**, ? (1998c)

M. R. Brozel, E. J. Foulkes, and B. Tuck, Phys. Stat. Solidi **72a**, K159 (1982)

V. N. Brudynl, M. A. Krivov, A. I. Potapov, and V. I. Shakhovstov, Sov. Phys. Semi. **16**, 21 (1982)

C. R. Brundle, C. A. Evans, Jr. , S. Wilson, Encyclopedia of Materials Characterization, Manning Publication, CT (1992)

S. A. Campbell, The Science and Engineering of Microelecronic Fabrication, Oxford University Press, NY (1996)

N. Chand, T. Henderson, J. Klem, W. T. Masselink, R. Fischer, Y.-C. Chang, H. Morkoç, Rehy. Rev. B **30**, 4481 (1984)

F. Clauwert. P. Van Daele, R. Baets, and P. Lagasse, J. Electrochem. Soc., **134**, 711 (1987)

J. Chevrier, M. Armand, A. M. Huber, and N. T. Linh, J. Electron. Mat. **9**, 745 (1980)

S. N. G. Chu, R. A. Logan, N. T. Ha, S. Nakahara, R. F. Karlicek, Jr., and J. A. Grenko, J. Electrochem. Soc., **141**, 242 (1994)

W. Chu, J. W. Mayer, M. Nicolet, Backscattering Spectrometry, Academic Press, NY (1978)

B. D. Cullity, Elements of X-ray Diffraction, Addison-Wesley Publishing Company, MA (1978)

J. P. de Souza and D.K. Sandana, Mater. Res. Soc. Symp. Proc. **240**, 887 (1992)

J. P. Donnelly, Inst. Phys. Conf. Sser. **33b**, 166 (1977a)

J. P. Donnelly, Solid State Electron. **20**, 183 (1977b)

L. Eaves, A. W. Smith, M. S. Skolnick, and B. Cockayne, J. Appl. Phys. **53**, 4955 (1982)

C. A. Evans, C. G. Hopkins, J. C. Norberg, V. R. Deline, R. J. Blattner, , R. G. Wilson, D. M. Jamba and Y. S. Park, Semi-insulating III-V Materials, Shiva Publishing Ltd., England, 138 (1980)

P. N. Favennec, G. P. Pelous, M. Binet, and P. Baudet, Ion Implantation in Semiconductor and Other Materials, Plenum, NY 621 (1973)

H. D. Fuchs, W. Walukiewicz, E. E. Haller, W. Dondl, R. Schorer, G. Abstreiter, A. I. Rudnev, A. V. Tikhominov, V. I. Ozhogin, Phys. Rev. B, **51**, 16817 (1995)

K. Gamo. T. Inada, J.W. Mayer, F.H. Eisen, and C.G. Rhodes, Rad. Effects **33**, 85 (1977)

S. K. Ghandi, VLSI Fabrication Principles, Second Edition, John Wiley & Sons, Inc., NY (1994)

U. Gösele and F. Morehead, J. Appl. Phys. **52**, 4617 (1981)

I. Grand, D. Rumsby, R. Ware, M. R. Brozel and B. Tuck, Semi-insulating III-V Materials, UK (1982)

B. R. M. Grovenor, Microelectronic Materials, Institute of Physics Publishing, PA (1989)

B. Gruska, H. Ullrich, R. K. Bauer, D. Bimberg, K. Wendel, J. Appl. Phys. **73**, 4825 (1993)

S. M. Gulwadi and M. V. Rao, J. Appl. Phys. **69**, 162 (1991)

D. E. Holmes, R. G. Wilson, P. W. Yu, J. Appl. Phys. **52**, 3396 (1981)

D. E. Holmes, R. T. Chen, K. R. Elliot and C. B. Kirkpatrick, Appl. Phys. Lett.. **40**, 46 (1982)

R. H. Hopkins and A. Rohatgi, J. Cryst. Growth **75**, 67 (1986)

H. R. Huff and E. Sirtl, Eds., Semiconductor Silicon, The Electrochemical Society, NJ, 968 (1978)

A. T. Hunter, H. Kimura, J. B. Baukus, H. V. Winston, and O. J. Marsh, Appl. Phys. Lett. **44**, 74 (1984)

R. C. Jaeger, Introduction to Microelectronic Fabrication, Addison-Wesley Publishing Co., MA (1988)

A. Juhl, A. Hoofman, D. Bimberg, K. Wendel, J. Appl. Phys. **73**, 4825 (1993)

H. Kamda, S. Shinoyama, A. Katsui, J. Appl. Phys. **55**, 2881 (1984)

J. Katcki, M. Shiojiri, T. Isshiki, and K. Nishio, Electron Techn., **29**, 393 (1996)

C. Kittel, Introduction to Solid State Physics, 6th Edition, John Wiley & Sons, Inc., NY (1986)

W. Kohn, and J. M. Luttinger, Phys. Rev. **97**, 1721 (1955)

W. Kohn and J. M. Luttinger, Phys. Rev. **98**, 915 (1955)

D. Kuhl, F. Hieronymi, E.H. Böttcher, T. Wolf, A. Krost, and D. Bimberg, Electron Lett. **26**, 2107 (1990)

S. S. Kular, B. J. Sealy, K. G. Stephens, D. K. Sadana, and G. R. Booker, Sol. St. Elect. **23**, 831 (1980)

J. Lagowski, H. C. Gatos, J. M. Parsey, K. Wada, M. Kaminska, and W. Walukiewicz, Appl. Phys. Lett. **40**, 342 (1982)

D. V. Lang and R. A. Logan, Phys. Rev. Lett. **39**, 635 (1977)

D. V. Lang, Deep Levels in Semiconductors, Gordon and Breach, NY (1986)

J. M. Langer and H. Heinrich, Phys. Rev. Lett. **55**, 1414 (1985)

N. T. Linh, A. M. Huber, P. Etienne, G. Morrillot, P. Duchemin, and M. Bonnet, Semi-insulating Materials, Shiva Publishing Ltd., UK, 211 (1981)

J. Lindart, M. Scharff, and H.Schiott in "Range Concepts in Heavy Ion Ranges", Mat.-Fys. Med. Dan. Vid. Selsk **33**, No. 14, 1963

P. F. Lindquist, J. Appl. Phys. **48**, 1262 (1977)

M. H. Lorretto, Electron Beam Analysis of Materials, Chapman & Hall, NY (1994)

S. Makram-Ebeid and B. Tuck, Semi-insulating Materials, Shiva Publishing Ltd., England (1982)

G. M. Martin, J. P. Farges, G. Jacob, J. P. Hallais, and G. Poiblaud, J. Appl. Phys. **51**, 2840 (1980)

J. W. Mayer, L. Eriksson, and J. A. Davies, Ion Implantation in Semiconductors, Academic Press, NY (1970)

J. W. Mayer and S. S. Lau, Electronic Materials Science: For Integrated Circuits in Si and GaAs, MacMillan Publishing Company, NY (1990)

A. G. Milnes, Deep Impurities in Semiconductors, John Wiley and Sons, NY (1973)

M. Mizuta, M. Tachikawa, H. Kukimoto, S. Minomura, Jpn. J. Appl. Phys. **24**, L143 (1985)

A. J. Moll, J. W. Ager III, K. M. Yu, W. Walukiewicz, and E. E. Haller, J. Appl. Phys. **74**, 7118, (1993)

R. S. Muller and T. I. Kamins, Device Electronics For Integrated Circuits, Second Edition, John Wiley & Sons, NY (1986)

D. D. Nolte, W. Walukiewicz, and E. E. Haller, Phys. Rev. Lett. **59**, 501 (1987)

J. D. Oberstar, B. G. Streetman, J. E. Baker, and P. Williams, J. Electrochem. Soc. **128**, 1814 (1981)

J. R. Oliver, R. D. Fairman, R. T. Chen and P. W. Yu, Electron Lett. **17**, 839 (1981)

S. J. Pearton, C. R. Abernathy, M. B. Panish, R. A. Hamm, and L. M. Lunardi, J. Appl. Phys. **66**, 656 (1989)

S. J. Pearton, Mater. Sci. Rep. **4**, 313 (1990)

S. Reynolds, W. Vook, and J. F. Gibbons, J. Appl. Phys. **63**, 1052 (1988)

E. Rimini, Ion Implantation: Basics to Device Fabrication, Kluwer Academic Publishers, MA (1995)

D. K. Schroder, Semiconductor Material and Device Characterization, John Wiley & Sons, Inc., NY (1990)

B. J. Sealy, Int. Mat. Rev. **33**, 38 (1988)

D. Shaw, Ed., Atomic Diffusion in Semiconductors, Plenum, NY (1973)

J. Singh, Semiconductor Optoelectronics, McGraw-Hill, NY (1995)

R. A. Smith, Semiconductors, Cambridge University Press, Cambridge, (1959)

M. Skowronski, S. T. Neild, and R. E. Kremer, Appl. Phys. Lett. **57**, 902 (1990)

A. Srocka, H. Scheffler, and D. Bimberg. Phy. Rev. **B 49**, 10259 (1994)

T. Y. Tan and U. Gösele, Appl. Phys. A. **31**, 1 (1985)

J. R. Tesmer, M. Nastasi, J. C. Barbour, C. J. Maggiore, J. W. Mayer, Handbook of Modern Ion Beam Materials Analysis, Materials Research Society, PA (1995)

F. A. Trumbore, Bell. Syst. Tech. J. , **39**, 205 (1960)

B. Tuck and G. A. Adegboyega, Appl. Phys. **12**, 1895 (1979)

O. Ueda, Reliability and Degradation of III-V Optical Devices, Artech House Inc, MA (1996)

H. Ullrich, A. Knecht, and D.Bimberg, J. Appl. Phys. **70**, 2604 (1991)

V. A. Uskov and V. P. Sorvina, Inorg. Mater. **10**, 895 (1974)

L. J. van der Pauw, Phil. Res. Rep. **13**, 1 (1958a)

L. J. van der Pauw, Phil. Tech. Rev. **20**, 220 (1958b)

W. Walukiewicz, J. Vac. Sci. Technol. B **5**, 1062 (1987)

W. Walukiewicz, Phys. Rev. B **37**, 4760 (1988a)

W. Walukiewicz, J. Vac. Sci. Technol. B **6**, 1257 (1988b)

W. Walukiewicz, Appl. Phys. Lett. **54**, 2094 (1989)

W. Walukiewicz, Mat. Res. Soc. Symp. Proc. Vol. **300**, 421 Materials Research Society, PA, (1993)

L. Wang, L. Hsu, E. E. Haller, J. W. Erickson, A. Fischer, K. Eberl, and M. Cardona, Phys. Rev. Lett. **76**, 2342 (1996)

E. Weber, H. Ennen, U. Kaufmann, J. Windscheif, J. Schneider, and T. Wosinski, Appl. Phys. **53**, 6140 (1982)

E. Weber, Vol. Ed., Semiconductors and Semimetals, (R. K. Willardson, A. C. Beer, and E. R. Weber, eds), Vol. 38, Academic Press, NY (1993)

J. S. Williams and J. M Poate, Ion Implantation and Beam Processing, Academic Press, NY (1984)

R. E. Williams, Modern GaAs, Artech House, MA (1990)

S. Wolf and R. N. Tauber, Silicon Processing for VLSI Era. Vol 1, Lattice Press, CA (1986)

K. B. Wolfstirn, unpublished

J. A. Wolk, M. B. Kruger, J. N. Heyman, W. Walukiewicz, R. Jeanloz, and E. E. Haller, Phys. Rev. Lett. **66**, 774 (1991)

D. Wood, Optoelectronic Semiconductor Devices, Prentice Hall International, UK (1990)

S. Yamamura. T. Kimura, S. Yugo, R. Saito, M. Murata, and T. Kamiya, Nucl. Inst. and Meth. **B80/81**, 632 (1993)

J. Ziegler, J. P. Biersack, U. Littmark, The Stopping Range of Ions in Solids, Pergamon, NY (1985)

Ernest Orlando Lawrence Berkeley National Laboratory
One Cyclotron Road | Berkeley, California 94720

Prepared for the U.S. Department of Energy under Contract No. DE-AC03-76SF00098